UNIVERSIDADE DE LISBOA

FACULDADE DE CIÊNCIAS

Magnetic thin films for spintronic applications

Doutoramento em Física

Cátia Patrícia Santos da Silva

Tese orientada por:
Dr. Maria Margarida Cruz

Documento especialmente elaborado para a obtenção do grau de doutor

2017

UNIVERSIDADE DE LISBOA

FACULDADE DE CIÊNCIAS

Magnetic thin films for magnetic applications

Doutoramento em Física

Cátia Patrícia Santos da Silva

Tese orientada por:
Dr. Maria Margarida Cruz

Júri:
Presidente:
- Dr. José Rebordão

Vogais:
- Dr. Andrii Vovk
- Dr. João Pedro Araújo
- Dr. José António Paixão
- Dr. Maria Margarida Cruz
- Dr. Pedro António Algarabel

Documento especialmente elaborado para a obtenção do grau de doutor

Financiado pela Fundação para Ciência e Tecnologia através da bolsa SFRH/BD/70150/2010 e projeto PTDC/FIS/102270/2008

2017

Acknowledgements

Firstly, I would like to express my sincere gratitude to my advisor Dr. Margarida Cruz for the continuous support of my Ph.D research, for her patience, motivation, and immense knowledge. Her guidance helped me in all the time of research and writing of this thesis. I could not have imagined having a better advisor and mentor for my Ph.D study. Besides my advisor, I would also like to thank Dr. Margarida Godinho for welcoming me into LCMBT, for all these years.

My sincere thanks also goes to Dr. Andrii Vovk for all the hours spent with me tinkering with our old sputtering system, all the hours of discussion and jokes. If it wasn't for Dr. Andrii Vovk, I probably wouldn't have met Dr. Pedro Algarabel and Dr. Pavel Strichovanec, who I would also like to acknowledge for providing me an opportunity to work with them and access to their laboratory and research facilities. Without their precious support it would not have been possible to conduct this research.

I am also grateful to Dr. Rui Silva, Dr. Liliana Ferreira, Dr. Maria de Deus, Dr. António Casaca, Dr. Carlo Meneghini, Dr. Ilaria Carlomagno, Dr. Paula Ferreira and Dr. António Gonçalves for their contributions with help in the various techniques used throughout this work.

I would also like to thank all my fellow labmates, who changed a bit over the years, for the stimulating discussions (some scientific, other not so much) and all the fun we had together in the past few years.

Lastly but certainly not the least, I would like to thank my family: my boyfriend, my parents and my grandparents, for supporting me throughout writing this thesis and my my life in general.

This work was carried out with the support of the Portuguese foundation FCT, through project PTDC/FIS/102270/2008 and grant SFRH/BD/70150/2010.

Abstract

Co-N and Fe-N thin films were deposited using reactive sputtering. Different deposition conditions, varying both temperature and partial pressure (PP) of N_2 in the reactive mixture, were employed in order to obtain different compositions and clarify the relation between PP(N_2) and the final N content of the films.

In order to study the relation between the the substrate choice and the obtained crystalline order of the films, different substrates were used to perform this study: glass, Al_2O_3, MgO and TiO_2. This group of substrates was selected because of their different crystallographic structures, as glass is amorphous and Al_2O_3, MgO and TiO_2 are single crystals with hexagonal, cubic and tetragonal structures, respectively. It was observed, for both Co-N and Fe-N films, that depositions performed at room temperature or on glass result in films with very poor crystalline quality.

A similar trend for cobalt and iron nitrides when analyzing the prepared films as a function of PP(N_2): a progression towards nitrogen richer phases as the PP(N_2) during deposition was increased, associated with a decrease in the films magnetic moment and increase in coercive field (particularly in films deposited on glass). The influence of the substrate was discovered to be paramount for the films properties, inducing different orientation of growth (specially for Co-N films) and affecting the magnetic properties of the films, introducing in-plane anisotropic behavior.

Single crystals of Al_2O_3, MgO and TiO_2 were also implanted with X+N (X=Co,Fe) with energies of 110 keV and 35 keV and fluences of 2×10^{17} at/cm^2 and 5×10^{16} at/cm^2, respectively, to form nitrides

embedded in the oxide matrix and study the role of the interfaces between embedded nitrides and host oxides.

Lastly, samples consisting of n layers (n=2,3) of alternating Fe and Fe-N films were deposited in order to study the influence of the interaction and interplay between Fe and Fe-N layers on the overall magnetic properties. However, the formation of clear boundaries and consequently real multilayers was not possible, result explained by nitrogen mobility at the high temperature of deposition.

Agradecimentos

Em primeiro lugar, gostaria de expressar a minha gratidão à minha orientadora Dr. Margarida Cruz pelo apoio contínuo que deu ao meu trabalho, pela sua paciência, motivação e conhecimento. A sua orientação foi fundamental ao logo de todo o trabalho de investigação, bem como durante a escrita desta tese. Eu não poderia ter tido uma pessoa mais indicada como conselheira e mentora para o meu doutoramento. Além da minha orientadora, gostaria também de agradecer à Dr. Margarida Godinho por me receber no LCMBT durantes todos estes anos.

Quero também expressar o meu agradecimento ao Dr. Andrii Vovk por todas as horas gastas comigo no nosso velhinho sistema de deposição e por todas as horas de discussão e piadas. Se não fosse pelo Dr. Andrii Vovk, eu provavelmente não teria conhecido o Dr. Pedro Algarabel e o Dr. Pavel Strichovanec, a quem eu também gostaria de agradecer por me terem dado a oportunidade de trabalhar com eles e acesso ao seu laboratório e instalações. Sem o seu precioso apoio, este trabalho não teria sido possível.

Agradeço também ao Dr. Rui Silva, Dr. Liliana Ferreira, Dr. Maria de Deus, Dr. António Casaca, Dr. Carlo Meneghini, Dr. Ilaria Carlomagno, Dr. Paula Ferreira e Dr. António Gonçalves pelas suas contribuições com as vrias técnicas usadas neste trabalho.

Também gostaria de agradecer a todos os meus colegas de laboratório, que foram mudando ao longo dos anos, pelas estimulantes discussões (algumas científicas, outras nem por isso) e por todos os momentos de diversão que tivemos juntos nos últimos anos.

Por último, mas certamente não menos importante, gostaria de agradecer à minha família: ao meu namorado Tiago Santos, aos meus pais e aos meus avós paternos, por me apoiarem durante todo o processo de escrita desta tese e na minha minha vida em geral.

Este trabalho foi realizado com o apoio da FCT, através do projeto PTDC/FIS/102270/2008 e bolsa de doutoramento SFRH/BD/70150/2010.

Resumo

O trabalho deste projeto de doutoramento foca-se em nitretos metálicos (de ferro e cobalto): na sua preparação e nas suas propriedades magnéticas. A técnica de eleição para a preparação dos mesmos em forma de filmes finos foi a pulverização catódica (*sputtering*). Uma grande parte do esforço efetuado neste trabalho esteve associado à recuperação de um equipamento de produção de filmes por este método, presente no Campus Tecnológico e Nuclear do Instituto Superior Técnico, que inicialmente apresentava inúmeros problemas, nomeadamente

- Incapacidade de obtenção de um nível de vácuo satisfatório
- Impossibilidade de introdução de mais do que um gás na câmara de deposição
- Impossiblidade de efetuar deposições acima da temperatura ambiente
- Os magnetrões presentes no sistema não se encontravam preparados para utilização de alvos magnéticos, como Fe e Co

Todas estas falhas foram revistas e corrigidas, sendo neste momento possível efetuar deposições a alta temperatura tendo como alvo materiais magnéticos e recorrendo a dois gases (tipicamente árgon e azoto) para produzir a mistura reativa. Contudo, apesar de todas as melhorias efetuadas, o sistema não provou ser viável para a produção dos nitretos magnéticos pretendidos. Por esse motivo, todos os filmes cujos resultados são apresentados e discutidos neste trabalho foram produzidos no Instituto de Nanociencia de Aragón (INA) em Saragoça.

Na técnica de deposição utilizada recorre-se à atmosfera presente na câmara de deposição para causar a ejeção de material do alvo escolhido que pode posteriormente reagir (ou não) com os iões da atmosfera, no nosso caso iões de azoto, antes de se depositar no substrato. As condições de deposição dos filmes finos estudados foram variadas de modo a permitir a obtenção de diferentes compostos e observar o impacto que a variação de parâmetros como a temperatura e a pressão parcial de azoto têm no crescimento e composição dos filmes. Diferentes substratos foram também usados para estudar a influência dos mesmos no crescimento dos filmes. Verificou-se que a utilização de um substrato amorfo (vidro) leva à obtenção de filmes com má qualidade cristalina. Mesmo quando se recorre à utilização de substratos monocristalinos (Al_2O_3, MgO, TiO_2) não há garantia imediata de obtenção de filmes orientados, pois verifica-se que quando as deposições são efetuadas à temperatura ambiente isso leva à produção de filmes com fraca qualidade cristalina e potencia o aparecimento de óxidos.

Relativamente às pressões parciais de azoto utilizadas, verificou-se que um aumento da quantidade de azoto presente na atmosfera reativa durante a deposição leva a um aumento do teor de azoto nos filmes produzidos, observando-se tipicamente uma evolução com a pressão parcial do tipo:

$$X \rightarrow X_4N \rightarrow X_3N$$

onde X representa Fe ou Co.

Para os diferentes nitretos obtidos verificou-se que há um decréscimo do momento magnético por átomo metálico com o aumento do teor de azoto. Este facto está associado ao decréscimo de momento que ocorre nos atómos metálicos devido à hibridização entre orbitais dos mesmos e a orbital *2p* do azoto, logo quanto maior for o teor de azoto, maior o decréscimo causado. Verificou-se também, especialmente em filmes depositados em vidro, que o campo coercivo do filme magnético

aumenta progressivamente com o aumento do conteúdo de azoto.

Relativamente aos filmes de Co-N, observou-se que os filmes crescem epitaxialmente sobre os substratos monocristalinos de Al_2O_3 e MgO com direcções de crescimento diferentes, determinadas pela orientação do substrato escolhido. Essa dependência é determinada pelas tensões provocadas pelo desajuste das estruturas do substrato e do filme e corresponde à situação de mínimo desajuste, sendo favorecidas as orientações em que as distorções causadas ao filme são de expansão ou compressão em ambas as direcções perpendiculares no plano. No caso de filmes de Fe-N este efeito parece menos marcado pois quando se obtém a fase Fe_4N esta cresce sempre com orientação (100) independentemente do substrato utilizado, indicando que esta será a direcção de crescimento preferencial para este composto. Este resultado pode ser entendido considerando o crescimento de uma camada de composição mista na interface entre o filme e o substrato, devido à elevada afinidade entre ferro e oxigénio (elemento presente em elevada quantidade nos substratos utilizados).

A utilização de substratos cristalinos, além de condicionar a orientação dos filmes, tem também impacto na composição e nas propriedades magnéticas dos mesmos. Observou-se que em filmes depositados simultaneamente nas mesmas condições de temperatura e pressão sobre os diferentes substratos cristalinos, a composição em azoto presente nos filmes não é igual, sendo sempre superior nos filmes depositados em substratos cristalinos, relativamente a filmes depositados em vidro, indicando que a ordem da estrutura tem um papel ativo na integração de azoto no filme, permitindo estabelecer as ligações químicas necessárias para obter um composto com mais elevado teor de azoto.

Também se verificou que os filmes depositados sobre monocristais apresentam momento magnético superior ao observado para filmes homólogos depositados em vidro, mesmo quando estes são depositados à temperatura ambiente e apresentam fraca qualidade cristalina.

Um dos resultados mais relevantes é a influência dos substratos mono-

cristalinos nas propriedades magnéticas dos filmes obtidos, nomeadamente no aparecimento de anisotropia magnética induzida por tensões entre o filme e o substrato. Nos casos em que as direcções perpendiculares do substrato não são equivalentes aparece comportamento anisotrópico; mesmo no caso do filme Fe_4N com orientação (100) que tem estrutura cúbica e apresenta direcções perpendiculares no plano perfeitamente equivalentes. Este resultado indica que através de uma escolha adequada de substrato e para condições de deposição adequadas se conseguem obter filmes com elevado momento magnético, cuja estabilidade química é superior à do respectivo metal e cuja anisotropia se pode adaptar para a utilização pretendida.

Foram também produzidas amostras por implantação iónica de Fe/Co e N em monocristais de Al_2O_3, MgO e TiO_2 usando energias de implantação que permitem uma dispersão dos elementos implantados numa região de aproximadamente 100 nm do cristal implantado e fluências num rácio de 4:1 de metal/azoto. Verificou-se que, mesmo procedendo à implantação do azoto em primeiro lugar, a elevada afinidade dos metais para formarem ligações com o oxigénio presente na rede cristalina leva ao aparecimento de óxidos e compostos com estrutura espinela do tipo YX_2O_4 não tendo por isso sido observada a formação de X_4N, apenas X_3N e X_2N (X=Fe,Co).

A implantação promove a criação de uma zona altamente danificada no cristal que, mesmo após um recozimento de 1 hora a 250^{o}C em vazio, não recupera significativamente. O mesmo tratamento térmico também não causa difusão ou rearranjo significativo dos elementos implantados, não tendo causado alterações relevantes nas propriedades magnéticas observadas.

Por último, foram também depositadas n camadas (n=2,3) de nitreto de ferro alternado com ferro, numa tentativa de criar um sistema de multicamadas que permitisse estudar a influência das fronteiras e das interações metal-nitreto nas propriedades magnéticas. Infelizmente, verificou-se que à temperatura de deposição, de 250^{o}C que potencia

a formação de nitretos, a difusão do azoto é elevada condicionando a formação de fronteiras bem definidas entre as camadas. Os resultados experimentais são compatíveis com a formação de uma mistura de compostos com teor de azoto variável.

Glossary

AFM	Atomic force microscopy
$\vec{B}$	Magnetic induction
$\mathbf{B}_{hf}$	Hyperfine field
CEMS	Conversion electron Mössbauer spectroscopy
DOS	Density of states
$\mathbf{E}_F$	Fermi energy
EXAFS	Extended X-Ray Absorption Fine Structure
F	Helmholtz free energy
FC	Field-cooled
fcc	Face-centered cubic
FT	Fourier transform
$\vec{H}$	Applied magnetic field
$\mathbf{H}_C$	Coercive field
hcp	Hexagonal close-packed
ICDD	International Centre for Diffraction Data
IS	Isomer shift
$\vec{M}$	Magnetization
MR	Magnetoresistance
$\mathbf{m}_s$	Saturation magnetic moment
$\mathbf{N}_d$	Demagnetizing factor
PCAR	Point-contact Andreev Reflection

PP	Partial pressure
QS	Quadrupole splitting
RBS	Rutherford backscattering spectrometry
RT	Room temperature
SQUID	Superconducting quantum interference device
SRIM	Stopping and range of ions in matter
$\mathbf{T}_B$	Blocking temperature
$\mathbf{T}_C$	Curie temperature
XANES	X-ray near edge extended structure
XRD	X-ray diffraction
XRR	X-ray reflectivity
ZFC	Zero field-cooled
χ	Magnetic susceptibility
Γ	Line width
μ	Magnetic permeability
μ_0	Vacuum magnetic permeability
μ_B	Bohr magneton
ρ	Resistivity

Contents

Chapter 1

Introduction

Metallic nitrides have been used for industrial purposes for many years due to their excellent mechanical hardness and chemical stability. The potential of magnetic nitrides for applications, especially in the magnetic recording media area was recognized since the first reports on iron nitrides [1; 2; 3].

Iron and cobalt nitrides offer the possibility to combine metallic conductivity and high magnetization with the good chemical stability and mechanical endurance characteristic of nitrides [2; 4; 5]. They share similar nitride phases with different stoichiometry, magnetic properties and structure: M_4N, M_3N, M_2N and MN (M=Fe,Co). These nitrides are interstitial compounds, *i.e.* N atoms occupy interstitial sites in the lattice, and therefore some of the phases are often non-stoichiometric [6]. It is known that M_4N and M_3N ,are ferromagnetic, while M_2N and MN are paramagnetic and that the saturation magnetization of the ferromagnetic phases decreases with increasing nitrogen content [7; 8; 9]. Besides the nitride phases already referred, a ferromagnetic phase with less nitrogen, $Fe_{16}N_2$, was also reported for iron. $Fe_{16}N_2$ has a magnetization strongly dependent on the degree of ordering of the nitrogen atoms in the lattice and consequently affected by microstructural features and surface morphology. In this work, the main interest relies in the ferromagnetic phases M_3N and M_4N (M=Fe,Co).

Fe_3N and Co_3N are ferromagnetic and have hexagonal structure that can be viewed as the hexagonal structure of the metal with added interstitial nitrogen ions. These structures can accommodate a range of different stoichiometries as

$M_{3-x}N$ (M=Fe,Co) with $0 < x < 1$.

Fe_4N and Co_4N possess higher saturation magnetization than Fe_3N and Co_3N, with values ranging between 186 and 205 Am^2/kg for Fe_4N [10; 11] and between 23.3 and 85.1 Am^2/kg for Co_4N [7; 8]. They share similar anti-perovskite structure consisting of a face-centred cubic (fcc) lattice of iron or cobalt with a N atom in the centre of the cubic cell (fig. 1.1). In this structure, the metal ions occupy two different sites, the vertices of the cubic cell (Fe^I or Co^I) and the centre of the faces (Fe^{II} or Co^{II}). The metal ions in the vertices are more distant from the N ions than the ones at the face centres and have larger magnetic moment [12; 13]. This was experimentally verified for iron by neutron diffraction measurements [14], giving magnetic moment moments of 2.98 μ_B and 2.01 μ_B for Fe^I and Fe^{II}, respectively. Stoichiometric Co_4N was not yet obtained but *ab initio* studies indicate that the results are similar for the cobalt ions magnetic moments [15; 16]. In fig. 1.2 we can see the spin polarized density of states (DOS) calculated for Fe_4N (a) and Co_4N (b) [15; 16]. The DOS for M^I resembles that of bulk metal fcc-structure [5] indicating that the M^I have very weak bonding with N atoms. The DOS of M^{II} extends over a wider energy range than M^I. The N(*2p*) electronic density populates the bottom of the valence band (below -6 eV) mixing with M^{II} states and implying a strong covalent bond N-M^{II} [17]. The calculated magnetic moments for the atoms in both structures are 2.98 μ_B and 2.01 μ_B for Fe^I and Fe^{II} [14] and 1.94 μ_B and 1.49 μ_B for Co^I and Co^{II} and a much smaller magnetic moment for N (<0.1 μ_B) [5].

An important feature of Fe_4N and Co_4N that makes them particularly interesting, especially for spintronic applications, is their spin polarization, which has been predicted to be 1 for iron [18] and 0.88 for cobalt[1] [19; 20]. Experimentally, using Point Contact Andreev Reflection (PCAR), Narahara *et al.* observed a spin polarization of 0.59 at 7.8 K for Fe_4N [21]. This material has already been successfully used as a ferromagnetic electrode in a magnetic tunnel junction consisting essentially of Fe_4N/MgO/CoFeB, yielding a considerable tunnelling magnetoresistance

[1]Spin polarization is defined as

$$P_{DOS}(E) = \frac{D_\uparrow(E) - D_\downarrow(E)}{D_\uparrow(E) + D_\downarrow(E)} \tag{1.1}$$

where $D(E)$ corresponds to the DOS of the respective spin population at energy E.

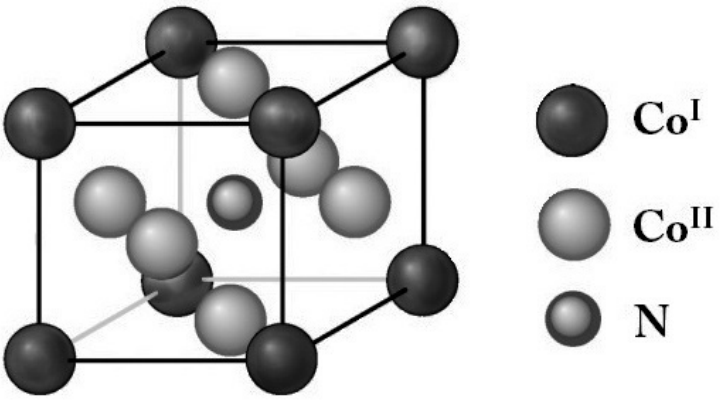

Figure 1.1: Co_4N structure.

of 18.5 % [22].

Early reports on Co-N thin films by Matsuoka *et al.* explore the structure and magnetic properties of cobalt nitrides for perpendicular magnetic recording applications [6; 23; 24], indicating that Co_4N films can develop perpendicular anisotropy.

Fe_4N has also interesting optical properties, exhibiting anomalous light reflectivity that can be modulated by an external magnetic field making it an optically smart material [3] with possible applications in optical switching devices. Co_4N also has potential as a catalyst for chemical processes involving nitrogen, namely for NO and hydrazine decomposition [25].

In this work the possibility of producing ferromagnetic films of iron and cobalt nitrides with different magnetic anisotropies controlled by the substrate is explored. The substrates used for this work were chosen to allow the study of the effect of different substrate geometries and structures both on the films' growth and properties and on the magnetic anisotropy of the nitride layer. Iron nitrides are more easily produced than cobalt nitrides. For instance Fe_4N can be obtained with the correct stoichiometry while $Co_{4+x}N$ is only obtained with x>12 [26]. For this reason the system Fe-N was chosen to produce bi-layers and multi-layers Fe/Fe-N.

Also single crystals, similar to the ones used as substrates, were implanted with Fe+N or Co+N to study the possibility of the formation of nitride phases embedded in a crystalline matrix.

The text has the following structure: chapter 2 summarizes the main concepts

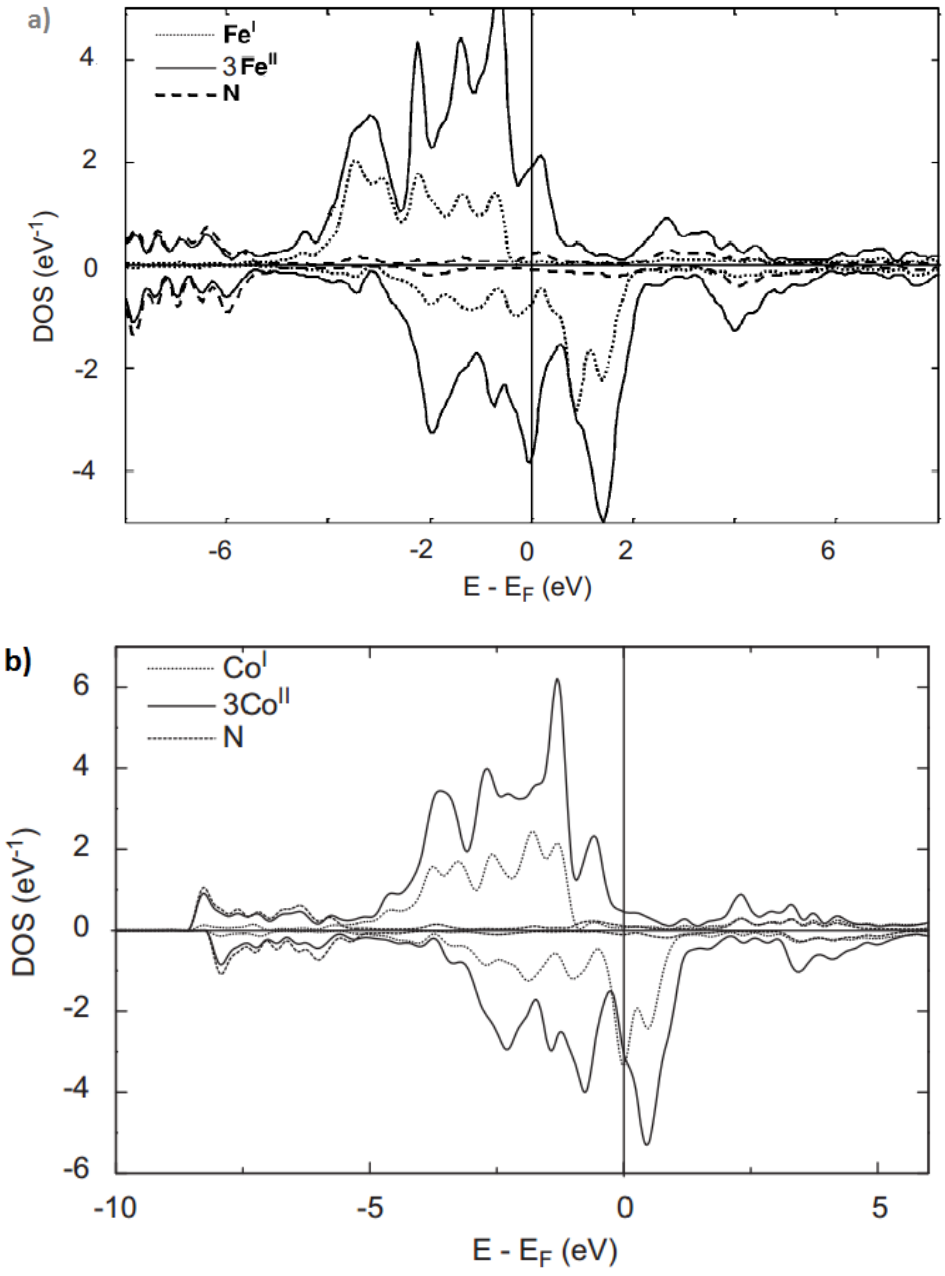

Figure 1.2: Spin and spin projected density of states (DOS) of a) Fe_4N and b) Co_4N [15; 16].

of magnetism required to explain the systems' behaviour, chapter 3 presents a description of the experimental techniques used throughout this work. In chapters 4 and 5 the experimental results and their analysis are presented and discussed. Since the essential part of the results for Co-N films is already published in two papers, a significant part of chapter 4 reproduces the text of these papers with permission of the editors. In chapter 6 the results regarding the samples produced by ionic implantation are presented and discussed. Chapter 7 concludes this thesis with a summary of the most significant result and conclusions.

Chapter 2

Fundamentals

2.1 Magnetic properties

The magnetic response of a material to an external magnetic field ($\vec{H}$) is measured by the magnetization $\vec{M}$, defined as the magnetic moment per unit volume. The relation between the magnetization and the applied field is given by the magnetic susceptibility χ:

$$\vec{M} = \chi \vec{H} \tag{2.1}$$

a second rank tensor that can be defined as

$$\chi = \nabla_{\vec{H}} \vec{M} \tag{2.2}$$

The magnetic induction $\vec{B}$ is the magnetic field inside the material that depends on the magnetization and external magnetic field $\vec{H}$ by $\vec{B} = \mu_0(\vec{H} + \vec{M})$, where $\mu_0 = 4\pi \times 10^{-7}$ Vs/Am is the vacuum magnetic permeability. This can also be written as $\vec{B} = \mu\vec{H}$ with $\mu = (1 + \chi)\mu_0$ being the magnetic permeability of the medium. In many cases the magnetic susceptibility tensor is diagonal with all directions equivalent (polycrystalline materials or cubic structures) and the material can be characterized by the diagonal value χ.

For most materials the magnetization is non zero in applied magnetic field and becomes zero when the magnetic field is removed. In these cases if $\chi < 0$ the

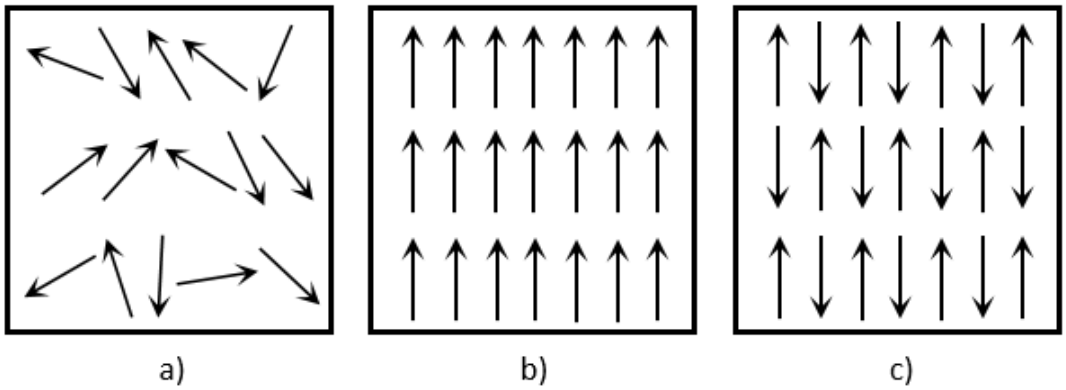

Figure 2.1: Typical distribution of directions for the local magnetic moments without applied magnetic field a) in a solid without magnetic interactions, b) in a ferromagnetic material below its critical temperature and c) in an antiferromagnetic material below its critical temperature.

behaviour is denoted diamagnetic and the induced magnetization is opposite to the applied field, while if $\chi > 0$ materials are termed paramagnetic.[1]

In general, a paramagnetic material has atoms with permanent magnetic moments that have negligible interactions. Without applied magnetic field the magnetic moments will be oriented randomly due to thermal disorder and, consequently, there will be no net magnetic moment for the paramagnetic solid (fig. 2.1 a)). If interactions are relevant and correlate the magnetic moments on neighbouring atoms, long-range magnetic order may develop. The patterns represented in fig. 2.1 correspond to the simplest ordered magnetic arrangements: ferromagnetism and antiferromagnetism. In ferromagnetic materials, the magnetic moments order parallel to each other resulting in spontaneous magnetization existing without applied magnetic field (fig. 2.1 b)). In antiferromagnetic materials the neighbouring magnetic moments are ordered with antiparallel arrangement (fig. 2.1 c)) resulting in a configuration with zero magnetization[27]. More complex configurations are also possible, such as ferrimagnets, helical spin arrays and canted ferromagnets or antiferromagnets. The compounds studied in this work are ferromagnetic.

[1]The magnetic behaviour of an atom is detailed in Appendix A.

2.2 Exchange interactions

The magnetic ordered patterns referred result, in first order, from the Coulombian interaction between the shared electrons denoted exchange interactions. This type of interactions are well illustrated by the bond formation in the diatomic molecule H_2. In this case, the Coulomb interaction shifts the energy of the electronic states of the shared electrons

$$\Delta E = Q \pm J \tag{2.3}$$

where Q measures the energy associated with the Coulombian repulsion between the electrons in the two atomic states and J is a term of quantic origin, the integral of mixed orbitals (exchange integral), that separates the energy of the state with $S = 0$ (singlet state) from the energy of the state $S = 1$ (triplet state), respectively associated with the sign $+$ and $-$ in 2.3. (For a more detailed description see Appendix B.)

The energy difference between both states, singlet and triplet, is then simply

$$E_s - E_t = 2J \tag{2.4}$$

The exchange integral, J, can be either positive or negative which determines the alignment to be parallel or antiparallel.

Heisenberg proposed in 1928 that if the exchange integral between two adjacent atoms was positive and magnetic electrons were described by localized orbitals then the resultant spins of neighbouring atoms would align parallel since this alignment will minimize the total energy [28]. Following Heisenberg's proposal, the exchange energy can be written as

$$E_{exch} = -2J\vec{S}_i \cdot \vec{S}_j \tag{2.5}$$

with $\vec{S}_i$ and $\vec{S}_j$ being the resultant spins of adjacent atoms i and j and J, the exchange integral being intrinsically dependent on the overlap between orbitals in adjacent atoms. If the interatomic distance is large, *i.e.* small wave function overlap, the exchange coupling will be weak and incapable of overcoming the thermal excitations, giving rise to paramagnetic behaviour. The definition (2.5) is a conve-

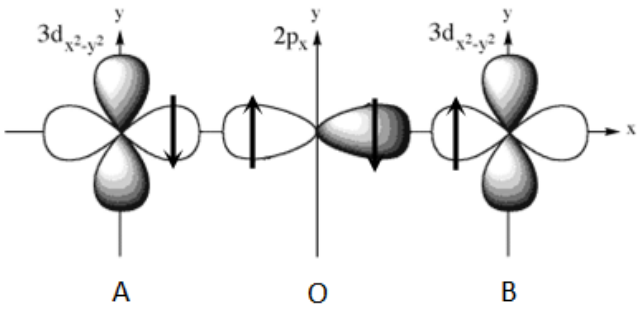

Figure 2.2: Schematic representation of the superexchange interaction between two metallic atoms (A and B) mediated by an oxygen atom.

nient phenomenological and empirical description of the exchange energy, with J being determined experimentally. It was postulated by Slater and Bethe that Fe, Co and Ni are ferromagnetic because in these elements there is a critical amount of d-orbital overlap that leads to positive J[28].

For two magnetic atoms separated by a non-magnetic atom (typically oxygen) it is possible to have a magnetic interaction mediated by the electrons of their common, non-magnetic, neighbour. This type of interaction is called superexchange. A good example is MnO where the magnetic Mn^{2+} ions order mediated by a diamagnetic O^{2-} through the overlap of the metal's *3d* with oxygen *2p* orbital (fig 2.2). The two electrons sharing the *2p* orbital have antiparallel spin due to the Pauli principle (fig. 2.2) and since their orbital overlaps the *3d* orbitals, the electrons of A and B tend to be coupled with antiparallel magnetic moments leading to antiferromagnetism. Ferromagnetic coupling can also be obtained when A and B share two different orbitals or the arrangement of the sites leads to 90° coupling. Generally, superexchange depends on the magnitude of the atomic moments of the metal atoms, the orbital overlap between metallic and non-metallic elements and the angle between the bonding orbitals.

Another type of magnetic interaction leading to magnetic order is the RKKY indirect exchange interaction (named after Rudermann, Kittel, Kasuya and Yoshida) which is most relevant in metals when there is no direct overlap of the wave functions with unpaired electrons. In this case, the conduction electrons are polarized

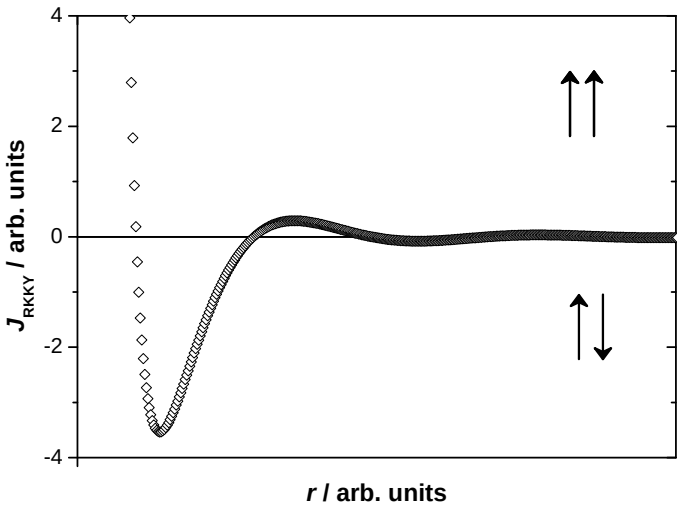

Figure 2.3: Dependence of the RKKY exchange energy on the interatomic distance r.

in the vicinity of the magnetic atom and mediate the interaction between two magnetic moments in different sites. The polarization decays with an oscillatory dependence on the distance r from the magnetic atom as $1/r^3 \cos 2k_F r$, with k_F being the radius of the Fermi sphere [28]. Depending on the separation between the interacting atoms, this coupling may lead to either a parallel or antiparallel configuration, *i.e.* ferromagnetic or antiferromagnetic arrangement (fig.2.3). Unlike what happens in the previous exchange mechanisms, this type of interaction although typically small in amplitude has a considerably large range and, in concentrated magnetic systems, provides coupling with nearest and next nearest neighbours [28].

In metallic *3d* systems, such as Fe, Co and Ni, both the atomic moments and the exchange interaction are due to delocalized (or itinerant) electrons, since the conduction electrons have states extended throughout the material and the s and d bands overlap. The exchange interaction between the conduction electrons shifts the energy bands corresponding to different spin orientation (fig. 2.4) giving rise to a non-zero total magnetic moment. The corresponding exchange splitting, ΔE_{exch}, is commonly described using the Stoner model in terms of the averaged atomic magnetization M and the integral of the exchange correlation I (Stoner exchange

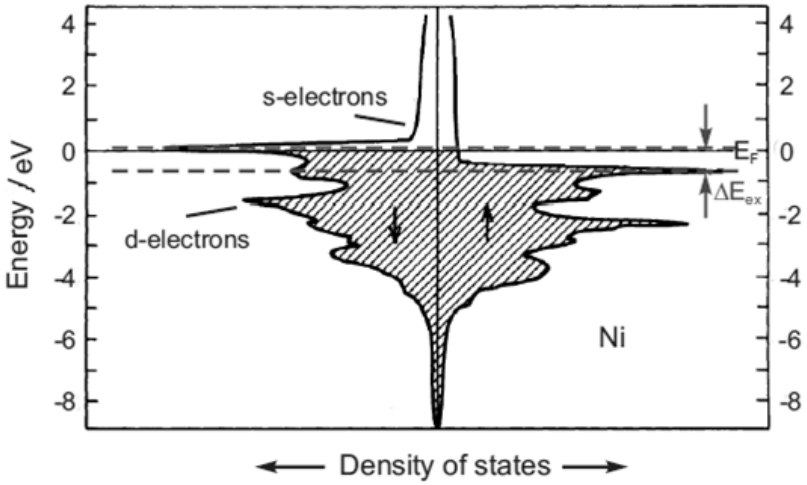

Figure 2.4: Calculated density of states of Ni. The exchange splitting ΔE_{exch} is calculated to be 0.6 eV. Adapted from [29].

parameter) which describes the energy reduction due to the electron correlation

$$\Delta E_{exch} = IM \tag{2.6}$$

Within this model, the condition for ferromagnetism to occur is given by the Stoner criterion:

$$IN(E_F) > 1 \tag{2.7}$$

where $N(E_F)$ is the density of states at the Fermi level. A high density of states and a strong spin splitting are therefore important for the appearance of ferromagnetism. The integral of the exchange correlation I, the density of states at the Fermi level and their product are plotted for metallic elements with $Z < 50$ in fig. 2.5 a) to c) showing that the Stoner criterion correctly predicts the ferromagnetic behaviour of Fe, Co and Ni. Some nitrides of these transition metals also exhibit similar ferromagnetic behaviour.

Due to thermal excitation the total moment of parallel magnetic moments decreases with temperature and is called spontaneous magnetization[1] for a ferro-

[1]In the literature, spontaneous magnetization is frequently referred to as saturation magnetization at temperature T.

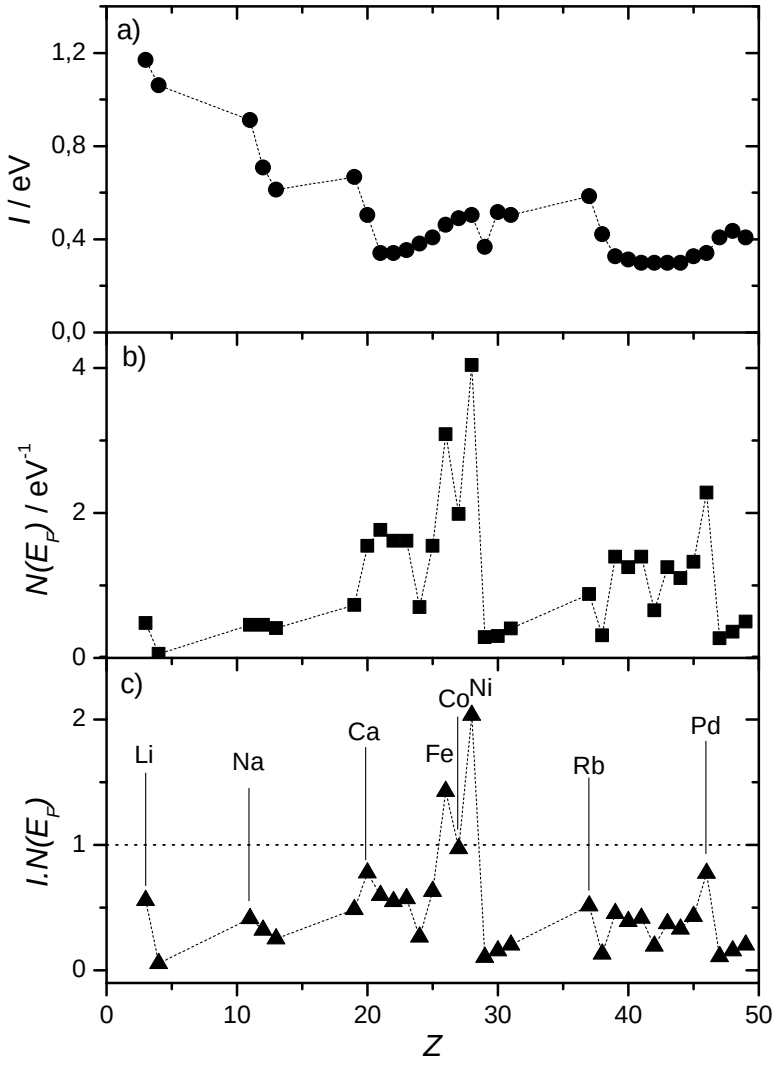

Figure 2.5: a) Integral of the exchange correlation I as a function of atomic number, b) Density of states per atom, c) Product of the density of states and the Stoner parameter I. The elements Fe, Co and Ni, with $IN(E_F) > 1$ display ferromagnetism. Adapted from [30].

magnetic material. It has the maximum value for T=0 K since all atomic moments of the atoms are oriented perfectly parallel[1]. The spontaneous magnetization decreases gradually with temperature until a critical point is achieved where the breakdown of order occurs reducing the magnetization to nearly zero in a very narrow temperature interval. The temperature at which the spontaneous magnetization reduces to zero (without applied field) is the Curie temperature, T_C. Above T_C the material becomes paramagnetic and the susceptibility follows a modified Curie law, known as the Curie-Weiss law:

$$\chi = \frac{C}{T - T_C} \tag{2.8}$$

In fig. 2.6 a) we can see the decay of the spontaneous magnetization of Fe, Co and Ni as temperature increases up to T_C.

The presence of an external magnetic field causes the transition to broaden, since the field favours the temporary presence of clusters of magnetic moments competing with thermal disordering[28].

The different materials have different spontaneous magnetization values at 0 K (saturation magnetization) and different T_C, however, when the data is normalized by saturation magnetization (M_0) and plotted as function of T/T_C all results seem to conform to a single curve (fig. 2.6 b)). This result, sometimes referred to as law of corresponding states [31], indicates that the ratio M_s/M_0 is determined by the ratio T/T_C.

Although the critical temperature of iron is over 1000 K (fig 2.6 a)) objects made of iron appear to be "unmagnetized" at room temperature but can interact with magnets. The explanation for this fact was provided by Weiss in 1907 that postulated that a ferromagnetic material is divided into small magnetized regions with different orientations called domains. In these regions the spontaneous magnetization follows the expected temperature dependence [28]. The formation of domains can be understood considering the magnetic dipolar interactions between the magnetic moments. The energy associated with these interactions is given by

[1]In a ferromagnet, the reduction of the moment implies changing the entire coupled system of interacting moments [28].

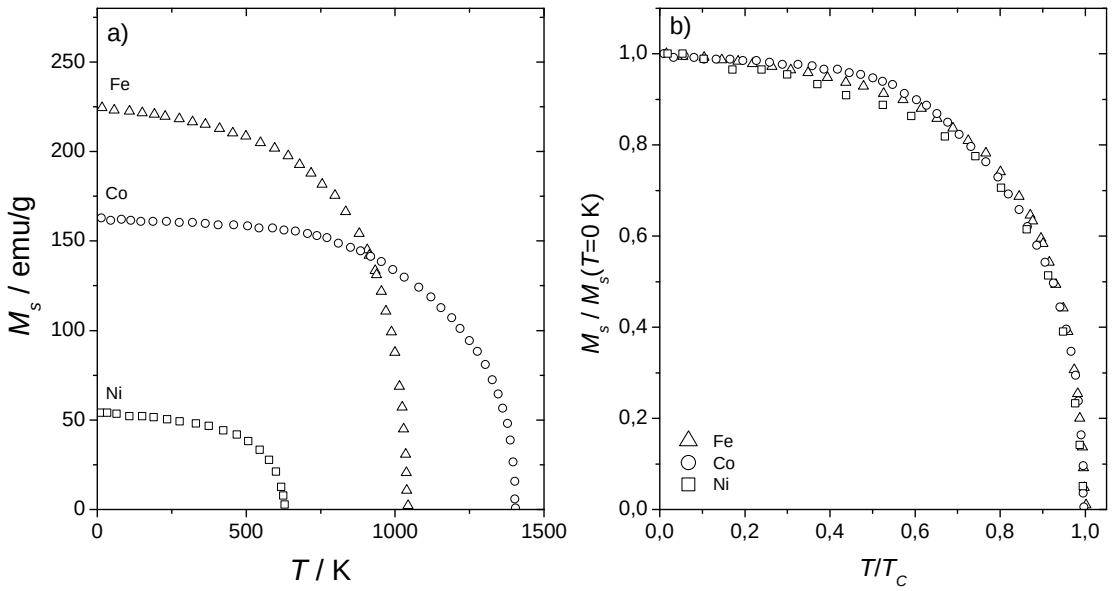

Figure 2.6: a) Spontaneous magnetization as a function of temperature for Fe, Co and Ni; b) Normalized spontaneous magnetization as a function of normalized temperature for the same materials. Adapted from [31].

[32]:

$$E_{dipolar} = \frac{\mu_0}{4\pi r^3}\left[\vec{m_1}\cdot\vec{m_2} - \frac{3}{r^2}(\vec{m_1}\cdot\vec{r})(\vec{m_2}\cdot\vec{r})\right] \tag{2.9}$$

where $\vec{m_1}$ and $\vec{m_2}$ are two magnetic dipoles separated by $\vec{r}$. This energy depends on the separation between dipoles and the degree of alignment between them [32] and is very weak (typically a thousand times smaller than the exchange coupling for nearest neighbour [27]). However, while the exchange interaction is short-ranged, the dipolar interaction is long-ranged and becomes important when a large number of spins is involved. The formation of domains with opposite orientation of magnetic dipoles decreases the volume dipolar energy at the cost of exchange energy between spins near the domains' boundaries [27].

The boundary between adjacent domains is called a domain wall and can extend for several atomic distances. It can be classified according to the angle between the magnetization of the two domains (for example, a 180° wall separates domains with opposite magnetization while a 90° wall separates domains with perpendicular magnetization). In fig. 2.7 we see a representation of two types of 180° walls,

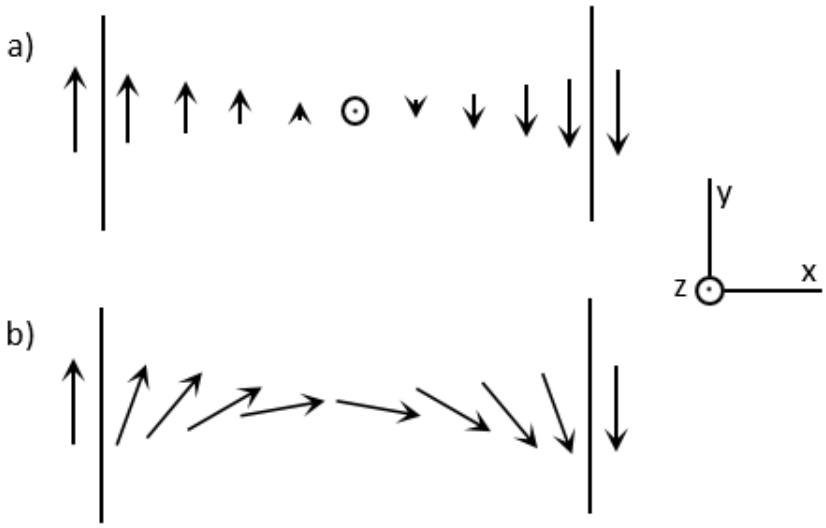

Figure 2.7: Schematic representation of a) Bloch wall; b) Néel wall.

termed Bloch and Néel walls. In the Bloch wall the magnetization rotates in a plane parallel to the plane of the wall while in the Néel wall the rotation is through a plane perpendicular to that of the wall [32].

If we consider the exchange energy given by (2.5), the energy associated with the successive pairs in a domain wall will be $-2JS^2\cos\theta$, and so the energy cost of having $\theta \neq 0$ is approximately $JS^2\theta^2$ if $\theta \ll 1$. Since it takes n steps to reverse the spin, the cost of achieving 180° reversal down a series of n spins is $JS^2\pi^2/n$ [32]. However, the domain wall width is not simply determined by the energy balance between dipolar and exchange interactions because real solids are not perfectly isotropic. The spins are coupled to the charge density by the spin-orbit coupling and therefore their orientation depends on the crystal axes symmetry. This dependence on the orientation is known as anisotropy energy. So, in practice, the thickness of a domain wall is determined by the balance between exchange, dipolar and magnetic anisotropy energies [27].

2.3 Magnetic anisotropy

In general, the magnetic properties depend on the direction of the sample in which they are measured. This corresponds to the dependence of the internal energy on

the direction of spontaneous magnetization (termed magnetic anisotropy). The energy term that describes the preference for the magnetization to lie along specific directions (easy directions of magnetization) is called magnetic anisotropy energy. This energy originates from: the spin-orbit coupling, the crystalline electric field and the dipolar interaction of magnetic moments.

In bulk materials, crystalline anisotropy is the main contribution to the total observed anisotropy, whereas in fine particles, thin films and nanostructures shape, strain and surface anisotropy contribute with energy terms that become relevant in addition to the crystalline field contribution. The spin-orbit coupling is seen as the main source of crystalline, surface and strain anisotropy, while shape anisotropy results from the magnetic dipolar contribution.

2.3.1 Crystalline anisotropy

Crystalline anisotropy is associated with the dependence of the internal energy on the direction of spontaneous magnetization relatively to the sample's crystalline directions. Generally, this magnetic anisotropy energy term contains the symmetry of the material. The simplest forms of crystalline anisotropy are the cubic anisotropy associated with cubic crystals (such as Fe and Ni) and uniaxial anisotropy in the case of hexagonal crystals (such as Co).

In the case of iron (fig. 2.8) the <100> direction is the direction where saturation magnetization can be achieved applying the lowest fields, while for the <110> direction the saturation is only achieved with high fields, making the former the easy direction and the latter the hard direction of magnetization.

In demagnetized crystals ($M = 0$), the magnetization lies along easy directions and the domain structure for a demagnetized iron disk cut parallel to (001) should be similar to that presented in fig. 2.9 (a). Obviously the domain structure represented is a simplification, since a real sample would contain many more domains, however each one would have its individual magnetization along easy directions. If a magnetic field is applied along an easy direction of magnetization, the domain walls will move allowing the domain aligned with the field to grow (fig. 2.9 b)) in detriment of the others and, in doing so, cause the energy of the crystal to be reduced. The crystal magnetization becomes saturated when only the parallel

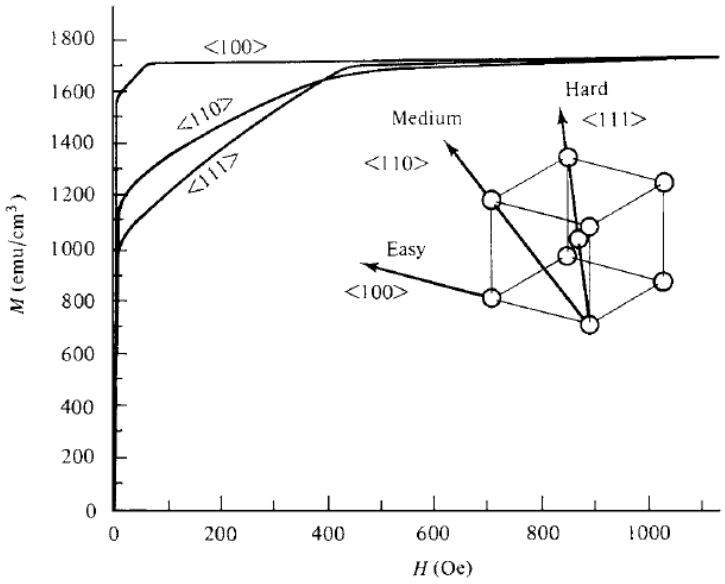

Figure 2.8: Magnetization curves measured along different crystallographic directions for a single crystal of iron [31].

domain exists (fig. 2.9 c)) corresponding to minimum energy ($E_p = -M_s H$). In this process, only domain wall motion is required and therefore the crystal can be successfully magnetized to saturation resorting to relatively low fields.

If, on the other hand, magnetic field is applied along a hard axis domain wall motion will occur to reduce the potential energy (fig. 2.10 (b)) keeping domains with moments aligned in easy directions, until only a few domains, with the same energy, remain (fig. 2.9 (c)). At this point the only way to reduce the magnetic energy is by rotation of the magnetization vectors of each domain until they are parallel to the field. This process is called domain rotation and occurs only for fairly high fields, since the magnetic energy has to overcome the crystal anisotropy energy. Since crystalline anisotropy is due mainly to spin-orbit coupling and electronic orbits' orientation is strongly fixed in the lattice by bonding, the energy required to rotate the magnetization of a domain away from an easy direction is essentially the energy required to overcome the spin-orbit coupling.

One way to express the crystal anisotropy energy is as a series expansion of the direction cosines of M_s relative to the crystal axes, *i.e.* α_1, α_2, α_3, cosines of angles a, b, c between M_s and the crystal axes, called direction cosines. The

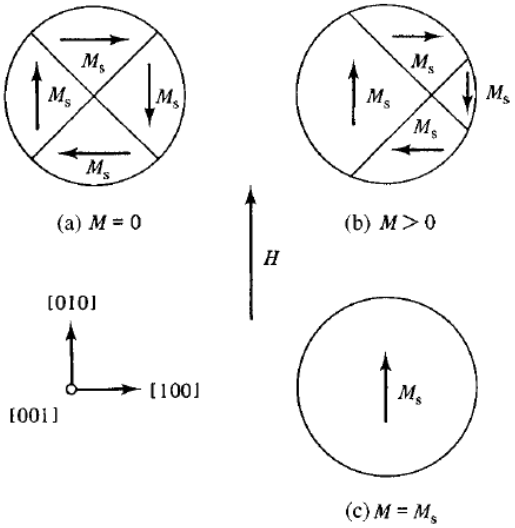

Figure 2.9: Schematic representation of the domain structure of an iron disk with field applied along the easy direction of magnetization. (a) Demagnetized state, (b) Domain wall motion, (c) Saturation.[31]

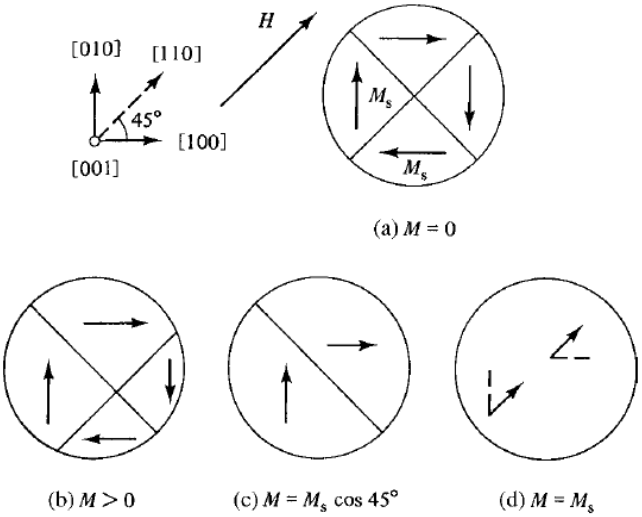

Figure 2.10: Schematic representation of the domain structure of an iron disk with field applied along the hard direction of magnetization. (a) Demagnetized state, (b) Domain wall motion, (c) Two domains with equal potential energy, (d) Domain rotation and saturation.[31]

crystal anisotropy energy is then written as

$$E_{cubic} = K_0 + K_1(\alpha_1^2\alpha_2^2 + \alpha_2^2\alpha_3^2 + \alpha_3^2\alpha_1^2) + K_2(\alpha_1^2\alpha_2^2\alpha_3^2) + ... \tag{2.10}$$

where K_0, K_1, K_2,... are constants, expressed in erg/cm^3 (cgs) or J/m^3 (SI), characteristic of the material at a particular temperature. Terms of higher order are generally not necessary and, in some cases, K_2 is so small that it can be neglected. Also, because what matters is the variation of the energy with angle, the term K_0 can be ignored since it is independent of angle. When K_2 is zero, the direction of easy magnetization is simply determined by the sign of K_1. However, in a more general case, the easy direction will depend on the values of both K_1 and K_2.

For an hexagonal crystal, like cobalt, the magnetization tends to be aligned with the c-axis. In these circumstances the anisotropy energy will depend only on the angle θ between the magnetization and the easy axis, and the anisotropic behaviour is classified as uniaxial. The anisotropy energy can therefore be written as

$$E_{uniaxial} = K_0' + K_1' \cos^2\theta + K_2' \cos^4\theta + ... \tag{2.11}$$

It is customary to express the anisotropy energy for uniaxial crystals in powers of $\sin\theta$. Using the transformation $\cos^2\theta = 1 - \sin^2\theta$ in equation (2.11), the anisotropy energy can be written as

$$E_{uniaxial} = K_0 + K_1 \sin^2\theta + K_2 \sin^4\theta + ... \tag{2.12}$$

If both K_1 and K_2 are positive, the energy minimum is obtained for $\theta = 0^o$ and the c-axis is the easy axis of magnetization. A crystal with a single easy axis can be referred to as uniaxial crystal and its domain structure in the demagnetized state is very simple, with all the domains aligned in the same direction (fig. 2.11).

If both K_1 and K_2 are negative, the minimum value is obtained for $\theta = 90^o$ and the basal plane is an easy plane of magnetization.

If both constants have opposite signs, the situation becomes more complex and, depending on their relative values, an easy axis or easy plane configuration can be

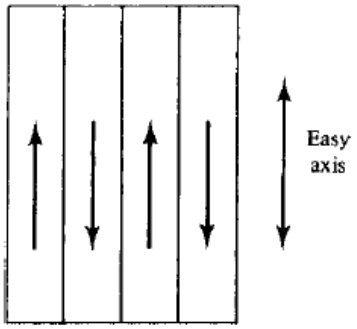

Figure 2.11: Domain structure of a uniaxial crystal in the demagnetized state.

obtained. There is also a third possibility: For a certain range of K_1 and K_2 the magnetization will tend to spontaneously align at a certain angle ($0^o < \theta < 90^o$) relatively to the c-axis creating an easy cone of magnetization. Although this configuration is unusual, it is not unknown [31].

2.3.2 Shape anisotropy

In the case of thin films, multilayers or nanostructures other contributions to the anisotropy energy, besides the crystalline anisotropy, become relevant. Anisotropic shape results in anisotropic contribution of the long-range dipolar interactions between the moments [33].

Let us consider a polycrystalline specimen having no preferred orientation of its grains and, therefore, no net crystal anisotropy. If it is spherical in shape, the same external field influences the magnetization in any direction to the same extent. However, if it is not spherical, the dipolar interaction will favour the magnetization along a long axis rather than a short axis. The dipolar interaction contribution is generally quantified as an additional magnetic field that opposes the magnetization - the demagnetizing filed H_d. This demagnetizing field depends on the shape of the specimen and the magnetization, being normally written using the demagnetizing factors N_d. For a given direction x_i, $H_{di} = N_{di}M_i$ and the energy associated with the demagnetizing field, also sometimes called magnetostatic energy, can be

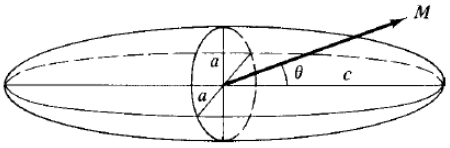

Figure 2.12: Ellipsoid of revolution uniformly magnetized.

calculated as

$$E_{ms} = \frac{1}{2}\mu_0 \vec{H}_d.\vec{M} \tag{2.13}$$

The demagnetizing factors characterize the influence of the geometric shape. The anisotropy energy of a uniformly magnetized general ellipsoid can be written as [34]

$$E_{shape} = \frac{1}{2}\mu_0(N_x M_x^2 + N_y M_y^2 + N_z M_z^2) \tag{2.14}$$

where N_x, N_y, N_z correspond to the demagnetizing factors relative to the three axis and M_x, M_y, M_z are the respective components of the magnetization.

If we take the particular case of an ellipsoid of revolution, which has a pair of equal semi-axis (a) and a distinct third semi-axis (c) (fig. 2.12), the energy can be rewritten considering only the components of the magnetization that are parallel and perpendicular to the c axis

$$E_{shape} = \frac{1}{2}\mu_0(N_c(M\cos\theta)^2 + N_a(M\sin\theta)^2) \tag{2.15}$$

where N_a and N_c correspond to the demagnetizing factors along directions a and c, respectively. Using the relation $\cos^2\theta = 1 - \sin^2\theta$, the previous expression can be rewritten as

$$E_{shape} = \frac{1}{2}\mu_0 N_c M^2 + \frac{1}{2}\mu_0(N_a - N_c)M^2\sin^2\theta \tag{2.16}$$

The first term is independent of the angle and the second term is the one that

accounts for the dependence on the angle between the magnetization and the semi-axis c, similar to what we had seen for the case of uniaxial anisotropy. The anisotropy constant for this case, K_{shape}, is then given by

$$K_{shape} = \frac{1}{2}\mu_0 M^2 \Delta \tag{2.17}$$

with $\Delta = N_a - N_c$. It is then clear that shape anisotropy, in this case, depends on the c/a ratio that will determine Δ.

2.3.3 Strain anisotropy

The dimensions of a ferromagnetic material vary when it is under the influence of an applied magnetic field. This effect is called magnetostriction. The magnetically induced strain is symbolized by λ [31] in order to distinguish it

$$\lambda = \frac{\Delta l}{l} \tag{2.18}$$

The value of λ measured at magnetic saturation is called saturation magnetostriction, λ_s, and when the term magnetostriction is used without other qualification λ_s is usually meant.

It has been observed that there is a close connection between the magnetostriction λ of a material and its magnetic behaviour under stress. Tensile stress ($\sigma > 0$), which tends to elongate a material, applied to a specimen with $\lambda > 0$ will cause an increase of the magnetization, while compressive stress ($\sigma < 0$) will cause the magnetization to decrease. This behaviour occurs even without applied magnetic field, as long as the magnetization is not zero. The effect of stress on the magnetization is then sometimes referred to as inverse magnetostrictive effect, but it is more commonly referred to as magnetomechanical effect.

The magnetostrictive strain is small in most magnetic materials, but implies that an applied mechanical stress can change the domain structure and be a new source of magnetic anisotropy.

This kind of anisotropy is often described by a magnetoelastic energy term.

$$E_{strain} = -\frac{3}{2}\lambda_s \sigma \cos^2\theta \tag{2.19}$$

where λ_s is the saturation magnetostriction, σ is the applied mechanical stress and θ is the angle between the magnetization and the stress. This expression is only valid if magnetostriction is isotropic for the material, *i.e.* it is independent on the direction of the magnetization relative to the crystal axis, which is often not the case. From (2.19) we can conclude that the response of a material to applied stress depends on the sign of the product between λ_s and σ [31].

2.3.4 Surface anisotropy

Breaking of symmetry and reduction of the nearest neighbour coordination leads to the appearance of surface anisotropy, first recognized by Néel [35]. In small magnetic nanoparticles or thin films, surface effects can be a major source of anisotropy since the magnetic contribution form the surface becomes more relevant as particle size or film thickness decrease.

The contribution of the surface to the magnetic anisotropy energy is given, to lowest order, by

$$E_{surface} = K_s' \sin^2 \theta \tag{2.20}$$

where θ is the angle between the magnetization and the surface normal [36]. In the case of films, the anisotropy constant K_s' is thickness dependent and can be expressed as

$$K_s' = 2\frac{K_s}{t} \tag{2.21}$$

with t being the thickness of the film.

Thin films have usually two different surfaces: an interface with the substrate and a real surface facing the vacuum [33]. Although these two K_s contributions are certainly different, a prefactor 2 is commonly used for simplicity as shown in (2.21). However, caution is needed if one attempts to interpret the numerical value of K_s given by this expression.

For thin films, it is usual to define an effective anisotropy constant as

$$K_{ef} = K_v + 2\frac{K_s}{t} \tag{2.22}$$

where $2K_s/t$ corresponds to the surface contribution and K_v is the volume contribution which, due to lattice distortions and the shape of the specimen, can be very different from the bulk value [33].

Chapter 3

Experimental Methods

In this chapter the main experimental techniques used in the production and characterization of the samples will be presented. All the magnetic thin films studied were prepared using reactive sputtering and their magnetic characterization was carried out through SQUID magnetometry. The structure and composition was analysed with Rutherford Backscattering Spectrometry (RBS), X-Ray Diffraction (XRD) and Conversion Electron Mössbauer Spectroscopy (CEMS).

3.1 Reactive Sputtering

The basic sputtering deposition process (fig. 3.1), consists in the evaporation of material from a target by bombarding it with energetic atoms [37; 38]. It is a technique known and used successfully for many years for deposition of different materials. In the case of reactive sputtering, the target is sputtered in the presence of chemically reactive gases that reacts with the target material in order to deposit a different chemical composition [39]. In the deposition chamber, the atmosphere is mainly composed of argon with controlled amount of the reactive gas, such as O_2 or N_2.

3.1.1 Magnetron Sputtering

Since basic sputtering relies mostly on secondary electrons to maintain a plasma in the chamber, the basic process is limited by the low ionization efficiency of

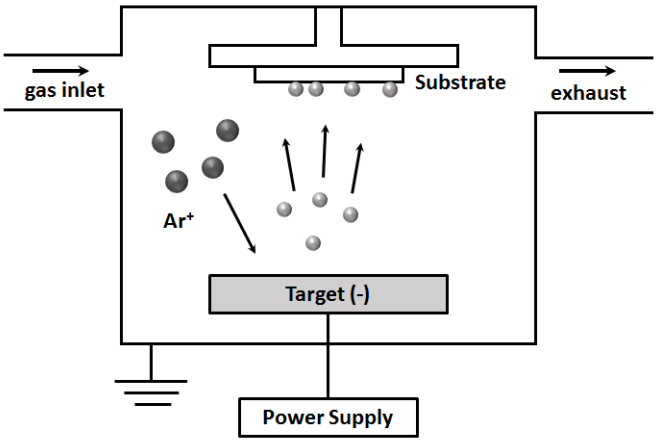

Figure 3.1: Schematic representation of a sputtering deposition system.

the plasma resulting in low deposition rates and high substrate heating effects. Magnetron sputtering was developed in order to overcome these limitations [40].

Magnetrons are designed to set a magnetic field parallel to the target surface in order to confine the secondary electrons to the vicinity of the target and substantially increase the probability of occurrence of an ionizing electron-atom collision. One magnetic pole is positioned at the central axis of the target and the second pole is a ring shaped magnet on the outer edge of the target (fig. 3.2). This geometry results in an increased efficiency for the formation of a dense plasma in the target region, yielding higher sputtering rates and, consequently, higher deposition rates [40].

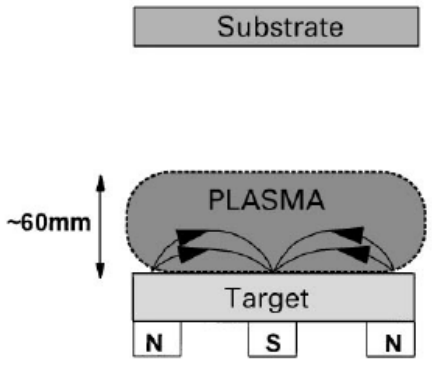

Figure 3.2: Schematic representation of a magnetron. Adapted from [40].

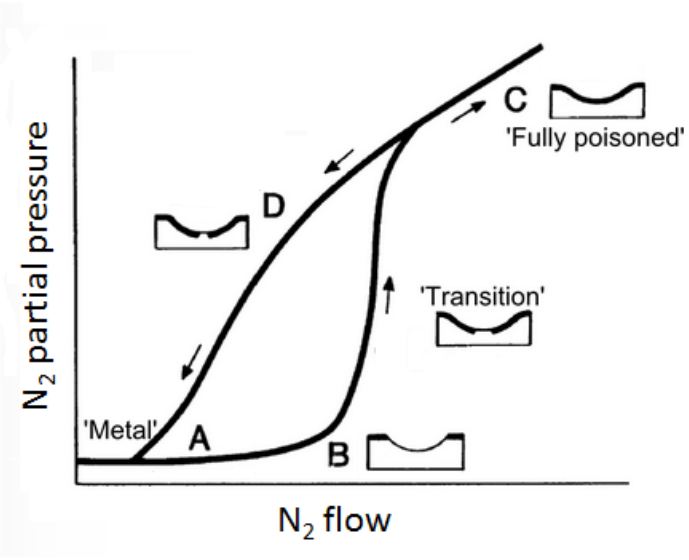

Figure 3.3: Hysteresis curve for reactive sputtering using mass flow control of the reactive gas (N_2). Adapted from [41].

Furthermore, the increased ionization efficiency achieved by this method allows the system to be run at lower operating pressures and lower operating voltages than in the basic sputtering configuration [40].

3.1.2 Flow control of the reactive gas

Ideally, the reaction between the reactive gas and the target material takes place only on the surface of the substrate. However, in reality it occurs not only on the substrate but also on the walls of the chamber and on the target leading to the formation of a compound at the target's surface. Since this compound has a significantly smaller sputtering rate than the one of the elemental target material, the coverage of the target results in a decrease in the deposition rate [41]. When the entire target surface is covered the target is said to be poisoned [42].

In a typical deposition of a nitride, the partial pressure of nitrogen evolves according to fig. 3.3. Keeping the target power constant as the flow of nitrogen into the chamber is increased, its partial pressure initially remains very low (fig. 3.3 - A) since most of the nitrogen reacts with the sputtered particles and is getter pumped. Above a certain threshold there is a sudden increase in partial pressure

(fig. 3.3 - B) indicating significant poisoning of the target surface with consequent drop in sputtering rate (less material available to combine with the reactive gas). As the gas flow increases the target becomes more poisoned until its surface is fully covered. Further increase in gas flow leads to a linear increase in the partial pressure [41].

After reaching the fully poisoned state, the partial pressure remains high even if the nitrogen flow is decreased and until the poisoning layer is broken through. Only then the sputtering rate increases.

It has been shown by different groups that it is also possible to control the partial pressure of the reactive gas directly during deposition, using different methods. Schiller *et al.* used an optical emission spectrometer signal from the sputtered material as the feedback signal and realized that the signal would decrease as the partial pressure of the reactive gas increases, due to the decrease in sputtering rate associated with the poisoning of the target [43]. Sproul and Tomashek integrated a mass spectrometer in the reactive gas partial pressure control system and modified it to provide a timely feedback signal to the control system [44]. Affinito and Parsons were the first to report the use of cathode voltage as a feedback signal. This method proved successful in the production of nitrides but hard to control for the case of oxides [45].

3.1.3 Reactive Sputtering Setup

The films studied in this work were produced at Instituto de Nanociencia de Aragón (INA) in Zaragoza. The system used is a TC Orion 5 UHV (fig. 3.4) with 5 magnetrons that work with targets of 2 inch of diameter, allowing great versatility of deposited material.

The base vacuum is typically below 10^{-7} Torr. It is equipped with two gas inlets which allow the entrance of Ar and O_2/N_2 in the chamber. The gas mixture is controlled by MKS100 gas flow-meters with maximum flow of 20 sccm. Working distance between magnetrons and sample holder is adjustable and in our case was set to 12 cm, with confocal arrangement. The sample holder's temperature can be varied from room temperature up to 400 ^{o}C. It can rotate to ensure uniform deposition for the entire substrate.

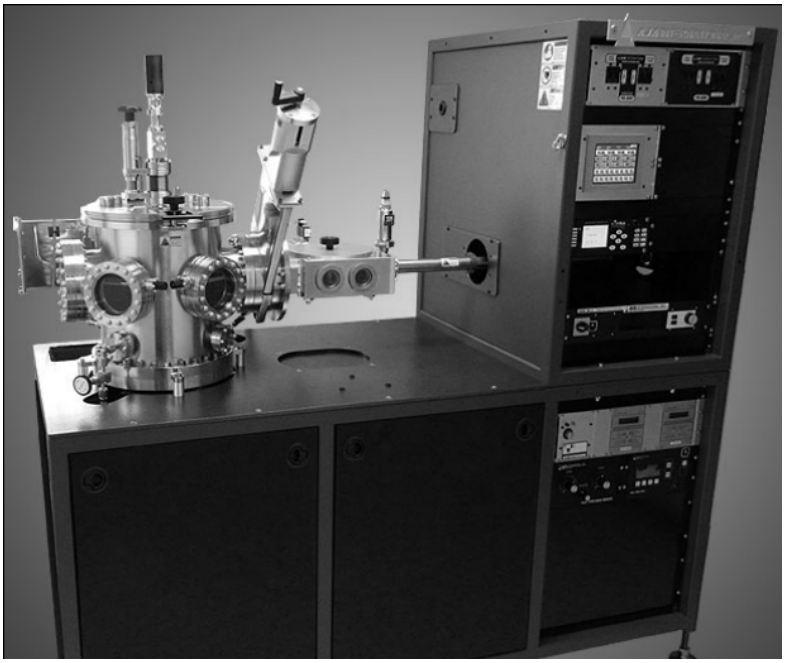

Figure 3.4: Reactive sputtering equipment present at INA.

The system is equipped with Phase II-J computer control system.

3.2 SQUID Magnetometry

The magnetic characterization of the samples was carried out using superconducting quantum interference device (SQUID) magnetometry. This technique has very high sensitivity and can detect magnetic moments as low as 5×10^{-10} A.m^2 (5×10^{-7} emu) due to the SQUID sensor.

3.2.1 System overview

In the present work, the magnetization measurements were performed using a Quantum Design MPMS SQUID for applied fields up to 5.5 T and temperatures between 2 K to 400 K.

The magnetometer consists essentially of a superconducting detection coil which couples inductively to the sample and is connected to a superconducting quantum interference device (SQUID) and a superconducting magnet to generate large mag-

netic fields and the temperature control is carried out by controlling cool or heated He flow. The location of the various components is shown in fig. 3.5.

3.2.2 Detection system

A measurement is performed by moving the sample through the system of superconducting detection coils which are connected to the SQUID by superconducting wires, allowing the current from the detection coils to inductively couple to the SQUID sensor (fig. 3.6), the whole system acting as an extremely sensitive magnetic flux-to-voltage converter. The detection coil itself consists of a single piece of superconducting wire wound in a set of three coils configured as a second-order (second-derivative) gradiometer [46]. This configuration is used to reduce the noise in the detection circuit that originates from fluctuations in the large magnetic field of the superconducting magnet.

As the sample moves through the superconducting detection coils, its magnetic moment induces an electric current in the coils, since the coils, the superconducting wires and the SQUID input coil form a closed superconducting loop.The change in the current of the detection system implies a variation of the SQUID output voltage, proportional to the magnetic moment of the sample. In a fully calibrated system, measurements of the voltage variations from the SQUID detector provide highly accurate measurements of the samples magnetic moment.

Given the SQUID's extreme sensitivity to fluctuations in magnetic fields, it is important that the sensor itself is shielded from both fluctuations in the ambient magnetic field and the large magnetic fields produced by the superconducting magnet. The necessary shielding is achieved through a superconducting shield which reduces the magnetic field to very low values in the region where the SQUID sensor is located.

3.3 Rutherford Backscattering Spectrometry

Rutherford Backscattering Spectrometry (RBS) has been used throughout this work for the characterization of the films and implanted single crystals. This technique is quite useful since it allows the quantitative determination of the com-

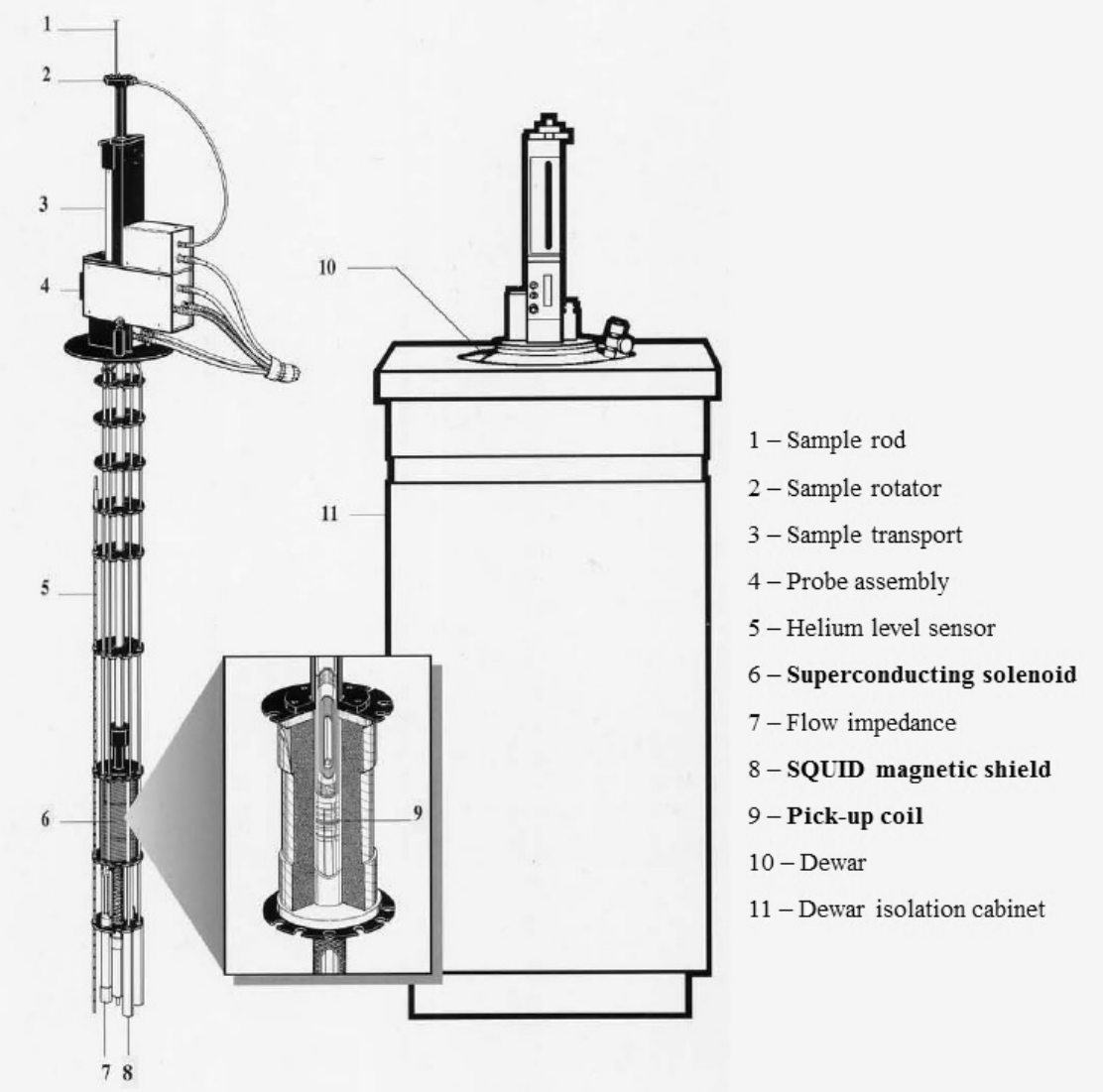

Figure 3.5: SQUID magnetometer system components (superconducting elements labelled in bold). Adapted from [46].

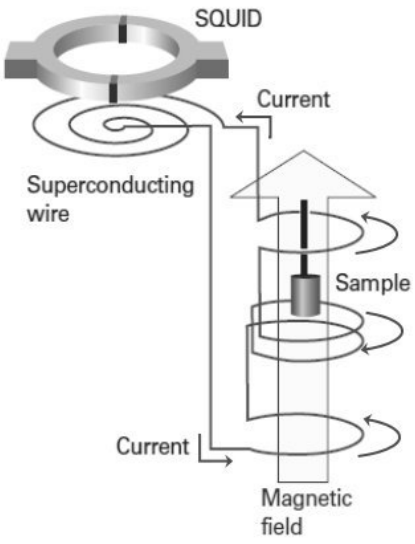

Figure 3.6: Basic structure of a SQUID magnetometer. Adapted from [47].

position of a sample, depth profiling of individual elements and determination of elemental areal density with minimal interference with the sample [48]. Taking advantage of the channelling effect, this technique can also assess the crystalline quality of the material and, in the case of thin films, study interface disorder and epitaxy.

3.3.1 Physical concepts

In RBS, the target to be analysed is bombarded with a beam of light ions with energies in the MeV range and the energy of the backscattered projectiles is recorded with an energy sensitive detector (typically a solid state detector) [49]. In the present work, the beam probe consisted of $^4He^+$ ions accelerated to 2 MeV by an electrostatic Van de Graff accelerator. The most often used scattering geometries are named Cornell and IBM. In the Cornell geometry the incident and exit beams are in the same plane as the axis of rotation of the sample. In the IBM geometry, the one used in this work, the incident beam, exit beam and surface normal of the target are in the same plane [49].

In fig. 3.7 we see an example of an RBS spectrum obtained for one of our thin

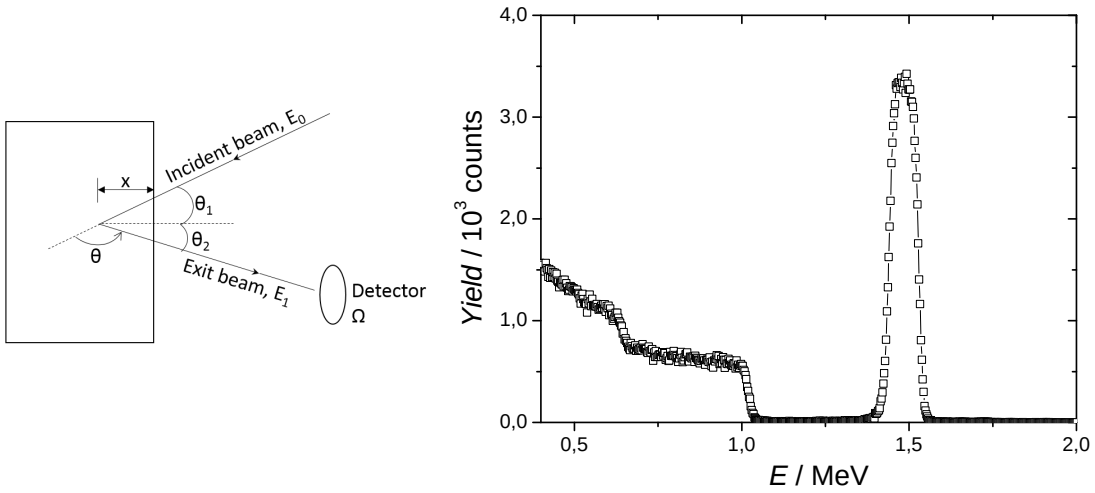

Figure 3.7: Schematic representation of a basic backscattering geometry (left) with θ being the scattering angle and example of RBS spectrum (right).

films of pure cobalt deposited on alumina. The width of the peak is caused by the different energy losses in the film material (convoluted with the energy response of the detection system) [48] and therefore is related with the film thickness and/or density.

The energy E_1 of a backscattered particle with mass m is related to the incident energy E_0, in the laboratory system, by

$$E_1 = KE_0 \tag{3.1}$$

where K, the kinematic factor, is given by

$$K = \frac{m^2}{(m+M)^2}\left\{\cos\theta + \left[\left(\frac{M}{m}\right)^2 - \sin^2\theta\right]^{1/2}\right\}^2 \tag{3.2}$$

m and M being, respectively, the masses of the probe and target nuclei ($m < M$) and θ being the scattering angle (fig. 3.7). Since θ, m and E_0 are usually set by experimental conditions the target elements, *i.e.* the target element masses M, can be identified. The energy separation ΔE_1 of particles backscattered by two

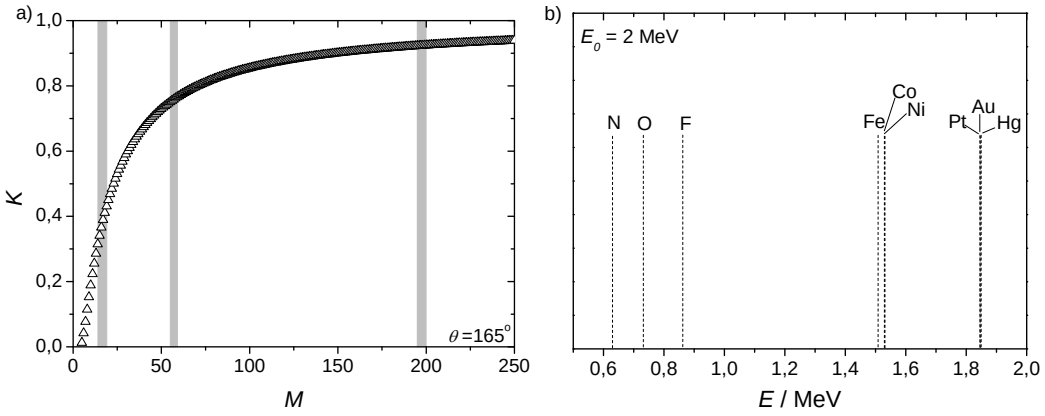

Figure 3.8: a) Kinematic factor as function of the mass of the target nucleus; b) Schematic representation of separation of energy of probe particles backscattered by three consecutive elements in different regions of the periodic table.

different target elements with mass difference ΔM is given by

$$\Delta E_1 = E_0 \frac{dK}{dM} \Delta M \tag{3.3}$$

Since the energy separation depends on dK/dM, the best energy separation and mass resolution are obtained for light target elements where $K(M)$ is the steepest and therefore dK/dM is large (fig. 3.8).

For a given scattering geometry, the number of backscattered particles collected by a detector spanning a solid angle Ω is given by

$$Y = Q\Omega N t \sigma \tag{3.4}$$

where Q is the number of incident particles, N and t are the atomic density and thickness of the target and σ is the scattering cross-section which, if the scattering is Rutherford scattering (*i.e.* pure Coulomb), can be calculated in the laboratory reference frame using

$$\sigma = 4 \left[\frac{Zze^2}{4E_0} \right]^2 \frac{\left[(1 - x^2 \sin^2\theta)^{1/2} + \cos\theta \right]^2}{\sin^4\theta (1 - x^2 \sin^2\theta)^{1/2}} \tag{3.5}$$

with $x = m/M$ and z and Z are the atomic numbers of the probe and target particles, respectively. The Rutherford cross-section is therefore essentially de-

pendent on the beam energy and the atomic numbers Z_p and Z_t. Since the term $[Z_t Z_p e^2/4E_0]^2$ is dominant this technique is more sensitive to heavy elements than to lighter ones, despite the smaller mass resolution for high masses.

3.3.2 Depth scale

When a particle travels through matter, it loses energy inelastically due to interactions with the target's electrons and nuclei. Many of the features of a RBS spectrum are determined by the energy losses of the probe particles as they traverse the target material since only a small fraction is scattered at the surface.

The stopping power of a material, for a given probe particle, is typically defined as the energy loss per distance travelled in the material and denoted as dE/dx. This quantity depends on the probe particle as well as on the target material and on the incident energy. Another useful quantity is the stopping cross-section [50],

$$\epsilon = \frac{1}{N}\frac{dE}{dx} \tag{3.6}$$

which is defined as energy loss probability per atom, N being the atomic density of the target.

If a scattering event occurs inside the target, the energy immediately before the collision is given by

$$E = E_0 - \int_0^d \frac{dE}{dx} dx \tag{3.7}$$

To evidence the depth at which scattering occurs, it is convenient to express the energy loss during the ingoing path, prior to collision, at a depth x, as

$$\Delta E_{in} = \int_0^{x/\cos\theta_1} \frac{dE}{dx} dx \tag{3.8}$$

and given that our attention is typically confined to particles that travel very small distances in the surface layers of the target, the rate of energy loss can be considered to be constant and equal to $dE/dx|_{E_0}$, *i.e.* the value at the energy of

the incident ion beam [50]. The previous expression can then be written as

$$\begin{aligned}\Delta E_{in} &= \frac{x}{\cos\theta_1}\left.\frac{dE}{dx}\right|_{E_0} \\ &= \frac{x}{\cos\theta_1} N\epsilon(E_0)\end{aligned} \tag{3.9}$$

ΔE_{out} can be determined analogously considering the outward path, in which the distance traversed is $x/\cos\theta_2$ (see fig. 3.7), and the rate of energy loss after scattering by element of mass M, retaining a fraction K of the energy with which it reached depth x, is constant and equal to KE_0.

From eqs. 3.6 - 3.8, the energy difference between particles scattered at the surface and at a depth x is then given by

$$\begin{aligned}\Delta E &= K\Delta E_{in} + \Delta E_{out} \\ &= K\left[\frac{x}{\cos\theta_1} N\epsilon(E_0)\right] + \left[\frac{x}{\cos\theta_2} N\epsilon(KE_0)\right] \\ &= Nx\,[\epsilon]\end{aligned} \tag{3.10}$$

depends on the target density and on $[\epsilon]$, defined as

$$[\epsilon] = \frac{K}{\cos\theta_1}\epsilon(E_0) + \frac{1}{\cos\theta_2}\epsilon(KE_0) \tag{3.11}$$

Any energy difference can be converted into a depth x using the atomic density of the target in equation (3.10), allowing to determine the thickness of a specimen through the width of the RBS profile relative to an element present in the sample. However, reliable information about the physical depth in the host can only be obtained if the host density value is reliable since RBS truly yields the elemental areal density (the product 'Nx' not 'N' and 'x' separately)

In summary, the energy of backscattered particles depends both on the mass of the target element and the depth at which the scattering occurs, allowing the identification of the elements present in the specimen as well as in-depth compositional analysis. The mass resolution is determined by the kinematic factor and

decreases with increasing target mass. However, since the yield is determined by the scattering cross-section, which depends basically on the square of the atomic numbers, this technique's sensitivity increases for heavier elements. Analysis of light elements in heavy hosts is difficult since it implies extraction of small signals overlapping large backgrounds due to the heavier host elements.

In the present work, the quantitative analysis of the RBS spectra was achieved through comparison of the experimental data with simulated spectra obtained using the RUMP© code[51].

3.3.3 RBS Channelling

RBS channelling is a technique which can be used to assess the crystalline order of a specimen by aligning the incident beam with one of the principal directions of the crystal structure. In alignment conditions the probe particles are steered by the periodic potential along the rows or planes of lattice atoms and effectively channelled through the matrix leading to a decrease in RBS yield. The presence of impurities or defects in the matrix will disrupt the periodicity and cause dechannelling of the probe particles causing the yield to increase. The crystalline quality of a single crystal can be evaluated by comparing the yield obtained in aligned and random conditions (fig. 3.9).

RBS channelling is of particular importance for thin film analysis, since it allows to assess the quality of the epitaxial growth. This evaluation is done by acquiring multiple spectra at different tilting angles in relation to the incident beam and integrating sections of the spectra that contain elements exclusive to the film and exclusive to the substrate (fig. 3.10 a)).

Comparing the results obtained for the film and the substrate, it is possible to determine if the substrate's channelling direction is also a channelling direction for the film and if so, the relative reduction in yield observed gives information on the quality of the epitaxy of the film (fig. 3.10 b)).

3.3.4 RBS system

The RBS analyses presented in this work were performed in Laboratório de Aceleradores e Tecnologias de Radiação of Campus Tecnológico e Nuclear - Instituto

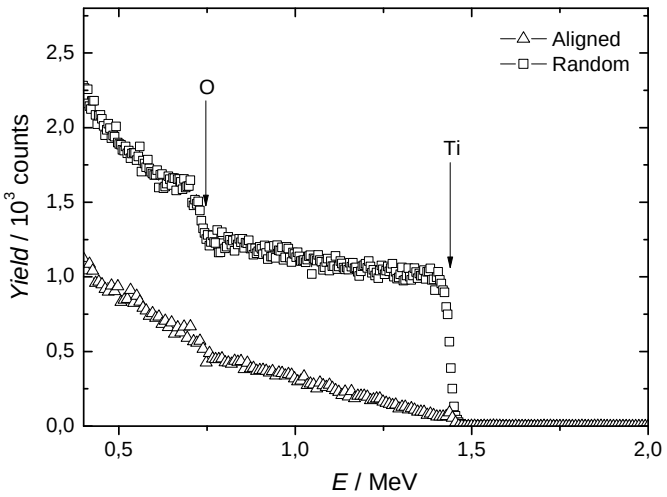

Figure 3.9: RBS spectra of a single crystal of TiO_2 in alignment and random conditions.

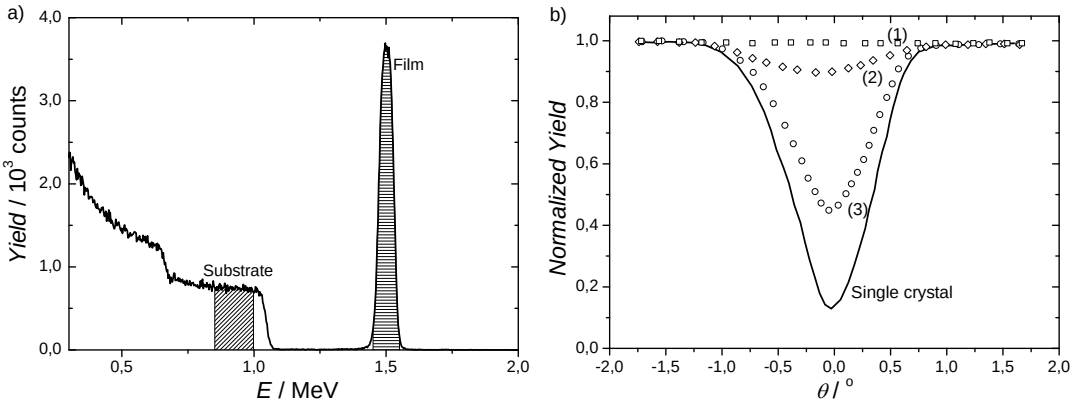

Figure 3.10: a) Example of a spectrum obtained for a specific angle, with the integrated regions for the film and substrate marked. b) Normalized yield as a function of angle for a single crystalline substrate, a non epitaxial film (1), an epitaxial film with poor crystalline quality (2) and an epitaxial film with good crystalline quality (3).

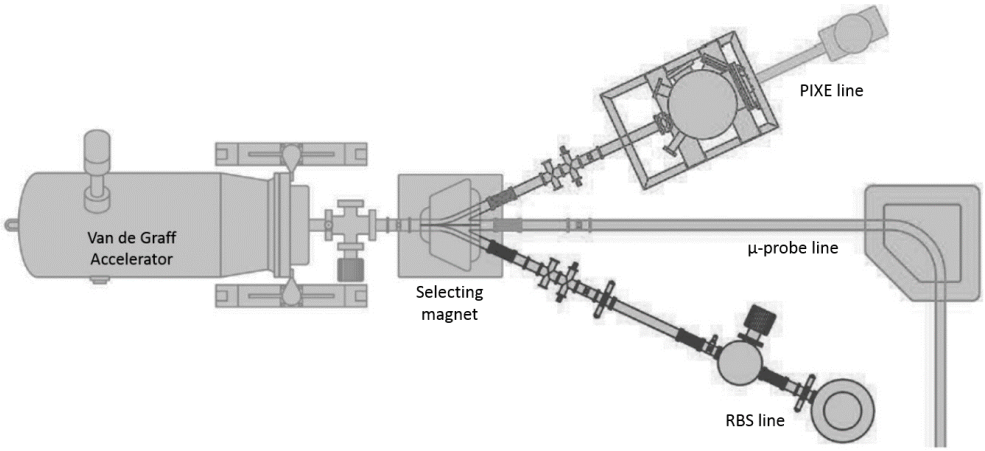

Figure 3.11: Schematic representation of the ion beam setup present in Unidade de Física e Aceleradores of Campus Tecnológico e Nuclear - Instituto Superior Técnico.

Superior Técnico. In the setup used, the ion beam is accelerated using a Van de Graff accelerator, which is a horizontal electrostatic accelerator, with the ability to achieve terminal voltages up to 2.5 MV and produce ion beams of helium (He^+) and hydrogen (H^+) with energies up to 2.5 MeV.

In order to create the ion beam, a radio frequency ion source is located inside the terminal and connected to different gas sources so that the desired ion can be selected. The ionization of the gas is assisted by a radio frequency antenna of 125 MHz frequency and 60 W power. After going through the accelerator tube, the beam passes through collimators to ensure its path and limit its divergence.

In this system, the ion beam created in the accelerator can be directed for one of three different beam lines associated to different experiments (fig. 3.11). The schematic representations of the RBS setup presented are courtesy of Norberto Catarino.

In the RBS line, the beam passes through a second set of collimators, to guarantee reduced divergence. In the chamber, three solid state particle detectors are present in the IBM geometry: the detector placed at -140° is a conventional PIPS detector[1], while the detectors placed at ±165° are Si-pin diodes[2]. A schematic

[1]Passivated Implanted Planar Silicon detectors.

[2]A PIN diode is a diode with a wide, undoped intrinsic semiconductor region between a p-type semiconductor and an n-type semiconductor region. The wide intrinsic region is in contrast

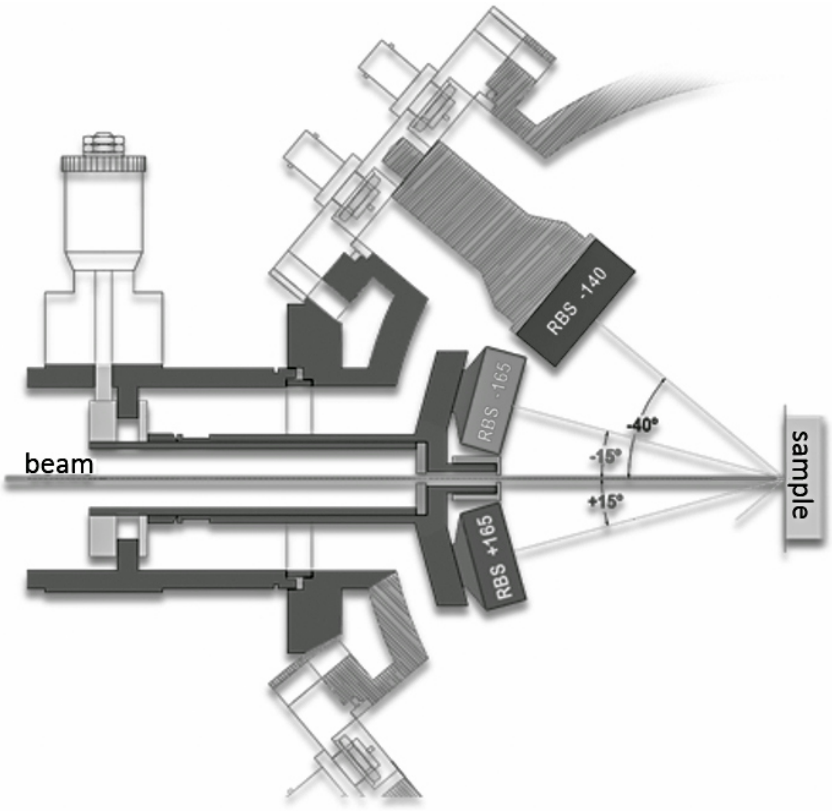

Figure 3.12: Schematic representation of the RBS chamber.

representation of the RBS chamber is presented in fig. 3.12.

to an ordinary PN diode. The wide intrinsic region makes the PIN diode an inferior rectifier (one typical function of a diode), but it makes the PIN diode suitable for attenuators, fast switches, photodetectors, and high voltage power electronics applications.

3.4 X-Ray Diffraction

X-ray diffraction is a very important non-destructive tool to analyse crystal structures since X-rays have wavelengths of the same order of magnitude as the crystal lattice.

X-ray diffraction can be described as the interference between X-rays elastically scattered from the atoms of the crystal[28].

Although the photon scattering is not necessarily elastic, the elastic scattering of X-rays is the main process exploited for structural investigations and it suffices to adopt an essentially classical approach for its description.[1]

The intensity of the radiation diffused by one electron at a distance r is given by

$$I(r) = I_0 r_0^2 \frac{K_1 + K_2 \cos^2(2\theta)}{r^2} \tag{3.12}$$

where $r_0 = \frac{e^2}{4\pi\epsilon_0 mc^2} = 2.82 \times 10^{-5}$ Å is the Thomson scattering length, I_0 is the intensity of the incident beam, 2θ is the scattering angle and K_1 and K_2 are fractions of the incident field amplitude perpendicular and parallel, respectively, to the scattering plane defined by the incident and scattered beams.

For an atom, the scattering is due to all atomic electrons that are added in the atomic form factor which represents the scattering power of the atom. It can be calculated as the integral of the electronic charge distribution $\rho(\vec{r})$ weighted by the corresponding phase factors

$$f_a(\vec{q}) = \int \rho(\vec{r}) e^{i\vec{q}\cdot\vec{r}} d\vec{r} \tag{3.13}$$

and is recognized as the Fourier transform of the electronic charge density of the atom.

In a standard diffractometer the specimen under study is irradiated by a collimated beam of monochromatic X-rays with wave vector $\vec{k}$ resulting in scattered rays in the directions of constructive interference as beams with wave vector $\vec{k}'$

[1] In a quantum mechanical approach (incident photon with a momentum of $\hbar\vec{k}$ and energy $\hbar\omega$) part of the photon's energy may be transferred to an electron resulting in a scattered photon with lower frequency than the incident one (inelastic diffraction).

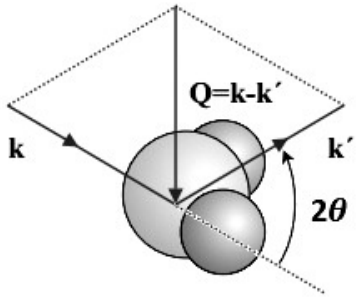

Figure 3.13: Schematic representation of scattering from a molecule. Adapted from [52].

and $\left|\vec{k}\right| = \left|\vec{k}'\right|$ (fig. 3.13).

The contribution of all atoms in a crystal (structure factor) can be determined, assuming each atom as a scattering centre, as

$$\begin{aligned} F_{cystal}(\vec{q}) &= \sum_{\vec{r_j}} f_a^j(\vec{q}) e^{i\vec{q}\cdot\vec{r_j}} \sum_{\vec{R_n}} e^{i\vec{q}\cdot\vec{R_n}} \\ &= F_{uc}(\vec{q}) \sum_{\vec{R_n}} e^{i\vec{q}\cdot\vec{R_n}} \end{aligned} \tag{3.14}$$

where $\vec{q}$ is $\vec{k}' - \vec{k}$, F_{uc} is the unit cell structure factor and the last factor is the lattice sum. All terms in the lattice sum presented in equation (3.14) are phase factors located on the unit circle in the complex plane, and so the sum will be on the order of unit except for scattering vectors fulfilling

$$\vec{q} \cdot \vec{R_n} = 2\pi n \tag{3.15}$$

where n is an integer, in which case the sum becomes of order N (the number of unit cells). Equation (3.15) implies that $\vec{q}$ is a vector of the reciprocal lattice $\vec{Q}$. This is the Laue condition for observation of X-ray diffraction from a crystal lattice:

$$\vec{q} = \vec{Q}_{hkl} \tag{3.16}$$

It can be shown that for each point of the reciprocal lattice (h, k, l) there exists

a set of planes in the direct lattice, the planes with Miller indices (h, k, l), perpendicular to $\vec{Q}_{hkl}$. Also $\left|\vec{Q}_{hkl}\right| = 2\pi n/d_{hkl}$ where d_{hkl} is the interplanar distance between (h,k,l) planes and n is an integer.

Since $|\vec{q}| = 2\left|\vec{k}\right| \sin\theta$ (fig. 3.13) and $\left|\vec{k}\right| = 2\pi/\lambda$, it is easy to see that the Laue condition for diffraction contains the Bragg's formula for diffraction

$$2d_{hkl} \sin\theta = n\lambda \tag{3.17}$$

where λ is the X-ray wavelength.

3.5 Atomic Force Microscopy

In this work, atomic force microscopy (AFM) has only been used to obtain information on the surface roughness of the films produced. For this reason, a very brief description of the working principles of AFM is given. A more comprehensive and detailed description can be found, for example, in [53].

In AFM, the measurement is performed by tracking the movement of a oscillating probing tip that is attached to a cantilever-type spring. Typical values for the spring constant of the cantilever vary between 0.001 and 100 N/m. The sample is set on a piezotube which controls movement on the xOy plane. The interaction between the tip and the sample's surface is registered by the deflection in the cantilever (fig. 3.14). In order to measure this deflection an optical system is used. At zero deflection a laser is focused on the tip's edge and its reflection centred in a photodetector. Any deflection in the cantilever causes a deviation of the reflected beam providing the means to measure the deflection. The xy position of the sample combined with the information obtained from the tip allows the production of a topographic map of the sample.

The measurements can be done in contact or non-contact mode. In non-contact mode a distance ranging from 10 to 100 nm is maintained between sample and tip and forces such as van der Waals, electrostatic or magnetic forces can be sensed and used to provide information about surface topography charge distribution and magnetic domain wall structure. In contact mode, ionic repulsion forces allow high resolution in the mapping of surface topography. Also, frictional forces and plastic

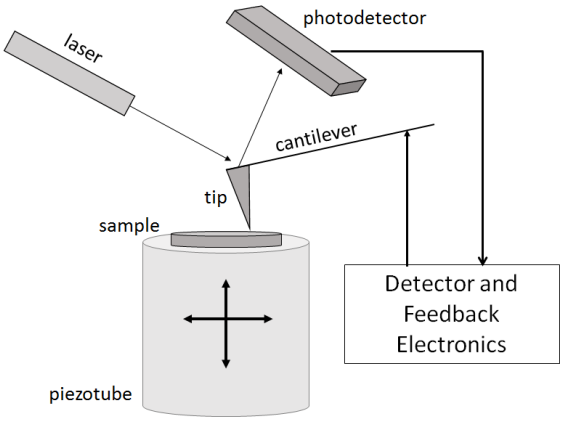

Figure 3.14: Schematic representation of AFM.

and elastic deformation can be assessed.

3.6 Mössbauer Spectroscopy

Mössbauer is a versatile spectroscopy technique that accesses the hyperfine structure of nuclear energy levels by studying the modification in the energy of absorbed gamma rays or emitted conversion electrons. It is characterized by a high energy resolution of the order of 1 in 10^{12} (corresponding in the case of the isotope 57Fe gamma of 14,4 keV to a spread of 4.67×10^{-9} eV). Since the experiments were not carried out directly by me only a quick overview of the information obtained from the spectra is given here.

Typically there are three types of nuclear interactions that are observed:

- Isomer shift
- Quadrupole splitting
- Magnetic hyperfine splitting

The isomer shift (δ) originates from the Coulomb interaction of the negatively charged electron density and the nuclear charge distribution within the nuclear volume of radius R in the excited and ground states. Given that , in general, the nucleus volume depends on the energy state, there is an energy shift related with

the electronic charge density in the nucleus. So, it describes a shift in the nucleus resonance energy due to the electrons in s orbitals.

An asymmetric charge distribution around the nucleus gives rise to an asymmetric field at the nucleus, characterized by the electric field gradient tensor (EFG), ΔE. The electric quadrupole interaction between the nuclear moment and the EFG gives rise to quadrupole splitting in the nuclear energy levels. Magnetic hyperfine splitting results from the dipole interaction between the nuclear spin moment and a magnetic field, and is also known as nuclear Zeeman effect. The energy levels of a nucleus under the effect of a magnetic field, which may arise from different contributions (from the atom itself, the lattice through crystal field effects and also from external applied fields) will split into non-degenerate sub-levels. The splitting of the magnetic sublevels is directly proportional to the magnetic field present in the nucleus and therefore the splitting of the lines in the spectrum gives a direct measure of the internal field.

3.6.1 Conversion Electron Mössbauer Spectroscopy

A standard Mössbauer spectrometer consists of a source and an absorber (the sample, in transmission geometry), a drive system to provide the movement of the source relative to the absorber and a detector with a counting system. If the absorber is too thick or mounted on an opaque substrate that prevents the radiation to pass through or greatly reduces the signal, then a reflective technique, such as Conversion Electron Mössbauer Spectroscopy (CEMS), must be used.

The de-excitation of a nucleus excited by gamma ray absorption can occur by emission of a gamma ray, with probability $N(\gamma)$, or by internal conversion and ejection of an electron, with probability $N(e)$. The ratio of these two processes is given by the internal conversion coefficient expressed as

$$\alpha = \frac{N(e)}{N(\gamma)} \tag{3.18}$$

which for ^{57}Fe is 8.21 and therefore spectra obtained through detection of conversion electrons have much higher efficiency than gamma detection if both can be detected. Since electrons are charged particles, CEMS is limited to near surface analysis because the conversion electrons produced by a resonant event have a

small range in the material (≈100 nm), due to interactions with other charged particles.

The CEMS measurements presented in this work were carried out by L. Ferreira and M. D. Carvalho from Centro de Física da Matéria Condensada and Centro de Química e Bioquímica of Faculdade de Ciências de Lisboa, respectively.

3.7 X-Ray Absorption Spectroscopy

Extended X-Ray Absorption Fine Structure (EXAFS) and X-ray Absorption Near Edge Structure (XANES) are two techiques that explore the energy spectrum obtained with X-Ray Absorption Spectroscopy (XAS). XAS consist in the measurement of the X-ray absorption coefficient μ(E) of a material as a function of energy, using an X-ray beam with a narrow energy resolution. The absorption coefficient, expressed as

$$\mu = -\frac{d \log I}{dx} \tag{3.19}$$

where x corresponds to the traversed distance and I corresponds to the intensity, describes the relationship between the intensity of an incident X-ray beam and the intensity of the transmitted beam after travelling a distance x within the sample.

When the energy of the X-ray matches the binding energy of the electrons of atoms in the sample the absorption of the X-rays increases and consequently the intensity of the transmitted wave diminished, resulting in what is called an absorption edge. Each element has a set of distinct absorption edges, giving XAS element sensitivity.

XANES spectra are obtained near the absorption edge and give information regarding the local coordination of the element and the oxidation state, since different energy edges of many elements exhibit shifts associated with the oxidation state. Comparison of XANES spectra of an "unknown" sample with spectra obtained from known standards, combined with linear combination fitting of several appropriate different known standard spectra allows the technique to provide an estimate of the composition of the sample.

EXAFS corresponds to the oscillatory part of the XAS that extends to about

1000 eV above the absorption edge of a particular element of the sample. The observed oscillations in the spectra are associated with wave interactions between the ejected photoelectron and electrons surrounding the absorbing atom, with maxima in the oscillations resulting from constructive interference between these waves, and minima resulting from destructive interference. If properly interpreted, these spectra can provide information on interatomic distances and coordination numbers [54]. Since EXAFS requires a tunable x-ray source, data are always collected at synchrotrons, often at beamlines which are especially optimized for the purpose.

The measurements performed in this work were done by C. Meneghini and I. Carlomagno from the Dip. di Scienze of Università di Roma using fluorescence geometry at the BM23 beam line at the ESRF synchrotron radiation facility (Grenoble, France).

3.8 X-Ray Reflectivity

X-Ray Reflectivity (XRR) is a surface sensitive analytical technique used to characterize surfaces, thin films and multilayers [55].

This technique consists in analysing X-ray reflection intensity curves from grazing incident X-ray beams to determine thin film characteristics such as thickness, density and surface or interface roughness.

Electromagnetic waves upon incidence on a surface generate a specular reflected wave, a refracted wave and diffuse reflections. In the case of X-ray waves, the relative refractive index is slightly below 1 [56] and therefore X-rays undergo total reflection upon incidence on a flat surface at a grazing angle below the critical angle θ_c.

In a substrate covered by a film of different electron density, interference occurs between the X-rays reflected from the surface of the film and those reflected by the interface between the film and the substrate. An example of an XRR measurement performed on Au deposited on Si is shown in fig. 3.15 evidencing the dependence of the period of the oscillations on the film thickness. In this work, this technique was used to determine the films' thickness.

The amplitude of the oscillations and the critical angle for total reflection

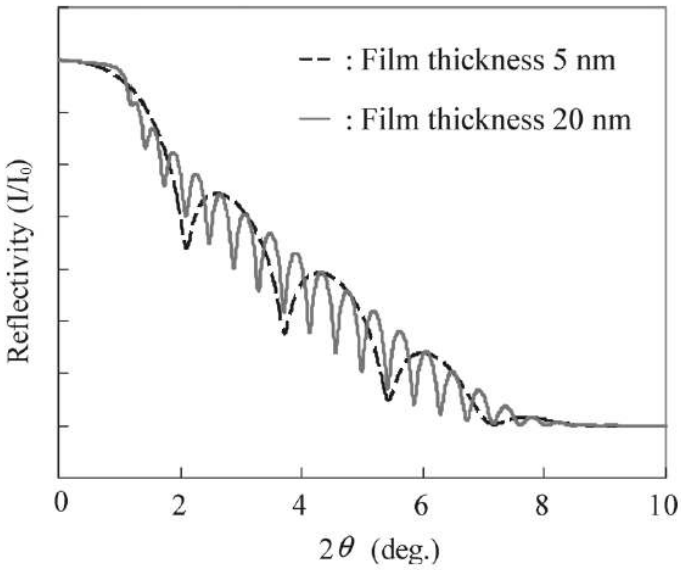

Figure 3.15: XRR measurements obtained for Au films with different thicknesses deposited on Si substrate. Adapted from [56].

provide information on the density of the films. The greater the difference between the density of the substrate and the density of the film, the higher the amplitude of the observed oscillations. The roughness of the surface and the interface roughness between the film and the substrate also have an effect on the oscillation pattern. Fig. 3.16 illustrates how film thickness, density and roughness affect the XRR curve.

The XRR measurements presented in this work were performed by P. Ferreira from CICECO, Departamento de Engenharia de Materiais e Cerâmica of Univeridade de Aveiro.

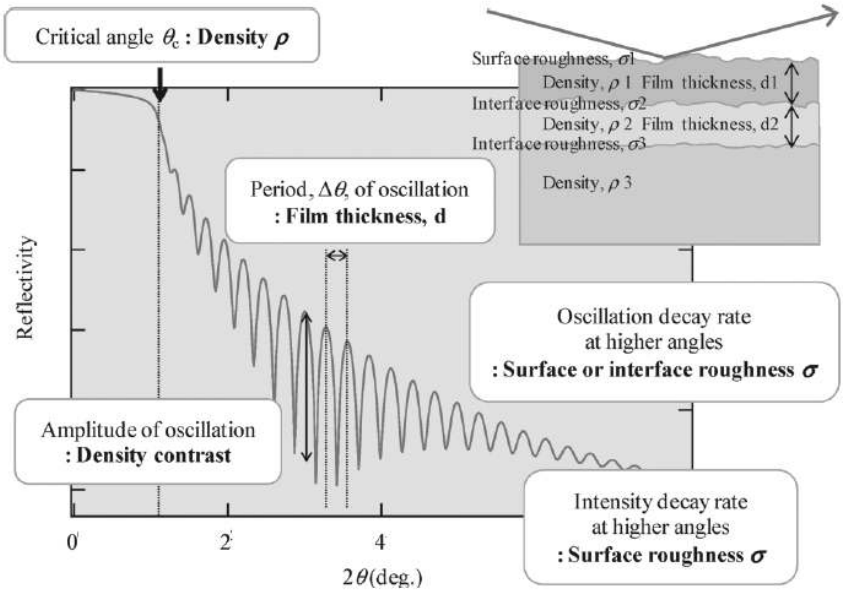

Figure 3.16: Summary of information extracted form XRR measurements [56].

Chapter 4

Co-N thin films

4.1 Introduction

As already stated in the introduction the two main phases to be explored for Co-N films are Co_3N and Co_4N. From these two phases, Co_4N is the one proposed to have higher magnetization and spin polarization. Co_4N is a challenging material. It was never observed as a stoichiometric compound and until now the maximum nitrogen content obtained in the cubic phase is indicated to be $Co_{16}N$ [26]. With this low nitrogen content the cubic structure is very close to that of fcc-Co ($\Delta a/a_{Co} \approx 1$ %) and the identification of the nitride is very difficult. Also, it is the least temperature resistant cobalt nitride, decomposing into Co_3N and α-Co(N) at approximately 270 ^{o}C [6; 7; 57]. In fact, it was observed that using rapid thermal annealing at gradually higher temperatures (between 400 ^{o}C and 700 ^{o}C) for 5 minutes it is possible to obtain a gradual loss of nitrogen resulting in a stepwise decomposition in a sequence

- $Co_4N \rightarrow Co_3N + \beta$-Co(N)
- $Co_3N \rightarrow Co_2N + \beta$-Co(N)
- $Co_2N \rightarrow CoN + \beta$-Co(N)

with CoN being the most stable compound.

The work done on Co-N thin films has been the subject of two papers already published, whose essential part is included as sub-sections 4.3.1 and 4.3.2 under permission of Elsevier. The respective papers can be found in references [58; 59].

4.2 Experimental details

In this work, thin films of Co-N were first deposited on glass substrates with different deposition conditions in order to determine the best conditions for cobalt nitride growth using reactive sputtering. Depositions using the optimal deposition conditions were then performed using single crystalline substrates (Al_2O_3 (0001), Al_2O_3 (11$\bar{2}$0), MgO (100), MgO (110), TiO_2 (100) and TiO_2(110)) in order to study the influence of the substrate on the growth and properties of the films.

For the films deposited on glass, the depositions were carried out in plasma forming media Ar+N_2 with different partial pressure (PP) of N_2 (N_2/Ar+N_2 = 0, 5, 10, 15, 20 %), having a base pressure in the chamber of 5×10^{-5} mTorr and a total pressure of the mixture Ar+N_2 during deposition of 10 mTorr. During the deposition process the substrates were mounted on a rotating sample holder, situated at 120 mm from the magnetron, to ensure a uniform distribution of the deposited material. The substrates were kept at 250 ^{o}C during deposition. The direct current power was 100 W. The samples of this group will be referenced by the nitrogen PP used as CoN#, where # represents the percentage of nitrogen present in the reactive plasma forming media during deposition (#=0, 5, 10, 15, 20).

The deposition conditions determined by the study of films deposited on glass were the ones used for the films deposited on single crystalline substrates: 10 and 15%, keeping the temperature at 250 ^{o}C and the DC power at 100 W. The nomenclature for this group of samples is similar, with the samples being referenced by the nitrogen PP and substrate used as substrate/CoN#, with # being 10 or 15 in this case.

The films' structure and composition were studied by X-Ray Diffraction (XRD) in $\theta - 2\theta$ geometry using Cu-Kα radiation (λ = 0.15418 nm) and Rutherford Backscattering Spectrometry (RBS) performed with a 2 MeV $^4He^+$ beam. The thickness and morphology of the films were analysed by Atomic Force Microscopy

(AFM) in AC mode. Magnetic characterization of the samples was performed using Superconducting Quantum Interference Device (SQUID) magnetometry in a temperature range from 10 K to 300 K and in magnetic fields up to 0.1 T.

For the films deposited on single crystalline substrates, in order to have deep information about the Co local atomic structure, X-ray absorption fine structure (EXAFS) experiments were carried out C. Meneghini and I. Carlomagno from the Dip. di Scienze of Università di Roma.

4.3 Results and Discussion

4.3.1 Co-N thin films deposited on glass

[1]

In order to confirm the incorporation of nitrogen in the films during deposition, RBS analysis was performed. The results are presented in Fig. 4.1 where two arrows mark the channels corresponding to the positions of Co and N at the films surface. It is difficult to observe the nitrogen profile in the RBS spectra due to the large amount of oxygen - major component of the underlying substrate - which contribution appears very close to that of the nitrogen; oxygen thus contributes a dominant background making it difficult to resolve the nitrogen profiles. However, following the variations in shape and intensity of the Co peak with increasing $\frac{N_2}{Ar+N_2}$ one can infer the presence of N_2 and estimate the composition of the films from the RBS results. An increased content of nitrogen is associated with a lower Co yield at the same depth. The spectra were compared with theoretical simulations of RBS results for different target compositions, obtained using the RUMP© software [60], allowing to conclude that films CoN5 and CoN10 contain approximately 9 at.% of incorporated nitrogen while films CoN15 and CoN20 have higher nitrogen content, approaching 13 at.% (see 4.1). For the film CoN0, without nitrogen, the cobalt surface atomic density was estimated from the simulations to be 4.8×10^{17} at/cm^2. For the other films, the relative surface atomic density to CoN0 was obtained directly from experimental results using the ratio of the areas of the Co peaks in the corresponding RBS spectra.

[1] This sub-section is a part of [58].

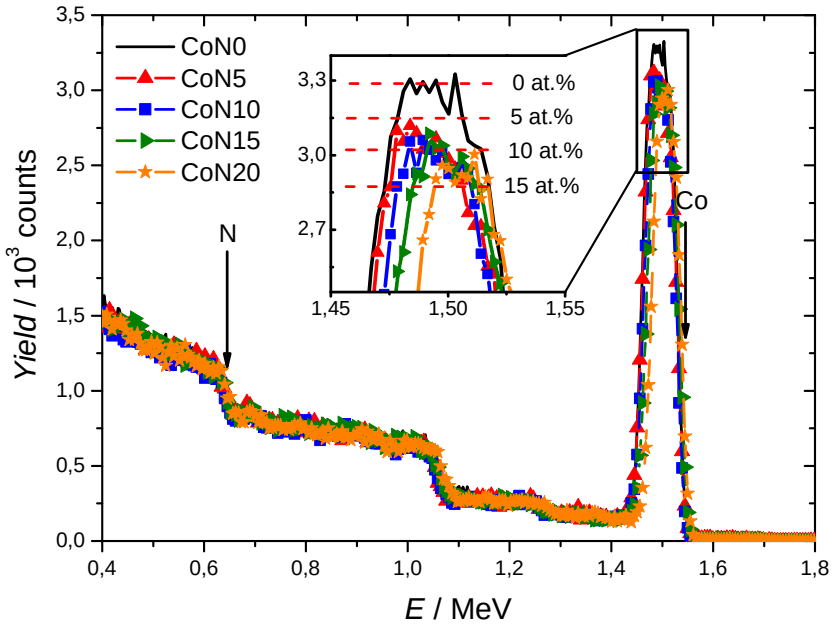

Figure 4.1: RBS spectra obtained for the different samples. Vertical arrows mark the position of the elements cobalt and nitrogen at the films surface. In the inset the detail of the Co profiles is shown and dashed lines mark the simulated Co yield obtained for different atomic concentrations of nitrogen in the film.

AFM measurements were used to determine the thickness and roughness of the films. Combining the thickness values with the surface density of cobalt ions obtained from RBS results, the volume density of the films was calculated (see Table 4.1). For the films deposited in pure Ar, the cobalt density is much smaller than the value for bulk cobalt (approximately 9.1×10^{22} at/cm^3) indicating that the deposition method favours low density aggregation of Co grains. For CoN5, total atomic density increases relative to CoN0, which is expected from incorporation of interstitial nitrogen in a cobalt structure, but decreases for other films with the increase of the PP of N_2 in plasma forming media. It was also observed that all films present similar roughness (6±2 nm), indicating that the density results are not a consequence of granular size.

Fig. 4.2 shows the XRD patterns for the films under investigation. Given that CoN0 was deposited in pure Ar, this film is used as a reference. The diffraction pattern for CoN0 allows us to conclude that the film is fine polycrystalline with the size of reflecting blocks below the spatial resolution of the instrument, this

Table 4.1: Film thickness and atomic density. The thicknesses were determined by AFM measurements and the surface cobalt atomic density from RBS results. The atomic density was calculated combining both results.

Sample	**Thickness (nm)**	**Co Surface Atomic Density** (10^{17} **Co/cm^2**)	**Co Atomic Density** (10^{22} **Co/cm^3**)	**Total Atomic Density** (10^{22} **at/cm^3**)
CoN0	80 ± 1	4.8 ± 0.1	6.0 ± 0.05	6.0 ± 0.05
CoN5	83 ± 1	4.7 ± 0.1	5.7 ± 0.05	6.3 ± 0.05
CoN10	84 ± 1	4.6 ± 0.1	5.4 ± 0.05	6.0 ± 0.05
CoN15	84 ± 1	4.3 ± 0.1	5.2 ± 0.05	5.9 ± 0.05
CoN20	85 ± 1	3.8 ± 0.1	4.5 ± 0.06	5.2 ± 0.05

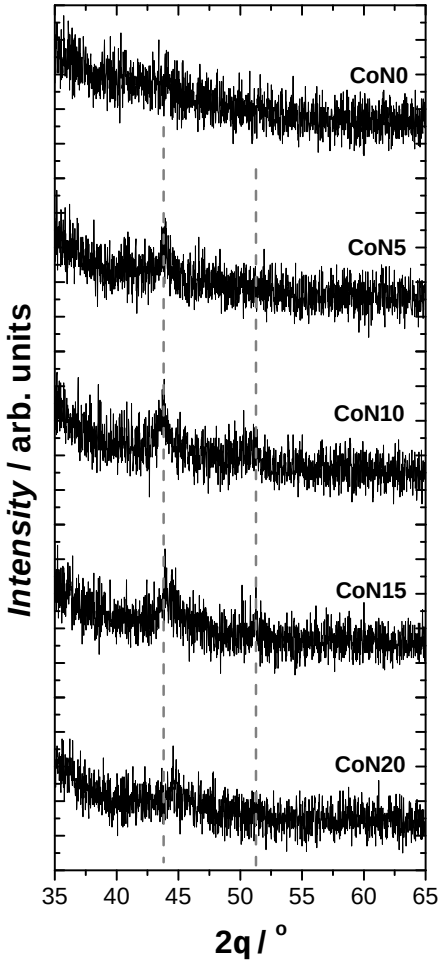

Figure 4.2: $\theta - 2\theta$ XRD patterns obtained for the different films studied. The dashed lines mark the position of the peaks observed for CoN10 and CoN15.

kind of structure being characterized as nano-crystalline. This may be caused by the fact that Co, in thin films, is usually represented by a fine mixture of fcc and hcp phases. XRD patterns for samples CoN5, CoN10, CoN15 and CoN20 are qualitatively different, *i.e.* two broad peaks are observed for the films CoN10 and CoN15, respectively at 43.6^o and 50.9^o, the position of the diffraction peaks being marked by dashed lines in Fig. 4.2. The first peak is also visible in the results for film CoN5. Both diffraction peaks can be assigned to $Co_{4+x}N$ phase ($Co_{5.47}N$: ICDD #00-041-0943). For CoN20, the second peak disappears while the first peak observed is slightly shifted to higher 2θ position, modification compatible with the formation of Co_3N in this film (ICDD #00-006-0691). The atomic density evolution can be compared with the evolution of calculated densities assuming the formation of the cobalt nitride phases referred. Using the lattice parameters in the ICDD files, the values 8.6×10^{22} Co/cm^3 for $Co_{5.47}N$ and 7.5×10^{22} Co/cm^3 for Co_3N are obtained, respectively. This corresponds to 95% and 82% of pure cobalt density. The decrease in cobalt ions density agrees with the experimental results of Table 4.1.

The magnetization results are presented in Fig. 4.3 as magnetic moment per cobalt ion, the number of cobalt ions being obtained by the surface atomic density multiplied by the film's area. The reference film, CoN0, presents the saturation magnetization close to the one for bulk cobalt, i.e. 1.7 μ_B per Co atom [61]. The smaller saturation magnetic moment observed for films CoN5, CoN10 and CoN15, compared to the reference value of CoN0, and the fact the saturation magnetic moment does not change significantly with PP of N_2 for these three films is consistent with the formation of a $Co_{4+x}N$ phase detected by X-ray diffraction. A smaller magnetic moment is measured for film CoN20, consistent with the presence of Co_3N phase, as inferred from the XRD patterns. The magnetization values obtained for these films are in good agreement with the theoretical calculations performed for ferromagnetic cobalt nitrides by Houari *et al.* [17], if we consider the formation of Co_4N above 5% N_2 and Co_3N at 20% N_2 in plasma forming media. The decrease in saturation magnetization was also observed in thicker films and associated with the formation of different nitride phases [8]. For the Co film, CoN0, our results give a very small coercive field (2.5 mT) that increases by a factor of three for films with nitrogen. This increase is monotonic with nitrogen

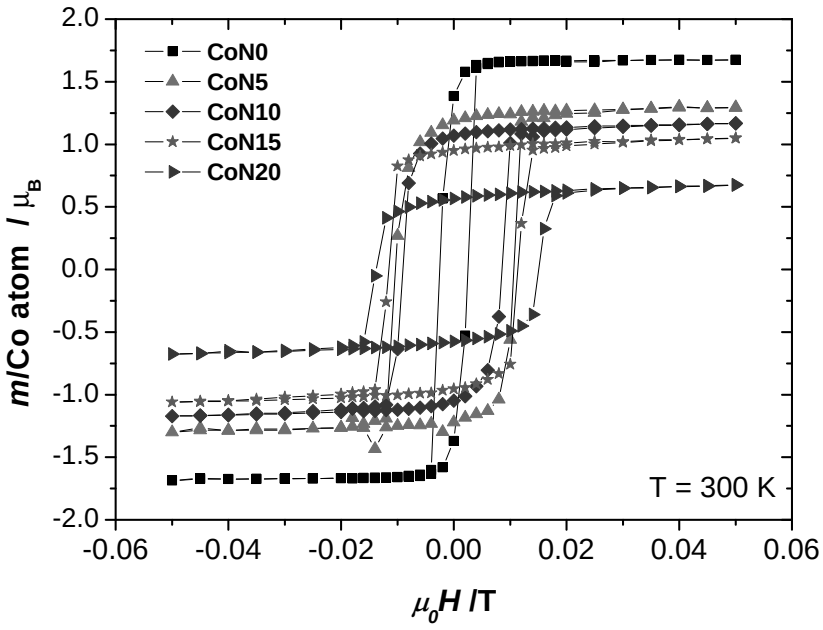

Figure 4.3: Hysteresis curves for all samples at 300 K.The normalization was carried out using the surface area and the surface atomic density determined by RBS.

content. For films CoN5-CoN15, the similarities in the XRD patterns indicate similar microstructure while an evolution of coercive field from 9 mT to 11.5 mT is observed. For CoN20, the coercivity increases further to 15 mT. The variation of the coercive field for the whole range of investigated compositions is explained by compositional and / or microstructural changes due to nitrogen addition. The obtained coercive field values are higher than the ones reported for thicker Co-N films [62].

Comparison with previous results allows the assumption that the atomic density and magnetic properties of the films are strongly dependent on the preparation conditions and thickness.

4.3.2 Co-N thin films deposited on crystalline substrates

[1]

The average roughness of the films was determined to be respectively below

[1]This sub-section is a part of [59].

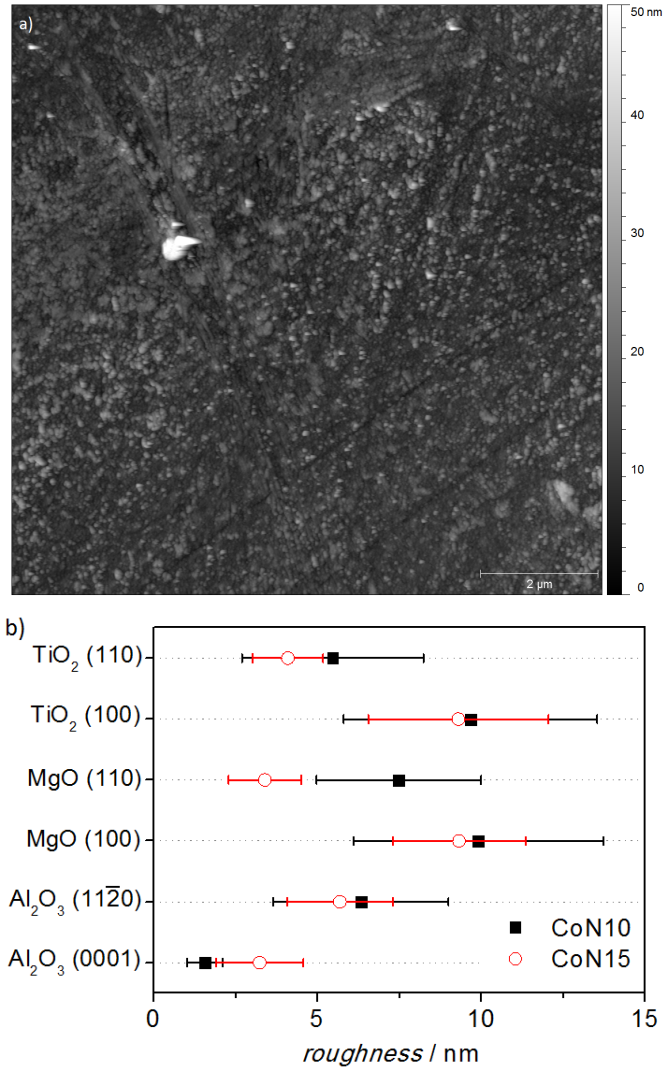

Figure 4.4: AFM topographic image of TiO_2 (100)/CoN15 film.

10 nm in all cases. In Fig. 4.4 a typical topographic image of the films is presented along with the average roughness values.

In order to confirm the incorporation of nitrogen in the films during deposition, RBS studies were conducted for all samples. In Fig. 4.5, the spectrum for sample Al_2O_3 $(11\bar{2}0)$/CoN10 illustrates the results obtained for an incident beam uncorrelated with crystal axes (random spectrum). In this figure, the full arrows mark the higher energy for $^4He^+$ backscattered by the different elements in the sample and the dashed arrow the energy expected for the same elements if considered at the surface of the samples. Since all substrates are oxides, a strong contribution of oxygen appears in all RBS spectra, starting around 0.66 MeV. This contribution appears deviated to lower energies when compared to the value for oxygen at the surface, indicating that the oxygen is in depth as expected since it is one of the major elements in the substrate. It also overlaps the profile corresponding to the nitrogen in the film preventing resolving the nitrogen profile. Nevertheless, the presence of nitrogen can be inferred by the modifications induced in the Co profile. In Fig. 4.5, the comparison between the simulations performed with and without nitrogen in the film, respectively full and dot-dash lines, shows that the contribution of nitrogen is clearly required to explain the experimental results. In the case of CoN10 deposited onto both MgO substrates, a small peak at nearby higher energies than the oxygen contribution of the substrate indicates a significant fraction of oxygen in the film. Since for most of the samples the Co profile shape decreases in the near surface region, that can also be explained by the partial oxidation of the films, the existence of an oxidized layer with the same Co/N ratio as the in depth region was allowed in the RBS simulations. Results indicate that this oxidized region does not exceed 20 nm depth for all samples with exception of MgO/CoN10.

The atomic concentrations of nitrogen were determined for all films from the simulations of RBS spectra, yielding values between 6% and 16% at depths greater than 20 nm. The results obtained for the films composition presented in Table 4.2 indicate an average Co/N ratio of 13 and 7 respectively for CoN10 and CoN15, confirming more nitrogen incorporation in CoN15 films.

The Co surface atomic density was determined directly from the peak area in the experimental RBS random spectra. Considering these values and the

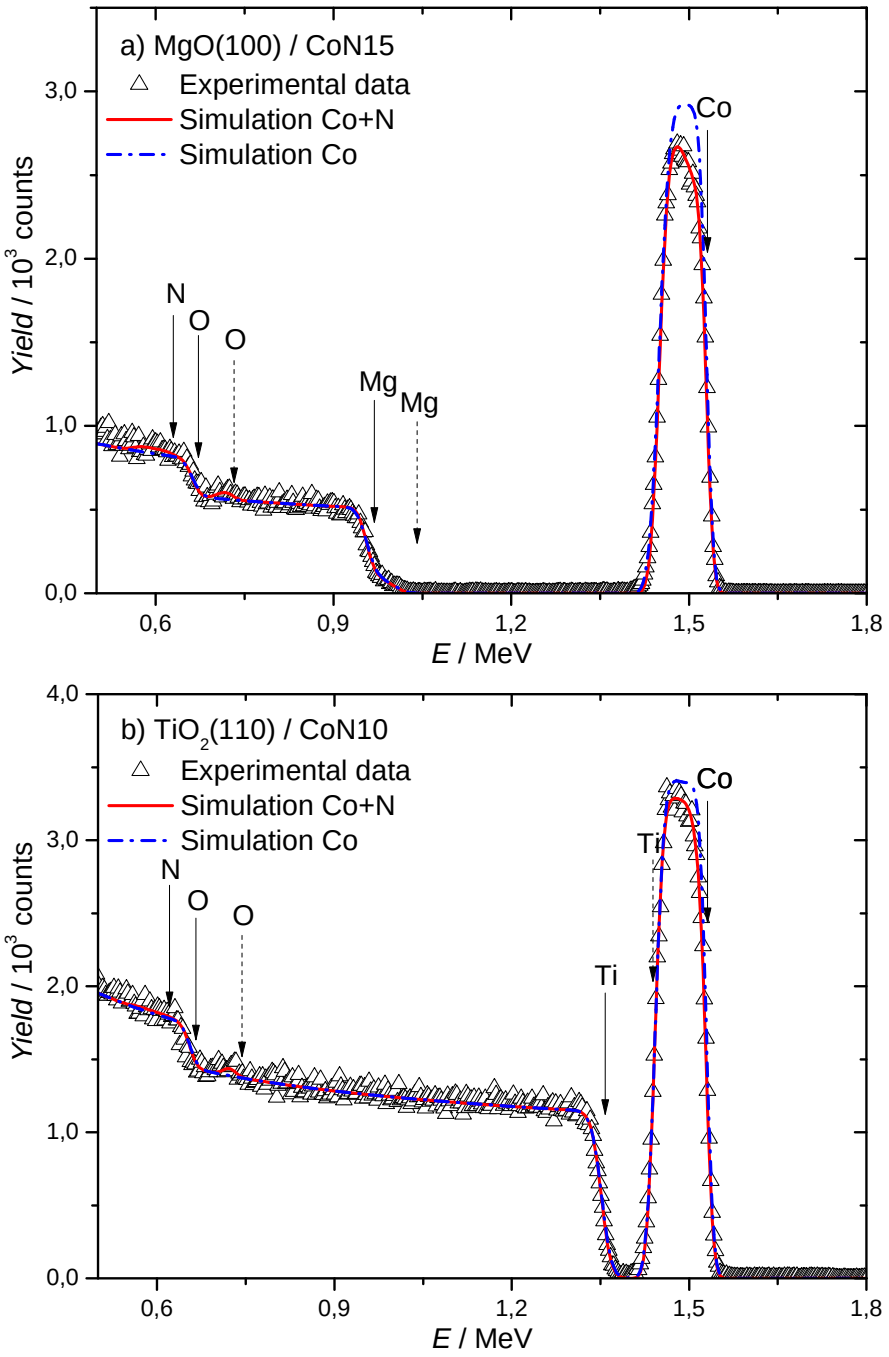

Figure 4.5: RBS spectra for samples (a) MgO (100)/CoN15 and (b) TiO2 (110)/CoN10. The blue dash-dot line and red full line are the simulated spectra, respectively with and without nitrogen. The full arrows mark the highest energy associated with particles scattered by the elements in the substrate and in the film, and the dashed arrows indicate the energy expected for the same scattering ions at the surface.

Table 4.2: Composition of the films under study, determined by simulation of the RBS spectra.

PP(N_2) = 10% *Substrate*	*f(Co)*	*f(N)*	*Ratio Co/N*
$Al_2O_3(0001)$	92(1)	8(1)	12
$Al_2O_3(11\bar{2}0)$	92(1)	8(1)	12
MgO(100)	73(1)	27 (N+O)	
MgO(110)	84(1)	16 (N+O)	
TiO_2 (100)	95(1)	6(1)	16
TiO_2 (110)	93(1)	7(1)	13
PP(N_2) = 15% *Substrate*	*f(Co)*	*f(N)*	*Ratio Co/N*
$Al_2O_3(0001)$	89(1)	11(1)	8.1
$Al_2O_3(11\bar{2}0)$	84(1)	16(1)	5.3
MgO(100)	85(1)	15(1)	5.7
MgO(110)	84(1)	16(1)	5.3
TiO_2 (100)	89(1)	11(1)	8.1
TiO_2 (110)	92(1)	8(1)	12

average thickness of the films, determined to be $54\,\text{nm} \pm 2\,\text{nm}$ for CoN10 and $48\,\text{nm} \pm 2\,\text{nm}$ for CoN15, the cobalt atomic density was calculated. The results are presented in Table 4.3, showing that the average density, 7.4×10^{22} at/cm^3, is the same for both groups of samples. The obtained value is smaller than the bulk Co density (9.11×10^{22} at/cm^3) or the theoretical density for stoichiometric Co_4N (8.31×10^{22} at/cm^3) (Fig. 4.6), indicating that the deposition method favours a low density aggregation of the film grains.

X-ray absorption near edge spectra (XANES) were collected on MgO(110)/CoN10 and TiO_2 (110)/CoN10. In Fig. 4.7 normalized Co-K edge XANES measured on MgO(110)/CoN10 are presented together with experimental spectra of reference compounds: bulk cobalt metal foil with hcp structure (Co_{hcp}) and Co sample with fcc structure (Co_{fcc}) [63]. The experimental spectra measured for the two films are similar to the spectrum of Co_{fcc} demonstrating that Co is mainly in cubic phase. In the same figure the experimental XANES spectra of reference oxides CoO (Co^{2+}) and Co_3O_4 (Co^{2+}, Co^{3+}) are also plotted to show that the existence of Co in higher valence state implies a considerable reduction of the edge shoulder around 7710 eV. Since this is not observed in the experimental data, the

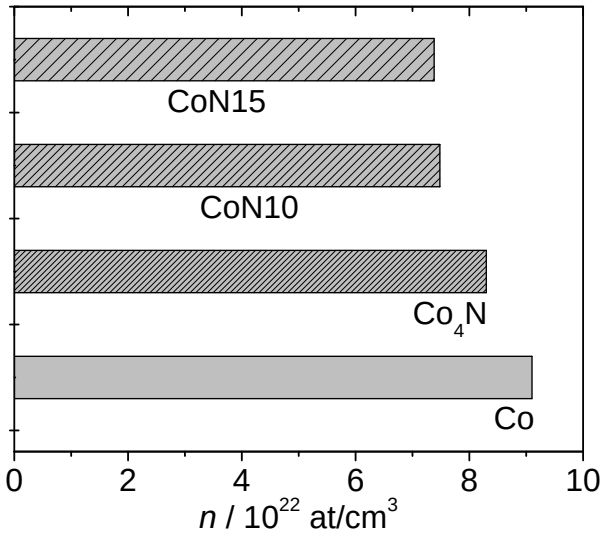

Figure 4.6: Average Co atomic density of the films and the theoretical values for Co and Co_4N compounds.

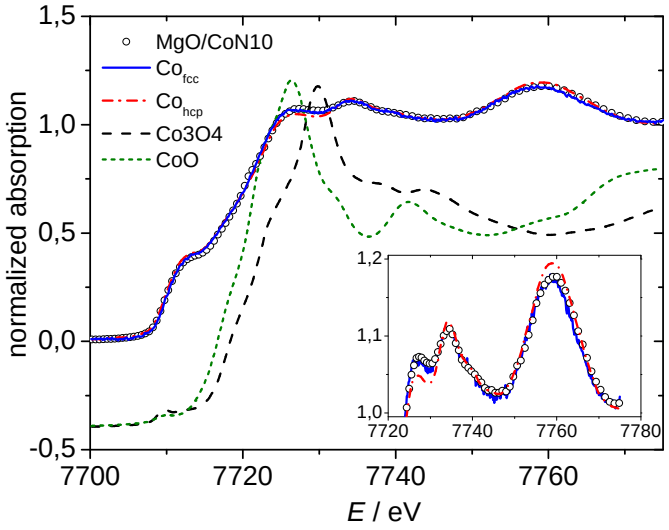

Figure 4.7: Normalized Co-K edge X-ray absorption spectra in the XANES region for MgO/CoN10 (open circles)and reference spectra of Cobalt, foil with hcp structure (Co_{hcp}) and Co fcc structure (Co_{fcc}) [63]. The Co K edge absorption spectra of reference Co oxides (CoO and Co_3O_4) are also plotted, vertically shifted for sake of comparison. In the inset the XANES features just above the edge are shown to highlight the difference (similarity) between MgO(110)/CoN10 spectra and Co_{hcp} (Co_{fcc}) spectra.

Table 4.3: Cobalt atomic density obtained from RBS results.

PP(N_2) = 10%		
Substrate	*Co surface atomic density (10^{17} at/cm^2)*	*Co atomic density (10^{22} at/cm^3)*
$Al_2O_3(0001)$	4.1(2)	7.6(4)
$Al_2O_3(11\bar{2}0)$	4.2(2)	7.8(4)
MgO(100)	3.9(2)	7.2(4)
MgO(110)	3.7(2)	6.9(4)
$TiO_2(100)$	4.0(2)	7.4(4)
$TiO_2(110)$	4.0(2)	7.4(4)
PP(N_2) = 15%		
Substrate	*Co surface atomic density (10^{17} at/cm^2)*	*Co atomic density (10^{22} at/cm^3)*
$Al_2O_3(0001)$	3.4(2)	7.1(4)
$Al_2O_3(11\bar{2}0)$	3.6(2)	7.5(4)
MgO(100)	3.5(2)	7.3(4)
MgO(110)	3.4(2)	7.1(4)
$TiO_2(100)$	3.5(2)	7.3(4)
$TiO_2(110)$	3.8(2)	7.9(4)

fraction of Co in these high valence states is well below 5 at% .

Deeper details about the nature of the Co structure are obtained looking at the EXAFS region of the spectra. In Fig. 4.8 the k^3 weighted Fourier transform (FT) of the EXAFS data and the best fit curves of the films results are shown along with those of Co-reference foil. All the data measured on Co-N films looks similar and no differences can be appreciated as a function of the substrate or the orientation. Moreover the data collected on the films looks very similar to the spectrum measured on a reference foil of metal Co. We must note that the difference between hcp and fcc structure is definitely weak at the local scale and cannot be easily appreciated in the EXAFS region. The FT of the films spectra depict sample structure from the next neighbour shells signal well above 5 Å, this suggests a bulk like structure around Co atoms, relatively ordered.

The quantitative analysis of the EXAFS data has been performed in the k-range 3 Å^{-1}−14 Å^{-1} using the FITEXA code [64] following a multi-shell approach: the first 4 coordination shells of the Co fcc structure are used in the fitting including multiple scattering contribution for the Co-Co-Co aligned configurations along the

Table 4.4: Results of EXAFS data analysis on Co film and reference Co-foil. The standard uncertainty on the refined parameters is indicated in parenthesis, (*) specify a fixed or constrained parameter: the coordination numbers were fixed to the fcc crystallographic values, the R_1 coordination distance was refined while the next neighbour distances were constrained to the fcc structure: R_2=$\sqrt{2}$ R_1, R_3=$\sqrt{3}R_1$ and R_4=2 R_1. R_2 corresponds to the edge of the fcc unit cell (lattice parameter). The coordination distances (R_1, R_2, R_3, R_4) are expressed in Å and σ^2 in units of 10^{-3} Å^2.

Shell	1		2		3		4	
	N_1=12*		N_2=6*		N_3=24*		N_4=12*	
Sample	R_1	σ^2	R_2	σ^2	R_3	σ^2	R_4	σ^2
MgO_{in}	2.495(6)	3.1(2)	3.528*	5.4(3)	4.321	5.4(3)	4.989	5.1(4)
MgO_{out}	2.495(6)	3.0(2)	3.529*	6.2(4)	4.322	5.2(3)	4.991	5.0(4)
TiO_{2in}	2.497(6)	2.8(2)	3.531*	5.0(3)	4.325	5.0(3)	4.994	4.8(5)
TiO_{2out}	2.496(6)	3.0(2)	3.529*	6.2(3)	4.322	4.7(3)	4.991	4.6(4)
Co-foil	2.489(6)	2.2(2)	3.520*	4.1(4)	4.311	4.0(3)	4.977	4.5(5)

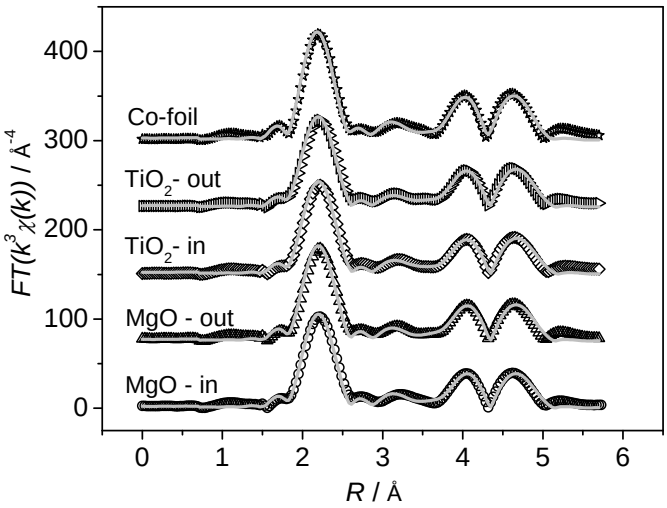

Figure 4.8: Moduli of the Fourier transform of k^3 weighted experimental EXAFS data (dots) and best fit (full lines) of the investigated samples, vertically shifted for clarity. The data and best fit for Co_{hcp} metal foil data (Co-foil) are reported as the topmost curve.

cube diagonal (see [65] for more details). Coordination numbers and coordination distances were constrained to the Co fcc structure in order to reduce the number of free parameters, a Gaussian distribution model is used to take into account for structural disorder (mean square relative displacement parameters σ^2). The best fits are shown in Fig. 4.8 and the structural parameters are summarized in table 4.4 . The structural parameters obtained from the fit are in agreement with weakly expanded Co-fcc structure with respect to the reference Co foil ($\Delta a/a$= 0.3%). The disorder parameters (σ^2) point out a weakly larger disorder in the films with respect to the metal foil. No differences can be observed comparing the data collected with X-ray polarization along the film plane (in) and perpendicular to it (out), meaning that the structural anisotropies, if existing, are below the detectability limit of our measurements.

The attempt to refine the data using a Co-N shell does not improve the data fitting, and no evidence for Co-N correlations can be found in the XANES region. EXAFS and XANES results indicate that the Co-N film structure is very similar to fcc-Co with a small lattice expansion, indicating a highly nitrogen deficient $Co_{4+x}N$ composition or that samples are inhomogeneous at the microscopic scale with relatively large cubic Co-rich regions co-existing with N-richer regions. The fraction of cobalt bond to nitrogen is not detected and must be below 5%-6%.

The XRD patterns for the films under investigation are shown in Fig. 4.9. Besides the substrate diffraction peak, two main peaks can be identified in most samples, respectively at 44.3° and 51.5° for CoN10 and at 44.6° and 51.6° for CoN15, indicating that the films are crystalline. These positions are associated with the (111) and (200) planes respectively, of the cubic phases of Co or $Co_{4+x}N$. The XRD and XAFS results cannot distinguish fcc Co and nitrogen deficient cubic $Co_{4+x}N$, since the corresponding structures have very small differences, with the lattice parameter varying by less than 0.5% for films prepared in the same way [58]. Nevertheless, the confirmation of nitrogen incorporation by RBS analysis, and the fact that no other nitride phases are observed in the XRD pattern, indicate that our films are primarily composed of $Co_{4+x}N$ or a mixture of $Co_{4+x}N$ and fcc Co. The small expansion determined by XAFS, indicates integration of N in the Co cubic cell. The lattice parameter a_{Co_4N} has been theoretically predicted to be 3.73 Å[15; 26] but reported experimental values are much lower, 3.587 Å[7]

and 3.57 Å[26] respectively for films and powders, only 1.2% and 0.7% larger than the lattice parameter of fcc Co ($a_{Co_{fcc}}$ = 3.545 Å). These experimental weaker expansions are explained by the nitrogen deficient stoichiometry of the prepared compounds. The influence of the substrate can also affect the expansion. For very thin Co-N films (9-14 nm thickness) grown onto $SrTiO_3$ the lattice parameter obtained was 3.524 Å, explained by the epitaxial interaction with the substrate[66], and corresponding to a negative expansion relative to fcc cobalt, $\Delta a/a$ = -0.6%. In our case there is a similar expansion of the lattice for the 50 nm films deposited onto two very different substrates corroborating the integration of nitrogen and indicating that the substrate is not the major factor determining the lattice parameter.

In the case of MgO(110)/CoN10, MgO(100)/CoN15 and MgO(110)/ CoN15 the intensities of the diffraction peaks are very small, but in the other systems they are well defined indicating good crystallinity. The two peaks relative intensity is similar for CoN10 and CoN15 films deposited onto the same substrate but changes for the different substrates, indicating that the films growth was epitaxial with the orientation determined by the substrate. For substrate Al_2O_3(0001) the Co-N films have orientation [111], while for $Al_2O_3(11\bar{2}0)$ or MgO(100) the film orientation is [100]. To explain these results, the lattice structures of the films and substrates were compared. Fig. 4.10 depicts three examples of the match between the plane of the substrate parallel to the surface and the best matching plane of the cubic structure of the film with the cobalt position adjusted to the one of the oxide cation in the substrate.

The mismatches between the films and the substrates were quantified considering the ratio $f = (d - d_0)/d$ where d is the nearest neighbour distance between cobalt ions in the film plane and d_0 is the distance between the cations of the substrate that better adjust with the cobalt ions. The sign of the ratio f, positive or negative, is associated respectively with compression or expansion of the films lattice to accommodate on the substrate. The f-values corresponding to the smallest mismatch found are presented in Table 4.5. These results are in agreement with the XRD results, as the substrates on which the films grow with higher crystallinity are the ones where the average f-factors are either small (<0.1) or have the same sign in the two perpendicular directions. This indicates that a global expansion

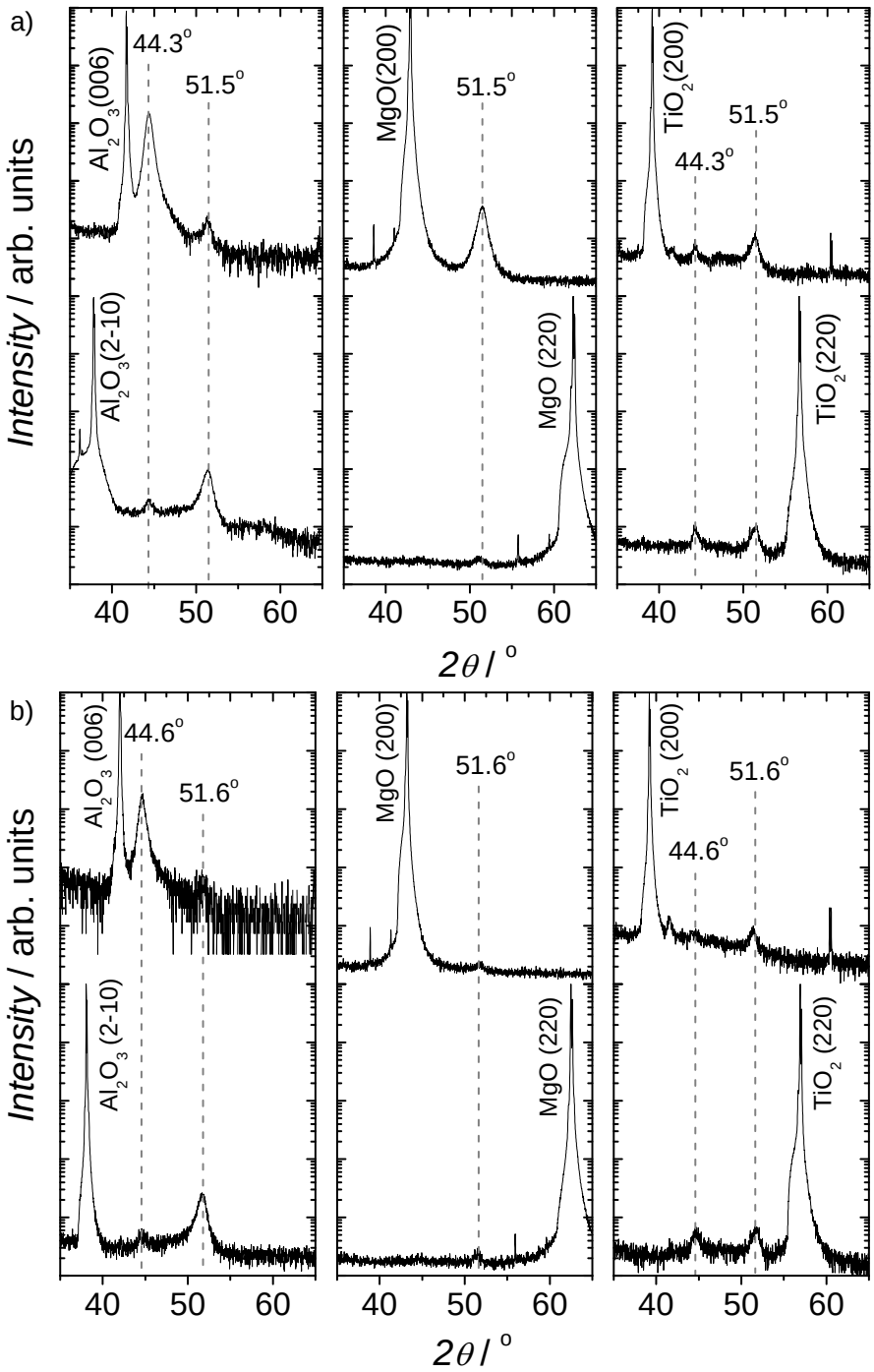

Figure 4.9: $\theta-2\theta$ XRD patterns obtained for films deposited with a) PP(N_2)=10% and b) PP(N_2)=15%.

Table 4.5: Lattice mismatch calculated for the arrangements with the best compatibility between film and substrates.

Substrate	*film orientation*	*relative directions*	*f-factor*
$Al_2O_3(0001)$	[100]	$< 100 >_s // < 051 >_f$	-0.042
		$< 120 >_s // < 01\bar{5} >_f$	0.098
	[111]	$< 100 >_s // < 1\bar{1}0 >_f$	0.061
		$< 120 >_s // < 11\bar{2} >_f$	0.061
$Al_2O_3(11\bar{2}0)$	[100]	$< \bar{1}10 >_s // < 011 >_f$	-0.083
		$< 001 >_s // < 01\bar{1} >_f$	-0.075
	[111]	$< 001 >_s // < 1\bar{1}0 >_f$	-0.075
		$< 1\bar{1}0 >_s // < 11\bar{2} >_f$	0.062
MgO(100)	[100]	$< 010 >_s // < 010 >_f$	-0.170
		$< 001 >_s // < 001 >_f$	-0.170
	[111]	$< 010 >_s // < 110 >_f$	0.172
		$< 001 >_s // < 11\bar{2} >_f$	0.043
MgO(110)	[100]	$< 100 >_s // < 011 >_f$	0.172
		$< 110 >_s // < 01\bar{1} >_f$	-0.169
	[111]	$< 1\bar{1}0 >_s // < 1\bar{1}0 >_f$	-0.169
		$< 001 >_s // < 11\bar{2} >_f$	0.043
$TIO_2(100)$	[100]	$< 010 >_s // < 011 >_f$	0.095
		$< 001 >_s // < 01\bar{1} >_f$	-0.168
	[111]	$< 010 >_s // < \bar{1}2\bar{1} >_f$	-0.046
		$< 001 >_s // < 101 >_f$	-0.168
$TIO_2(110)$	[100]	$< \bar{1}10 >_s // < 010 >_f$	0.093
		$< 001 >_s // < 001 >_f$	0.175
	[111]	$< \bar{1}10 >_s // < 1\bar{2}1 >_f$	-0.481
		$< 001 >_s // < 10\bar{1} >_f$	-0.165

or contraction of the film structure is preferred over an asymmetric deformation. For substrates MgO(110) and TiO_2(100) and TiO_2(110) the mismatch factors have different signs or very different values in the matched directions and no specific orientation can be identified since the films exhibit very small XRD diffraction peaks or peaks for different planes with similar intensity.

The magnetic moment of the samples was studied as a function of temperature and magnetic field in two perpendicular in-plane orientations. The substrates magnetization was also measured and the values -4.16×10^{-9} m^3kg^{-1}, -4.08×10^{-9} m^3kg^{-1} and 9.25×10^{-10} m^3kg^{-1} were obtained respectively for the mag-

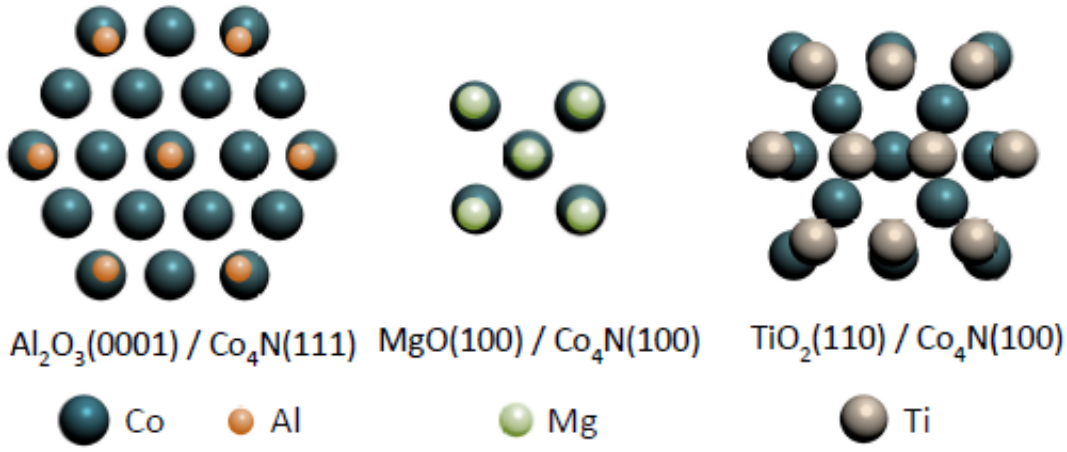

Figure 4.10: Schematic representation of the matching between a Co (fcc) film and substrate for the cases of Al_2O_3 (0001), MgO (100) and TiO_2 (110).

netic susceptibility of Al_2O_3 , MgO and TiO_2 rutile. Since the volume of the films is below 0.001% of the substrate volume, the contribution of the substrate to the magnetic moment was determined using the experimental susceptibility and the volume of the samples. In all results presented this contribution was subtracted to isolate the film magnetic moment. All the results are normalized by the surface area since all the samples have similar thickness ($\simeq$50 nm). At 300 K the magnetization hysteresis curves are similar for all samples indicating that both Co10N and Co15N films are ferromagnetic independently of the substrate. The results are illustrated in Fig. 4.11 for CoN10/Al_2O_3 (0001).

For all films of the same group, the saturated magnetic moment is comparable, and decreases from CoN10 to CoN15. Nevertheless the values of the magnetic moment per cobalt ion, calculated using the experimental cobalt densities, have similar values for both groups indicating that the different magnetization due to deposition in different partial pressure of nitrogen is associated with differences in cobalt concentration. The saturation magnetic moments obtained for the films under investigation range from 1.53 μ_B to 1.88 μ_B per Co atom. These values are higher than the ones obtained for films deposited under the same conditions on glass substrates (1.2 μ_B) [58]. This is explained by the crystallinity of the films grown on crystalline substrates.

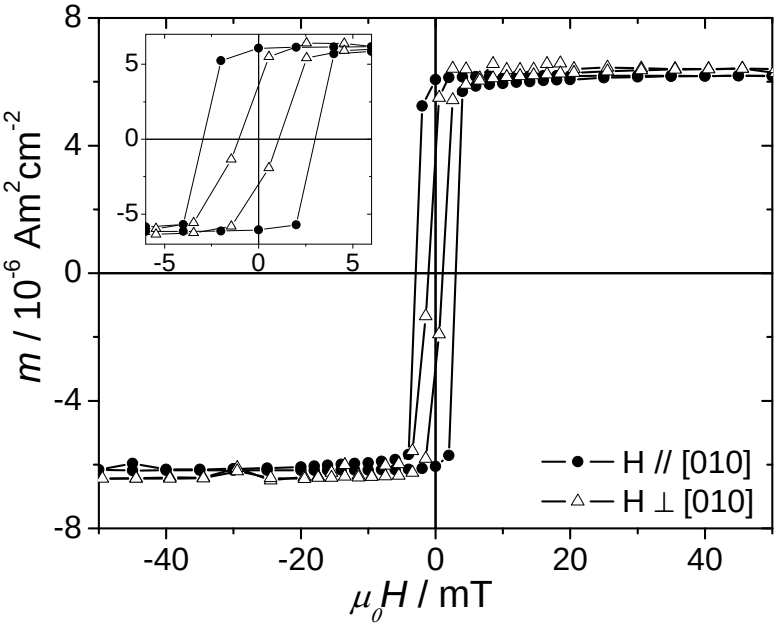

Figure 4.11: Magnetic moment as a function of applied magnetic field for $Al_2O_3(0001)$/CoN10 at 300 K; inset: low field region.

Table 4.6: Summary of magnetic properties obtained from in-plane magnetic measurements of samples deposited with PP(N_2)=10%.

Substrate	Geometry	H_c (mT)	m_s $(10^{-6}Am^2cm^{-2})$	m_s $(\mu_B/Co\,atom)$
$Al_2O_3(0001)$	H$\parallel <010>$	3.0	6.3(5)	1.6(1)
	H$\perp <010>$	1.0		
$Al_2O_3(11\bar{2}0)$	H$\parallel <001>$	5.0	6.0(3)	1.5(1)
	H$\perp <001>$	5.0		
MgO(100)	H$\parallel <001>$	12.0	5.7(1)	1.5(1)
	H$\perp <001>$	12.0		
MgO(110)	H$\parallel <001>$	12.0	6.3(2)	1.8(1)
	H$\perp <001>$	12.0		
$TiO_2(100)$	H$\parallel <001>$	2.0	6.7(3)	1.8(1)
	H$\perp <001>$	1.0		
$TiO_2(110)$	H$\parallel <001>$	3.0	6.7(5)	1.8(2)
	H$\perp <001>$	3.0		

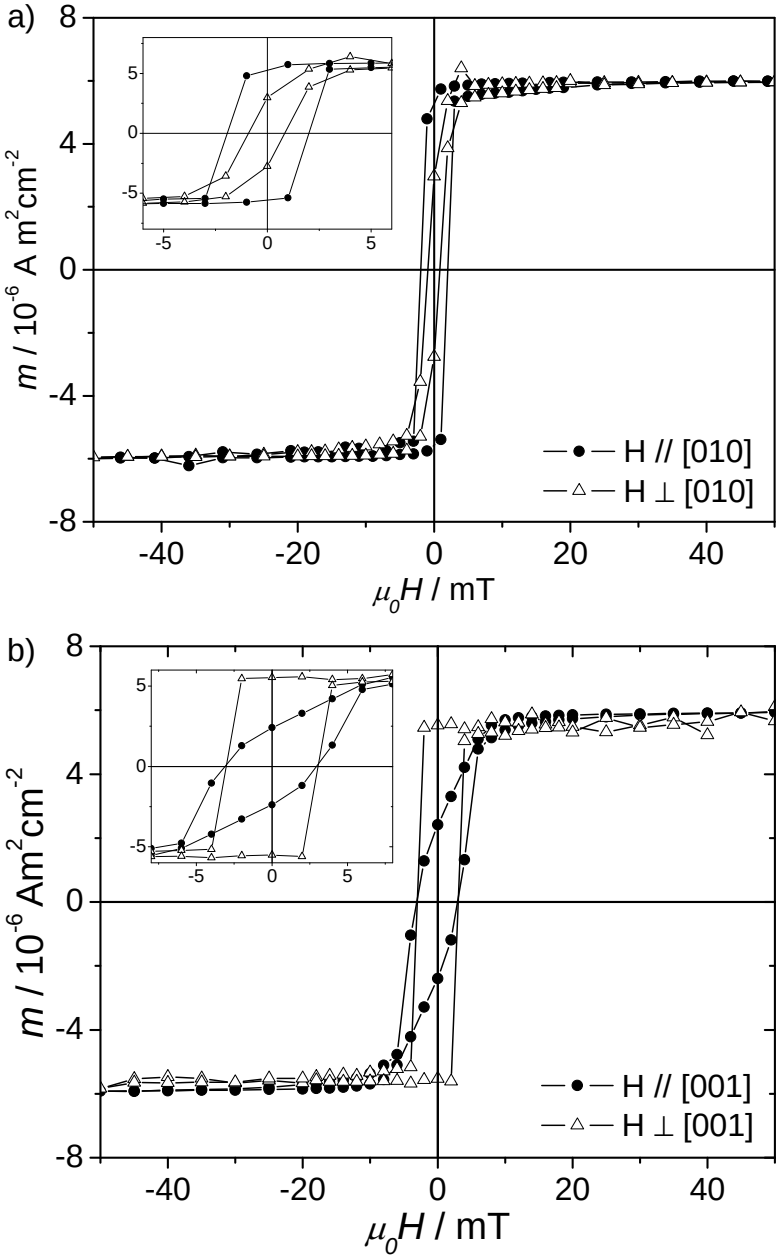

Figure 4.12: Magnetic moment as a function of applied magnetic field for CoN15 in substrates (a) $Al_2O_3(0001)$ and (b) $TiO_2(100)$.

The similar magnetization of the films along with the similar lattice parameter indicate that the composition of the cubic nitride is similar in both groups, the excess nitrogen segregating in nitrogen rich regions. In the case of CoN15/ TiO_2(100) films the XRD pattern exhibits a peak at 41.5° that can be associated with the appearance of a small fraction of Co_3N phase, that also explains the reduction in the intensity of the diffraction peaks associated with the cubic structure. The stoichiometry of the cubic nitride can then be obtained from the films CoN10, considering the one with lower nitrogen content, where less nitrogen segregation or none is expected. This is $Co_{16}N$, that agrees with the reported stoichiometry of the cubic nitride $Co_{4+x}N$ with higher nitrogen content produced by nitriding cobalt particles [26].

The films exhibit no significant anisotropy and relatively low coercive field for in-plane measurements, typically below 5.0 mT, except for the case of MgO(100) and $Al_2O_3(11\bar{2}0)$ substrates. Variations in the coercive field for different in-plane directions were only observed for the films deposited on substrates with non-equivalent directions in the surface Al_2O_3(0001)/CoN10 and Al_2O_3(0001)/CoN15. Since the films have cubic structure and for the (100) orientation should display equivalent perpendicular directions, the different coercive fields are attributed to the influence of the substrate that induce dependent expansion or contraction of the film during growth. In the case of the film TiO_2 (100)/CoN15 the coercive field is the same for both measured directions of applied field, but the shape of the hysteresis curves is different (Fig. 4.12), indicating different magnetization rotation mechanisms attributed to the anisotropic stress induced by the substrate. The coercive field observed for film MgO(100)/CoN10 (12.0 mT) is well above the values obtained for the other samples ($\leq$5.0 mT). This difference can be associated with the presence of oxygen in the film.

Magnetic measurements were also performed with magnetic field perpendicular to the film plane. The hysteresis curve obtained for MgO/CoN10 deposited at PP(N_2)=10% in Fig. 4.13 illustrates the type of results obtained. For all samples the coercive field is higher than 20 mT at room temperature, but the remanent magnetization values are lower compared to the magnetization measured in the plane of the film. The difference in coercivity can be explained by the fact that rotation occurs preferentially in the film plane for magnetic field parallel to the sur-

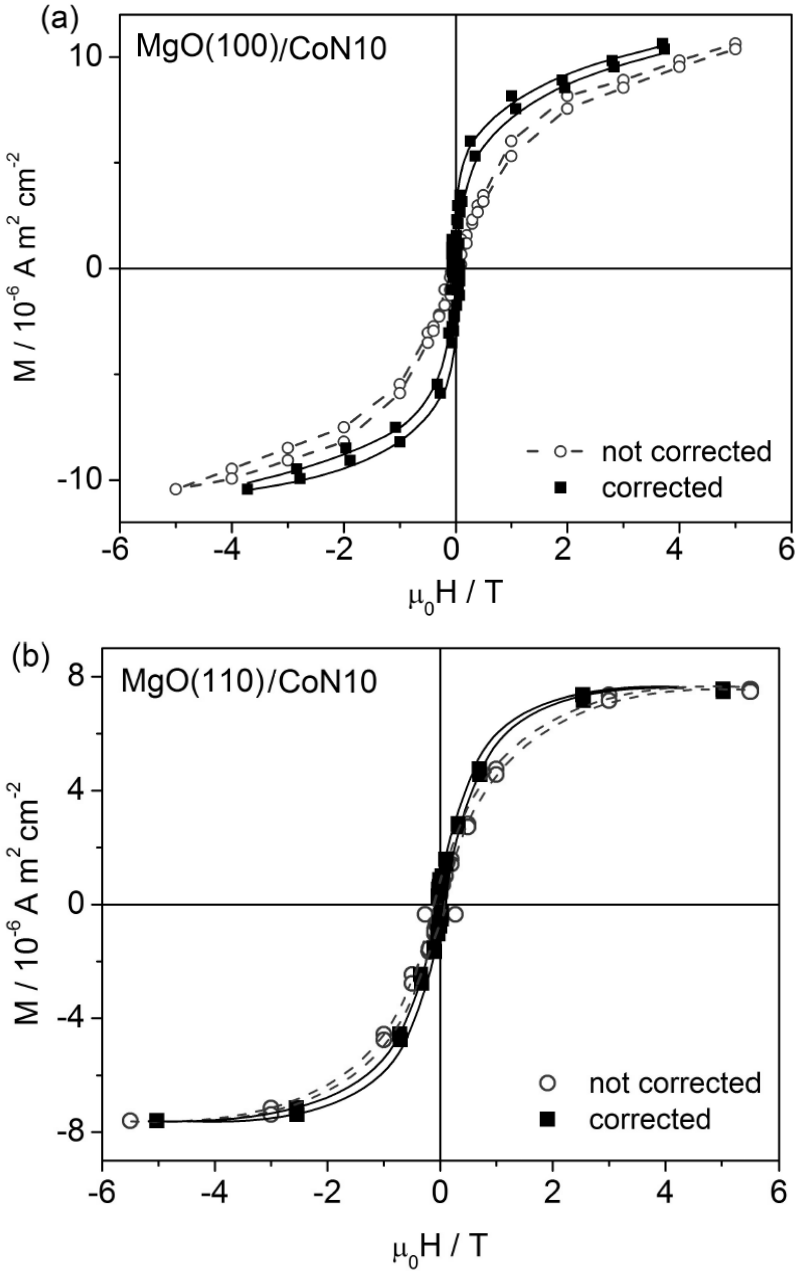

Figure 4.13: Magnetic moment as a function of magnetic field applied perpendicularly to the films surface for (a) MgO(100)/CoN10 and (b) MgO(110)/CoN10. The curves are shown before (open symbols) and after correction for the demagnetizing field (solid symbols). The demagnetizing factors are 0.78 for MgO(100) and 0.4 for MgO(110).

face, while for perpendicular magnetic field it comes out of the plane, the roughness of the films inducing a non-zero magnetization at low field. The demagnetizing factor is calculated from the susceptibility at low fields and does not correct completely the whole curve, explaining why saturation magnetization is only attained at higher fields. Results show that for the majority of the film perpendicular magnetization is not favoured.

All samples exhibit metallic conductivity in the temperature range between 5 K and 270 K, illustrated in Fig. 4.14 a) for sample MgO(100) / CoN10 and Al_2O_3(0001) / CoN10. Since for all samples, the spacing between contacts is $s \simeq 1$ mm, much higher than the thickness t of the films ($t/s \ll 0.5$), the electrical resistivity can be determined using $\rho = R\pi t/\ln 2$, with R being the experimental electrical resistance [67]. The determined values for the resistivity close to room temperature and the temperature coefficients considering linear temperature dependence above 100 K, determined by phonon scattering, are summarized in Table 4.8 for the four films displaying better crystallinity.

The values of the room temperature resistivity are of the same magnitude but larger than the ones obtained for polycrystalline Co films [68].

Below 60 K the electrical resistivity dependence with temperature can be well fitted with a T^4 dependence explained by multiple magnon diffusion or considering the added contribution of magnons and phonons with $aT^2 + bT^5$ dependence (see Fig. 4.14b).

Magnetoresistance (MR) was also measured between 10 K and 270 K using two different configurations: magnetic field in plane parallel to the electric current and magnetic field out of plane perpendicular to the films surface and to the current. Magnetoresistive effects were observed for all films in both configurations that do not depend on the temperature. Typical results are shown in Fig. 4.15 for film TiO_2(100)/CoN10. In the out of plane configuration the maximum values of MR are 1.0(2)% for all measured samples, while for the in plane configuration, the results are in the range of 0.1%. Both the magnitude and the temperature invariance of the MR are consistent with the magnetoresistance displayed by metals.

For all measured samples, an asymmetry is observed in the magnitude of the MR peaks for the two magnetic field polarities in the perpendicular configuration, although the location of the peaks is the same. This effect is particularly

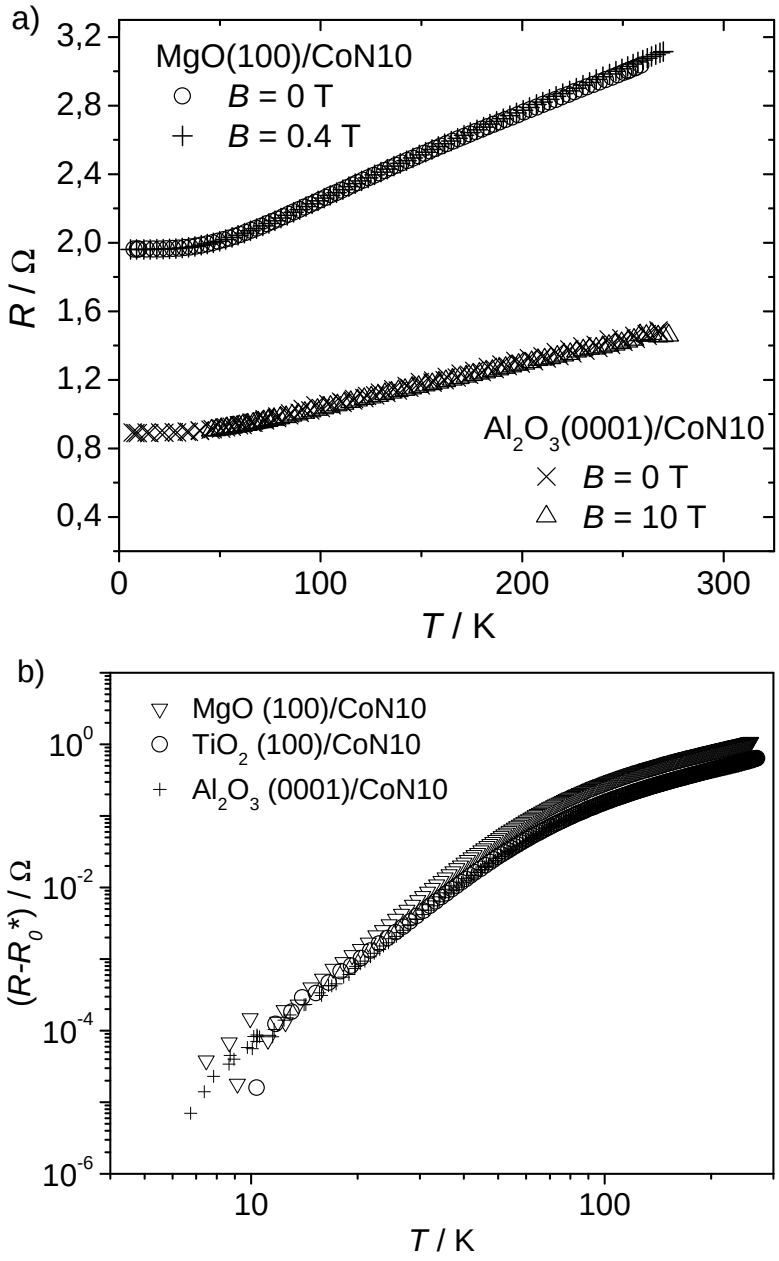

Figure 4.14: (a) Electrical resistance as a function of temperature for MgO(100)/CoN10 and Al_2O_3(0001)/CoN10 with and without applied magnetic field perpendicular to the film surface; (b) Logarithmic representation of three films resistance evidencing the low temperature behaviour (R_0^* is the value measured at the lowest temperature and B = 0 T).

Table 4.7: Summary of magnetic properties obtained from in-plane magnetic measurements of samples deposited with PP(N_2)=15%.

Substrate	Geometry	H_c (mT)	m_s $(10^{-6}Am^2cm^{-2})$	m_s $(\mu_B/Co\,atom)$
$Al_2O_3(0001)$	H$\parallel <010>$	2.0	5.9(2)	1.8(1)
	H$\perp <010>$	1.0		
$Al_2O_3(11\bar{2}0)$	H$\parallel <001>$	5.0	5.7(1)	1.7(1)
	H$\perp <001>$	6.5		
MgO(100)	H$\parallel <001>$	3.5	5.3(1)	1.6(1)
	H$\perp <001>$	3.5		
MgO(110)	H$\parallel <001>$	3.5	5.9(4)	1.9(2)
	H$\perp <001>$	3.5		
$TiO_2(100)$	H$\parallel <001>$	3.0	5.8(2)	1.8(1)
	H$\perp <001>$	3.0		
$TiO_2(110)$	H$\parallel <001>$	1.0	5.8(1)	1.6(1)
	H$\perp <001>$	1.0		

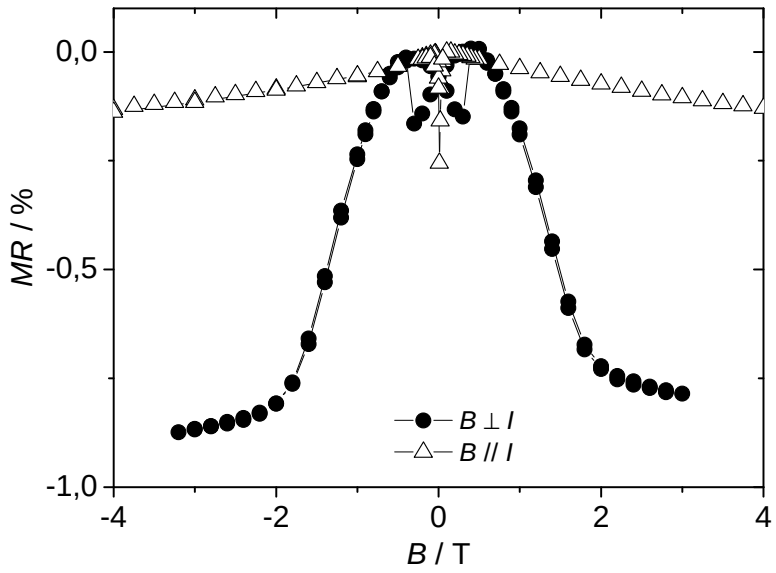

Figure 4.15: Magnetoresistance results for TiO_2 (100)/CoN10 obtained with magnetic field applied in plane parallel to the current and out of plane perpendicularly to the film surface, at 270 K.

Table 4.8: Electrical resistivity and temperature coefficients ($\alpha = \Delta\rho/\Delta$T) at room temperature for CoN10 films.

Substrate	$\rho/\mu\Omega$ cm (270 K)	$\alpha/10^{-3}K^{-1}$
$Al_2O_3(0001)$	53.4	2.5
$Al_2O_3(11\bar{2}0)$	41.9	3.2
MgO(100)	111	2.2
MgO(110)	50.4	3.0

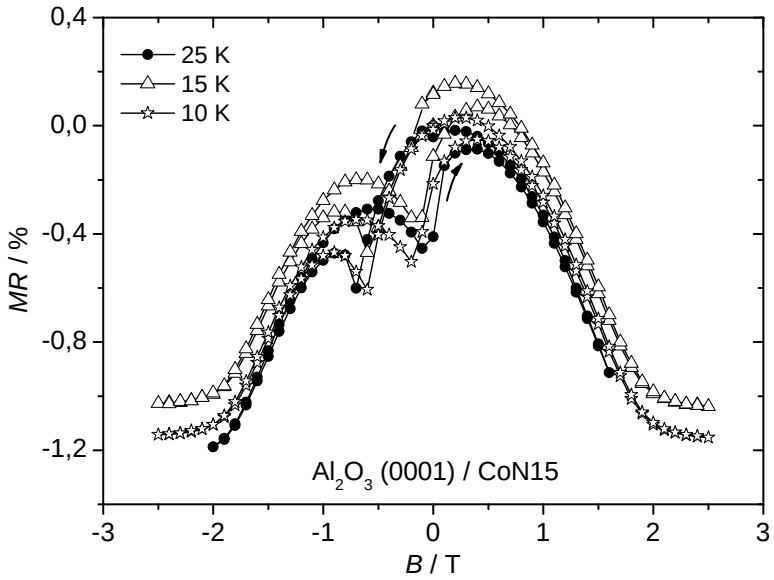

Figure 4.16: Magnetoresistance results for $Al_2O_3(0001)$/CoN10 obtained with magnetic field applied perpendicularly to the current and to the film surface, at several temperatures: an asymmetry is evident in the peaks magnitude for the two field polarities.

evident at low temperatures (Fig. 4.16), though it subsists at room temperature. Recently, it was shown that a minor variation of the thickness along the sample can induce this effect [69], but similar effects were also found at magnetization reversal of ferromagnets with an out-of plane magnetic anisotropy and explained by the movement of a domain wall located between the voltage probes, running perpendicular to both magnetization and current [70].

4.4 Main results obtained for Co-N films

Deposited on glass:

- Increase in PP(N_2) during deposition leads to an increase in nitrogen content and decrease in cobalt density;
- The phases Co, $Co_{4+x}N$ and Co_3N were observed depending on PP(N_2);

Deposited on single crystalline substrates:

- All films exhibit ferromagnetic behaviour at room temperature and display metallic electrical conductivity;
- Stoichiometry of CoN10 films deposited on crystalline substrates is close to $Co_{16}N$;
- The average moment of films is approximately 1.7 μ_B per Co atom, which is higher than what was obtained for the homologous films deposited on glass;
- Well oriented crystalline films were obtained on Al_2O_3 and MgO (100), with growth along [100] or [111] depending on the substrate's orientation;
- Stresses at the film/substrate interface induce anisotropic behaviour;
- All films exhibit negative magnetoresistance of the order of 1 % at room temperature.

Chapter 5

Fe-N thin films

5.1 Introduction

Iron nitrides were first reported by Jack [1] and since then have attracted considerable attention, due to their interesting properties and potential for applications, specially in the magnetic recording media area [2; 3].

Besides the well-known enhanced mechanical hardness of nitrides with respect to the corresponding metal, iron nitrides are more chemically stable and resistant to oxidation than Fe [2]. The ferromagnetic nitride phases are $Fe_{16}N_2$, Fe_4N, Fe_3N. It has been observed that the magnetization of iron nitrides diminishes with nitrogen content [9] with $Fe_{16}N_2$ being the phase with largest magnetization.

$Fe_{16}N_2$ is a metastable phase with a body centred tetragonal (bct) structure that can be viewed as eight (222) distorted bcc cells of α-Fe with nitrogen atoms located in regular positions (fig. 5.1). This phase has been extensively studied since the experimental determination of a giant magnetic moment of approximately 3.2 μ_B per Fe at room temperature was reported [71]. After the publication of this result many research groups endeavoured to explain and/or replicate this observation (both theoretically and experimentally) and, in many cases, without success leading to disbelief [12; 72; 73; 74]. Despite the somewhat discrepant reports, it has been established that $Fe_{16}N_2$ does in fact possess a high magnetic moment that is strongly affected by the degree of ordering of the nitrogen atoms in the lattice and by microstructural features such as surface morphology [10; 71; 75]

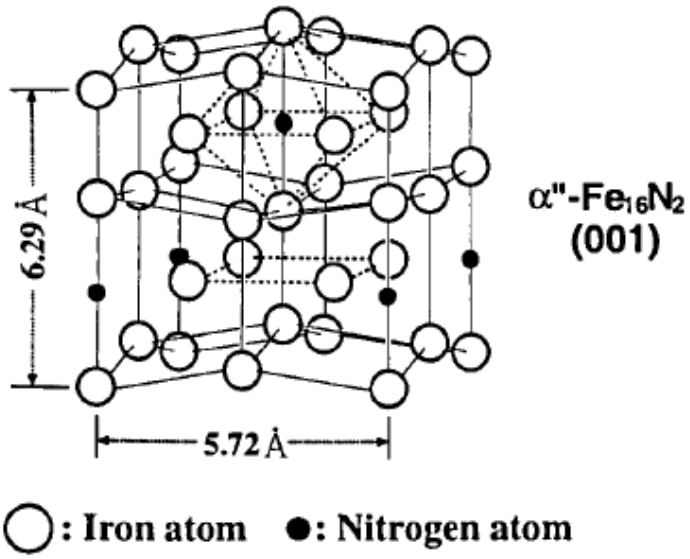

Figure 5.1: Crystal structure of $Fe_{16}N_2$. Adapted from [76].

which explains the many different observations reported. No similar phase was observed for cobalt nitrides.

The magnetic moment of Fe_4N is smaller than that of $Fe_{16}N_2$ and Fe, but it is significantly greater than iron oxide [2] and this compound is chemically more stable than Fe and easier to obtain than $Fe_{16}N_2$. Like Co_4N, it has an fcc structure of iron with a nitrogen atom at the body centre position (fig. 5.2). This structure has iron sites at different distances from nitrogen, Fe^I and Fe^{II}, respectively the corner and face centre sites, implying different local Fe moments. In fact, the most distant Fe from the N atoms (Fe^I) have larger magnetic moment than Fe^{II}[12; 13] which has been experimentally verified through neutron diffraction measurements by Frazer [14], giving magnetic moments of 2.98 μ_B and 2.01 μ_B for Fe^I and Fe^{II}, respectively.

The increase in volume per Fe caused by the introduction of N atoms in interstitial positions, leads to enhancement of the average Fe magnetic moments. However, Fe(*3d*)-N(*2p*) hybridization somewhat diminishes these enhanced moments, leading to a compromise between both effects [12].

An important feature that makes Fe_4N particularly interesting, specially for

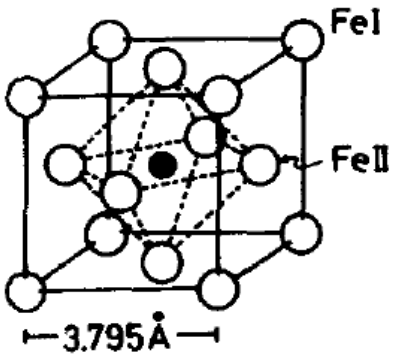

Figure 5.2: Crystal structure of Fe_4N (adapted from [13]).

spintronic applications, is its potential as a current polarizer due to its high spin polarization, predicted to be $P_{DOS}(E_F) = 1$ [18].

Fe_3N is the ferromagnetic iron nitride having higher nitrogen content. Its composition, in fact, can typically be found in a range $Fe_{3-x}N$ with $0 \leq x < 1$. It has an hexagonal structure that can be viewed as hcp Fe with N interstitials and has a magnetization significantly smaller than both $Fe_{16}N_2$ and Fe_4N.

Given the importance and potential for applications of iron nitrides, it is important to be able to control their magnetic properties, particularly the magnetic anisotropy. In previous works, different substrates have been used to produce iron nitride thin films, but none has provided a detailed study of the influence of the substrates on the in-plane magnetic anisotropy. In the following, the properties of different iron nitrides deposited by reactive sputtering will be presented, with emphasis on substrate induced anisotropy.

The characterization of films deposited on glass was carried out as a preliminary study regarding the growth conditions for iron nitride phases and the influence of temperature on oxidation.

5.2 Experimental Details

Thin films of Fe-N were deposited by reactive sputtering at two different temperatures (250 ^{o}C and room temperature (RT)) and with varying PP(N_2) on glass and crystalline Al_2O_3 (0001), Al_2O_3 (11$\bar{2}$0), MgO (100), MgO (110), TiO_2 (100) and

TiO_2 (110).

The PP(N_2) used were 5, 10 and 15 % for depositions performed at high temperature (250 ^{o}C) and 10 and 15 % for films produced at room temperature, for a constant total pressure of the Ar+N_2 mixture during deposition of 10 mTorr. The base pressure of the system was 5×10^{-5} mTorr.

The substrates were mounted on a rotating sample holder, kept at 120 mm from the magnetron, to ensure that the deposited material is uniformly distributed on the substrate. The direct current power was kept at 100 W and the deposition time was set to 30 min in order to obtain films of approximately 80 nm thickness.

The samples deposited at 250 ^{o}C will be referenced by their substrate and partial pressure of N_2 during deposition as substrate/FeN#, where # represents the PP(N_2). For samples deposited at RT the reference is substrate/FeN#RT.

X-Ray Reflectivity (XRR) was used to determine the films' thickness and morphology was accessed through AFM measurements performed in AC mode. The films' structure and composition were studied by XRD in $\theta-2\theta$ geometry and RBS performed with 2 MeV $^4He^+$ beam. To study the film's cristallinity RBS was also performed in channelling conditions with the He^+ beam aligned with the principal direction of the substrates. Mössbauer spectroscopy using ^{57}Fe conversion electrons (CEMS) was used to investigate the valence states and local surrounding of the Fe atoms in the films. The magnetic behaviour was studied using SQUID magnetometry in the temperature range from 10 K to 390 K and for magnetic fields up to 5 T.

Given the importance of magnetic multilayers for spintronic applications, samples consisting of n thin film layers (n=2,3) alternating between iron and iron nitride were deposited. The depositions were carried out at 250 ^{o}C, with a total pressure of 10 mTorr and 10 % N_2 in the reactive mixture for the production of the nitride layers.

In order to have multilayers adequate for devices, the chosen thickness for the layers was smaller than the ones used for the single layer thin films. Four groups of samples with varying layer order and thickness were prepared. The details of each group's layer stack are presented below (by the composition and the expected width of each layer given in nm).

Group A Substrate / Fe 20 / Fe-N 20

Group B Substrate / Fe 10 / Fe-N 10

Group C Substrate / Fe-N 10 / Fe 10

Group D Substrate / Fe-N 10 / Fe 10 / Fe-N 10

The samples' characterization procedure (structure, morphology, composition and magnetic properties) was carried out using the same techniques as for single layer thin films.

5.3 Results and Discussion

5.3.1 Fe-N thin films deposited on glass

The best results were obtained for PP(N_2) during deposition of 5, 10 and 15 % at 250 ^{o}C. RBS spectra show that films deposited at 250 ^{o}C have higher content of nitrogen, while films deposited at room temperature are oxidized (fig. 5.3 a)). Oxidation is detected by the increased oxygen profile in the depth corresponding to the film (between 0.65 and 0.75 MeV of the spectra). The composition of the films, determined by simulation of the RBS spectra using the RUMP code, are presented in Table 5.1 along with the determined surface atomic density of the films, both for iron atoms only and integrated for all atoms.

Table 5.1: Composition and surface density of Fe-N films deposited on glass.

	Fe (at.%)	N (at.%)	O (at.%)	Surface atomic density (10^{17} at.cm^{-2})	Fe surf. atomic density (10^{17} at.cm^{-2})
FeN10RT	69	4	27	6.30±0.32	4.35±0.34
FeN15RT	82	5	13	5.20±0.26	4.26±0.32
FeN5	>98	<2	0	4.90±0.25	4.90±0.34
FeN10	>98	<2	0	4.80±0.24	4.80±0.34
FeN15	85	15	0	5.10±0.26	4.34±0.32

The average thickness determined through XRR for each set of deposition conditions and the volume atomic density obtained using the surface atomic density in table 5.1 are presented in table 5.2. These results are consistent with the strong oxidation of the films prepared at room temperature. For these calculations a maximum error of 2 % was assumed for the composition and 5 % for the surface atomic density determined by RBS.

The X-ray diffractograms obtained in $\theta - 2\theta$ geometry are presented in fig. 5.4. No significant diffraction peaks are observed indicating that, regardless of the temperature of deposition, the films deposited on glass (amorphous substrate) have no crystalline order or are composed of polycrystalline grains of size smaller than the resolution of the diffractometer.

All films display ferromagnetic behaviour at room temperature (fig. 5.5). The films deposited at room temperature have smaller saturation magnetization as expected, since iron oxides have smaller magnetic moments than iron nitrides or

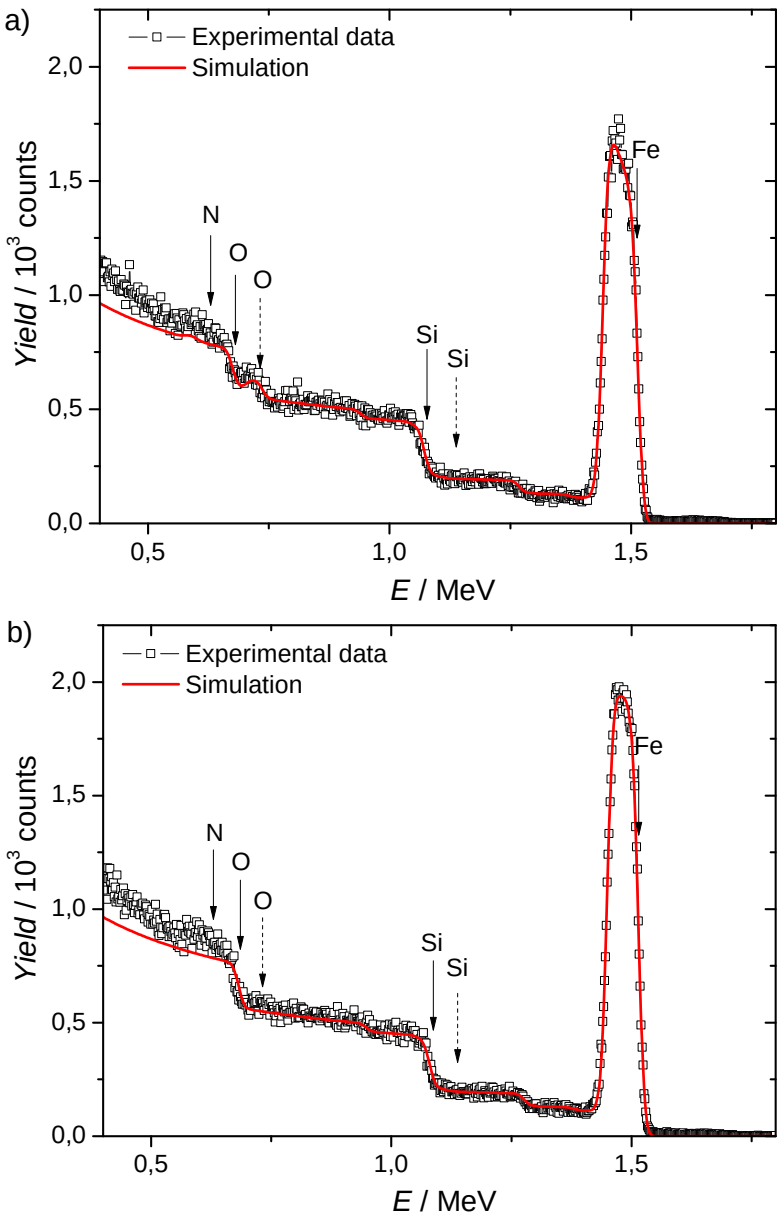

Figure 5.3: RBS results for films a) FeN10RT and b) FeN10. The solid lines correspond to the simulation of each spectrum using the RUMP code. The solid arrows mark the positions of the elements in the spectra and the dashed arrows indicate the expected positions for Si and O if they were present at the surface of the sample.

Table 5.2: Thickness and density of Fe-N films deposited on glass.

	Thickness (nm) (nm)	Atomic density (10^{22} at.cm^{-3})	Fe Atomic density (10^{22} at.cm^{-3})
FeN10RT	85±2	7.41±0.55	5.11±0.53
FeN15RT	83±2	6.27±0.46	5.14±0.51
FeN5	79±2	6.20±0.47	6.20±0.60
FeN10	75±2	6.40±0.49	6.40±0.62
FeN15	77±2	6.62±0.51	5.63±0.57

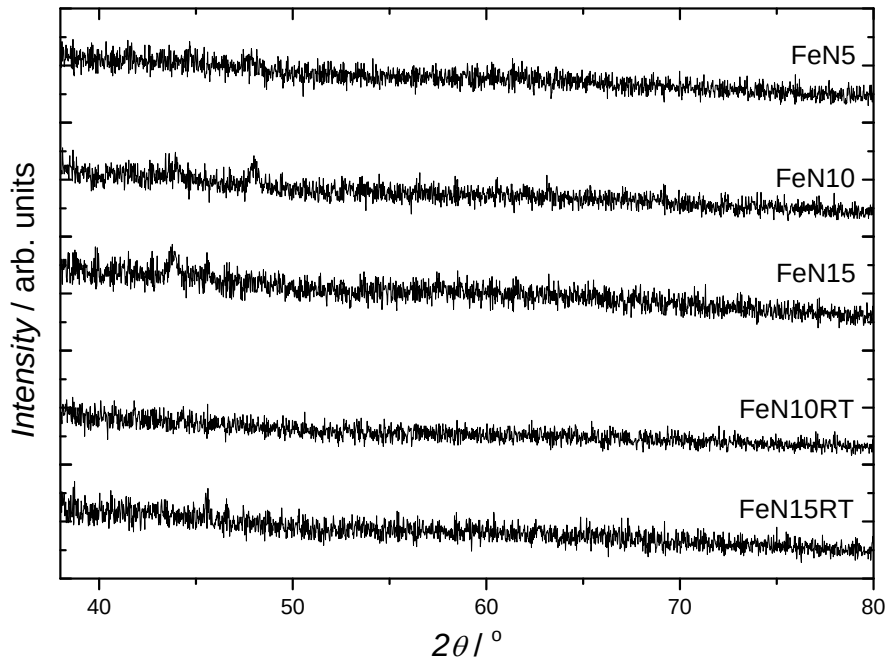

Figure 5.4: XRD diffractograms obtained for Fe-N films deposited on glass in $\theta-2\theta$ geometry.

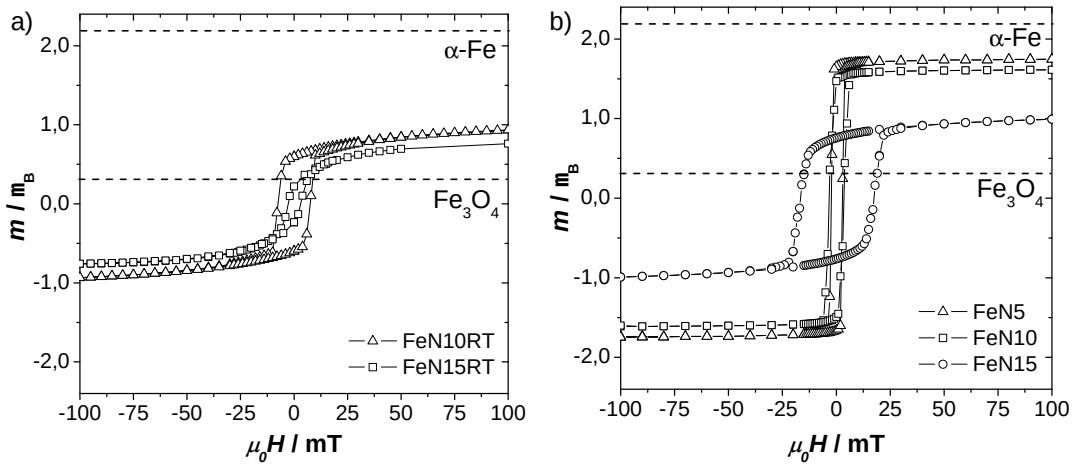

Figure 5.5: Magnetic moment as a function of applied field (measured at 300 K) for films deposited at a) room temperature and b) 250 ^{o}C .

Table 5.3: Magnetic properties of Fe-N films deposited on glass.

	m_s (10^{-6} A.m^2.cm^{-2})	m_s (μ_B/Fe)	H_c (mT)
FeN10RT	4.2	1.0	7.5
FeN15RT	3.4	0.9	3.0
FeN5	8.0	1.8	2.5
FeN10	7.3	1.6	3.5
FeN15	4.0	1.0	17.0

metallic iron [2]. In the case of films deposited at high temperature, FeN5 and FeN10 possess similar saturation magnetization, in agreement with their similar composition determined by RBS. For FeN15 the magnetization decreases significantly. Regarding coercive field (H_c) these films exhibit the same behaviour observed on Co-N films, H_c increasing with increasing nitrogen content.

5.3.2 Fe-N thin films deposited on crystalline substrates

For Fe-N films deposited on the single crystalline substrates, room temperature and 250 ^{o}C deposition were performed to explore the influence of the substrate cristallinity on the oxidation behaviour.

In fig. 5.6 and 5.7 RBS spectra illustrate the results obtained for depositions at RT and at 250^{o}C. Consistently with the results obtained for films deposited on glass, the films deposited at room temperature exhibit significant oxidation spanning throughout the films, while for films deposited at 250 ^{o}C only trace amounts of oxygen in the films are detected for two of the substrates (Al_2O_3 (0001) and MgO (110)). Results also indicate that higher PP(N_2) decreases oxidation, since films deposited at room temperature with PP(N_2) = 10 % have an average oxygen content higher (approximately 26 %) than films deposited with PP(N_2) = 15 % (approximately 19 %) (table 5.4). The same trend is observed for films deposited at 250 ^{o}C where a much lower degree of oxidation was detected (table 5.5).

Table 5.4: Composition and surface density of Fe-N films deposited on single crystalline substrates at room temperature.

Substrate	Fe (at.%)	N (at.%)	O (at.%)	Surface atomic density (10^{17} at.cm^{-2})	Fe surf. atomic density (10^{17} at.cm^{-2})
			FeN10RT		
Al_2O_3 (0001)	56	17	27	6.85±0.34	3.84±0.17
Al_2O_3 (11$\bar{2}$0)	56	21	23	7.00±0.35	3.92±0.17
MgO (100)	56	21	23	7.10±0.36	3.98±0.17
MgO (110)	55	16	30	6.90±0.35	3.80±0.17
			FeN15RT		
Al_2O_3 (0001)	61	20	19	5.85±0.29	3.57±0.15
Al_2O_3 (11$\bar{2}$0)	62	20	18	5.80±0.29	3.60±0.15
MgO (100)	60	20	20	5.90±0.30	3.54±0.15
MgO (110)	61	20	19	5.90±0.30	3.60±0.15

Table 5.5: Composition and surface density of Fe-N films deposited on single crystalline substrates at 250^{o}C.

Substrate	Fe (at.%)	N (at.%)	O (at.%)	Surface atomic density (10^{17} at.cm^{-2})	Fe surf. atomic density (10^{17} at.cm^{-2})
			FeN5		
Al_2O_3 (0001)	86	4	10	5.45±0.27	4.69±0.15
Al_2O_3 (11$\bar{2}$0)	83	17	0	5.55±0.28	4.61±0.15
MgO (100)	86	14	0	5.40±0.27	4.64±0.15
MgO (110)	77	18	5	5.95±0.30	4.58±0.16
TiO_2 (100)	78	22	0	5.70±0.29	4.45±0.15
TiO_2 (110)	80	20	0	5.60±0.28	4.48±0.15
			FeN10		
Al_2O_3 (0001)	75	20	5	5.45±0.27	4.09±0.15
Al_2O_3 (11$\bar{2}$0)	77	23	0	5.50±0.28	4.24±0.15
MgO (100)	88	12	0	5.05±0.25	4.44±0.15
MgO (110)	81	16	3	5.40±0.27	4.37±0.15
TiO_2 (100)	78	22	0	5.40±0.27	4.21±0.15
TiO_2 (110)	80	20	0	5.40±0.27	4.32±0.15
			FeN15		
Al_2O_3 (0001)	73	23	3	5.25±0.26	3.83±0.14
Al_2O_3 (11$\bar{2}$0)	81	19	0	4.95±0.25	4.01±0.14
MgO (100)	76	24	0	5.10±0.26	3.88±0.14
MgO (110)	66	30	4	5.50±0.28	3.63±0.14
TiO_2 (100)	70	30	0	5.30±0.27	3.71±0.14
TiO_2 (110)	68	32	0	5.80±0.29	3.94±0.15

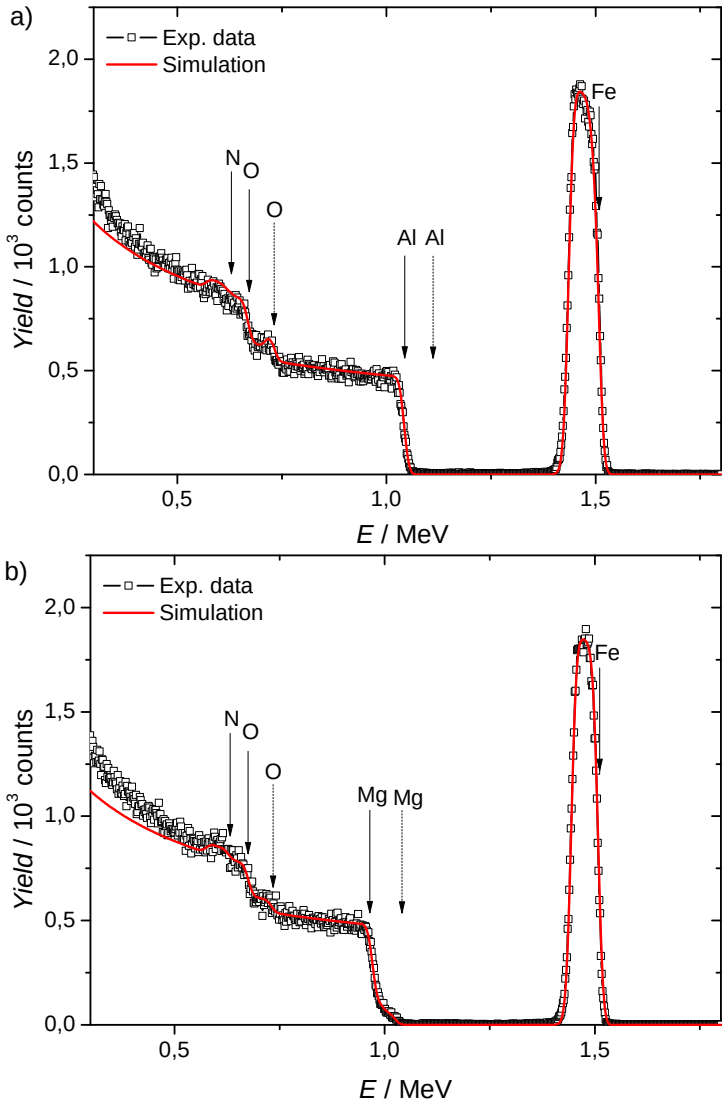

Figure 5.6: RBS spectra for films deposited at RT on a) Al_2O_3 (0001) (PP(N_2)=10 %) and b) MgO (100) (PP(N_2)=15 %). The full arrows mark the observed positions of the elements and the dashed arrows correspond to the expected energies associated with elements of the substrate if they were at the surface of the sample.

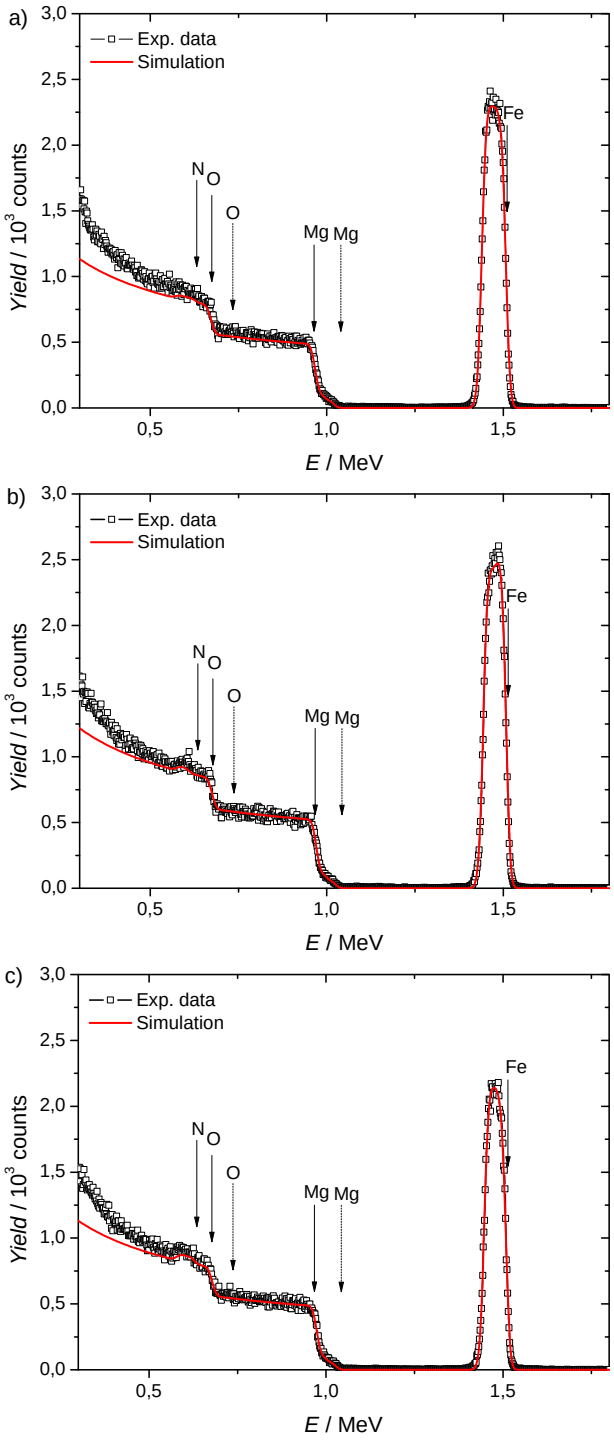

Figure 5.7: RBS spectra obtained for films deposited on MgO (100) at 250^{o}C with a) PP(N_2)=5 %, b) PP(N_2)=10 % and c) PP(N_2)=15 %. The full arrows mark the observed positions of the elements and the dashed arrows correspond to the expected energies associated with elements of the substrate if they were at the surface of the sample.

Table 5.6: Average thickness and density for each group of Fe-N films.

Group	Thickness (nm)	Fe surf. atomic density (10^{17} at.cm^{-2})	Fe atomic density (10^{22} at.cm^{-3})
FeN10RT	94±2	3.88±0.17	4.13±0.27
FeN15RT	75±4	3.58±0.15	4.77±0.46
FeN5	70±2	4.57±0.15	6.53±0.40
FeN10	72±2	4.28±0.15	5.94±0.37
FeN15	64±3	3.83±0.14	5.98±0.50

Despite the presence of oxidation, films deposited at room temperature in crystalline substrates have much higher nitrogen content (between 16 and 21 at.% for FeN10RT and 20 at.% FeN15RT) than the ones deposited on glass. This indicates that the ordered substrate enhances the integration of nitrogen during the films' deposition. Nevertheless the XRD diffractograms of the films deposited at room temperature exhibit no signs of significant crystalline order and no channelling effect is observed by RBS-Channelling .

For films deposited at 250 ^{o}C, the simulation of RBS spectra also indicates that nitrogen content increases with the PP(N_2) during deposition. For FeN5 the average nitrogen content is approximately 16 at.%, while for FeN10 and FeN15 it is 19 at.% and 26 at.%, respectively (table 5.5). With that nitrogen amount, the estimated compositions of FeN10 and FeN15 are very close to Fe_4N and Fe_3N stoichiometries, respectively, which may indicate these to be the main phases present in the films of those groups.

Using the thickness determined by XRR the average Fe atomic density for each group of samples was calculated. These results are presented in table 5.6.

For most films a decrease in yield in the region associated with Fe is observed in the RBS spectra under channelling conditions, indicating that these films have crystalline order and are aligned with the structure of the substrates.

XRD results obtained for the films deposited at 250 ^{o}C confirm these results. Fig. 5.9 shows the XRD diffractograms for the films deposited at 250^{o}C on Al_2O_3 (0001) and TiO_2 (100), which are representative of the results obtained for the films in each group (FeN5, FeN10 and FeN15). For films deposited at PP(N_2)=5 % a mixture of α-Fe and Fe_4N is obtained, at PP(N_2)=10% the main phase becomes Fe_4N (some Fe_3N is visible in the film deposited on the Al_2O_3 sub-

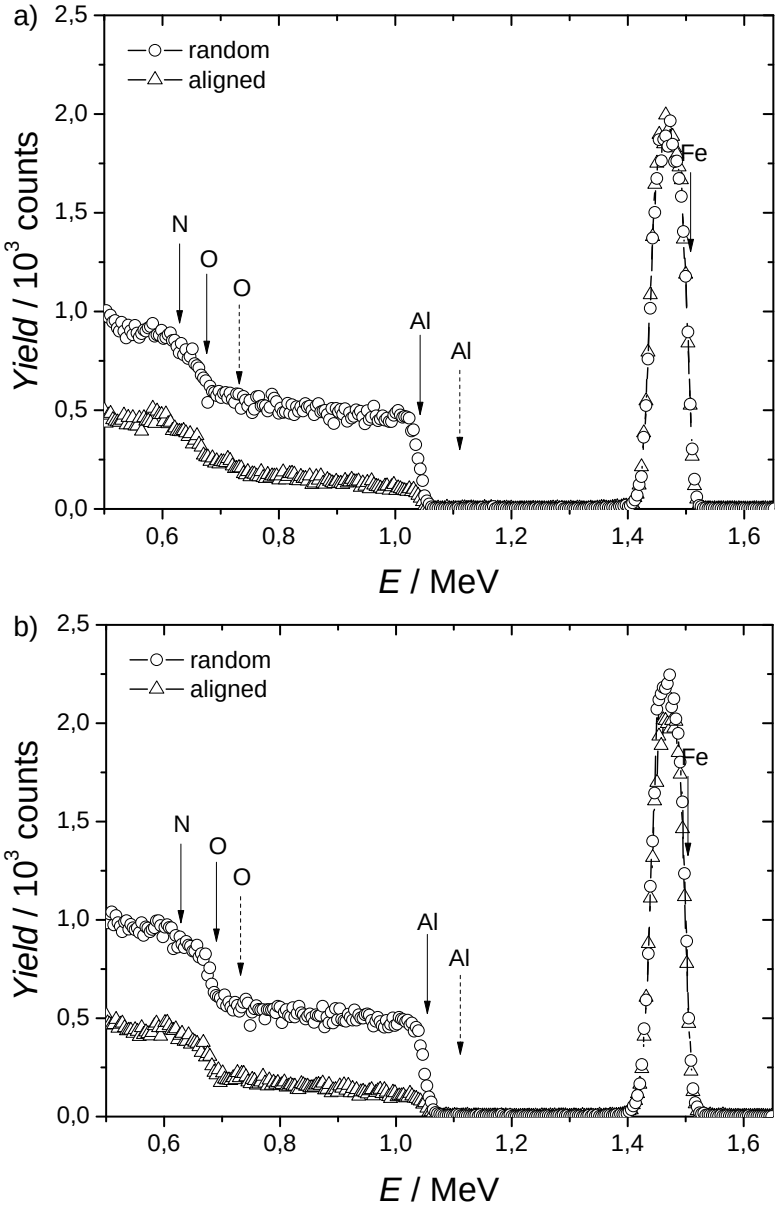

Figure 5.8: RBS spectra obtained in both aligned and random conditions for a) Al_2O_3 (0001)/FeN15RT with no evidence of channelling in the film and b) Al_2O_3 (0001)/FeN15 evidencing channelling in the film, as observed by the Fe yield (between 1.4 and 1.55 MeV). The full arrows mark the observed positions of the elements and the dashed arrows correspond to the expected energies associated with elements of the substrate if they were at the surface of the sample.

strate) and at PP(N_2)=15 %, Fe_3N becomes the predominant phase. The growth of Fe_3N on Al_2O_3 (0001) may be favoured by the hexagonal structure of the substrate.

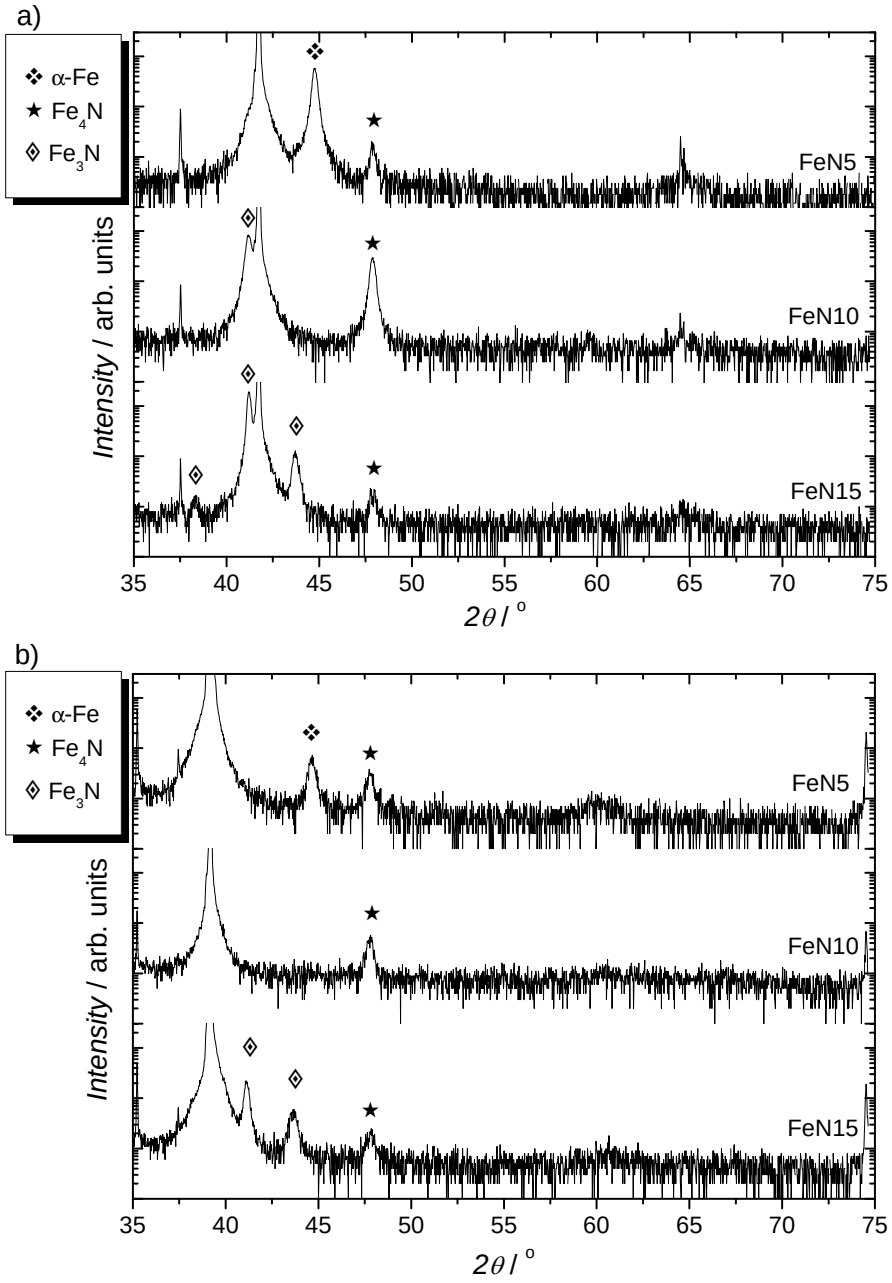

Figure 5.9: XRD difractograms for films deposited at 250^{o}C on a) Al_2O_3 (0001) and b) TiO_2 (100). The unidentified diffraction peaks correspond to the substrate peaks, Al_2O_3 (006) and TiO_2 (200), respectively.

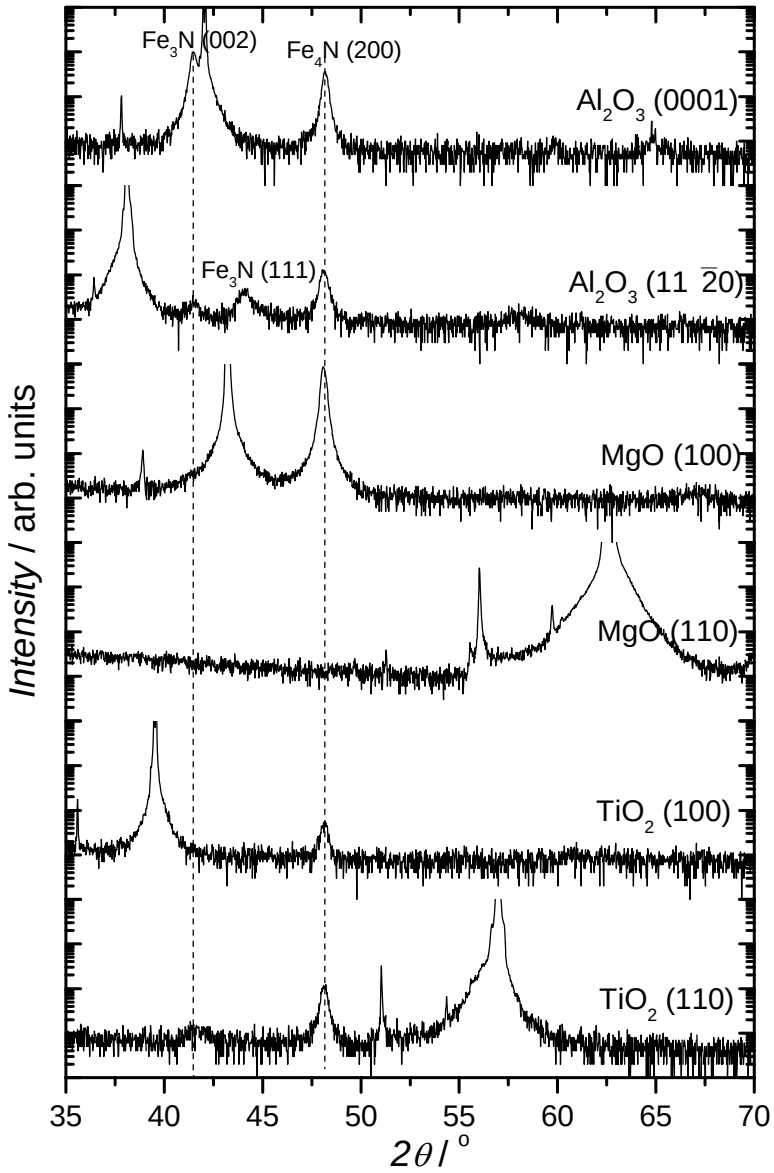

Figure 5.10: XRD diffractograms obtained for each film of FeN10.

Table 5.7: CEMS parameters obtained for Fe-N films deposited on MgO (100) at 250^{o}C. The associated spectra are presented in fig. 5.14.

	Site	B_{hf} (T)	IS (mm/s)	QS (mm/s)	Γ (mm/s)	I (%)	Iron Phase	Atomic composition
FeN5	1	21.5(7)	0.30	0.22	0.30(2)	29.4		
	2	21.8(1)	0.30	-0.43	0.42(6)	14.7	Fe_4N	87% Fe
	3	33.9(2)	0.24	0	0.31(4)	14.7		13% N
	4	33.1(3)	0	0	0.29(2)	41.2	α-Fe	
FeN10	1	21.7(5)	0.30	0.22	0.29(1)	50		
	2	21.9(1)	0.30	-0.43	0.35(3)	25	Fe_4N	80% Fe
	3	33.9(1)	0.24	0	0.28(3)	25		20% N
FeN15	1	21.6(1)	0.30	0.22	0.25(4)	22		
	2	21.6(2)	0.30	-0.43	0.28(7)	11	Fe_4N	76% Fe
	3	34.2(2)	0.24	0	0.26(8)	11		24% N
	4	22.0(2)	0.33(2)	0(1)	0.58(4)	56	$Fe_{3-x}N$	

In fig. 5.10, the comparison of the XRD results for FeN10 films in different substrates is shown. The Fe_4N (200) diffraction peak is always present, regardless of the substrate (except for the case of MgO (110) where no diffraction peaks are observed). This indicates that Fe_4N grows preferentially along a [100] direction, independently of the structure of the underlying substrate.

For all films, AFM measurements were performed in AC mode (fig. 5.11). The average roughness was determined for each group and is presented in fig. 5.12 with the error bars representing the standard deviation. Films deposited at high temperature display rougher surfaces (with rms roughness between 3 to 5 nm) than films deposited at RT (1 to 3 nm). This result agrees with the oriented growth in higher temperature depositions. While small nano-aggregates in a polycrystalline film can fit together in a packed structure that causes the surface to exhibit very small roughness, film growth with crystalline orientation occurring by island formation, that increase in size and group together in a relatively irregular manner, corresponds to rougher film surfaces (Volmer-Weber or Stranski-Krastanov growth).

To confirm the composition of the films CEMS spectra were obtained at room temperature for selected samples. The typical results obtained for films deposited at RT (illustrated in fig. 5.13) can only be fitted resorting to a distribution of hyperfine fields, indicating that no definite phase can be identified.

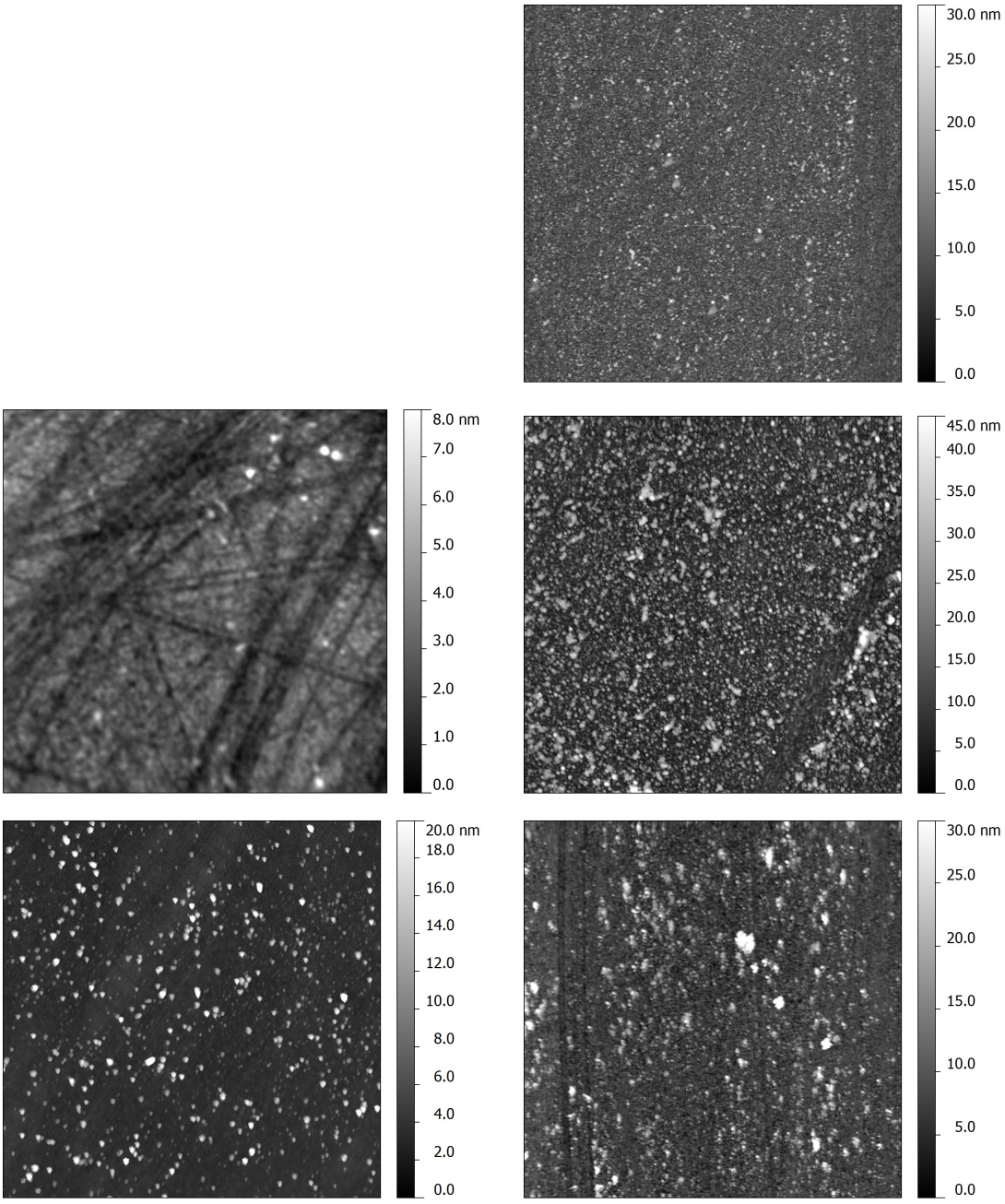

Figure 5.11: AFM 10x10 μm^2 images of the films deposited at RT on Al_2O_3 (0001) (left) and on TiO_2 (100) at 250^o C (right) with the different PP(N_2): top) 5%, middle) 10%, bottom) 15%.

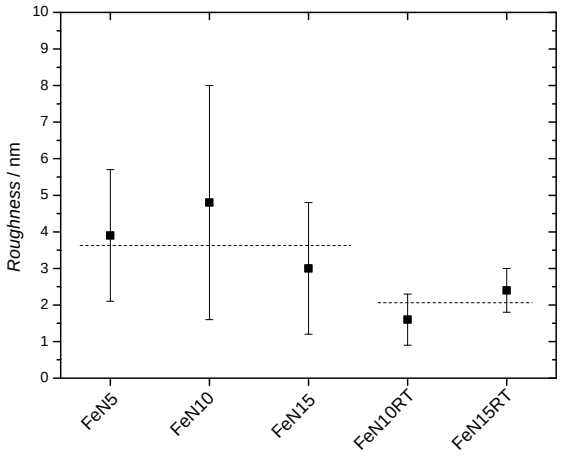

Figure 5.12: Average roughness for each group of Fe-N films, determined by AFM. The dashed lines correspond to the average roughness obtained for films deposited at 250^{o}C and RT, respectively.

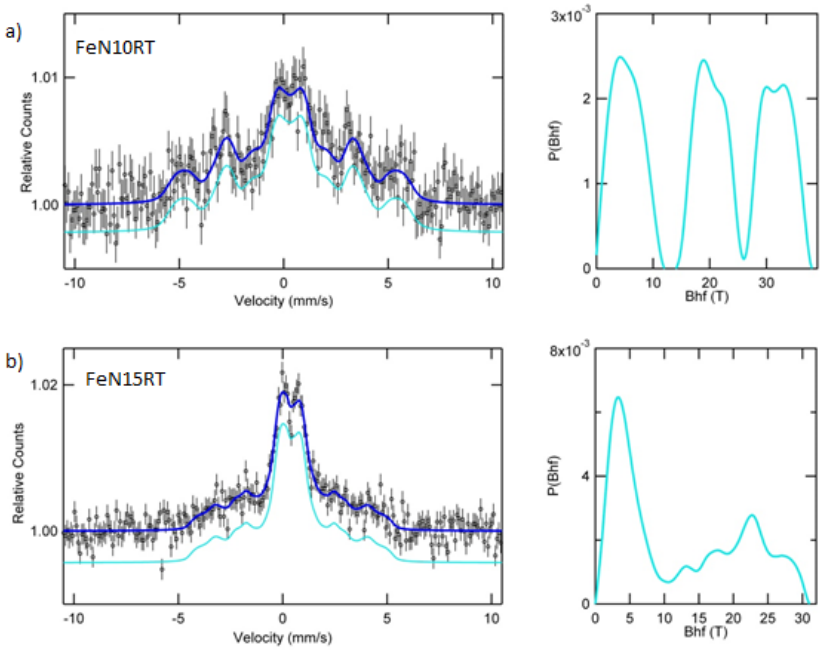

Figure 5.13: CEMS spectra for films deposited on MgO (100) at room temperature with a) PP(N_2)=10% and b) PP(N_2)=15%

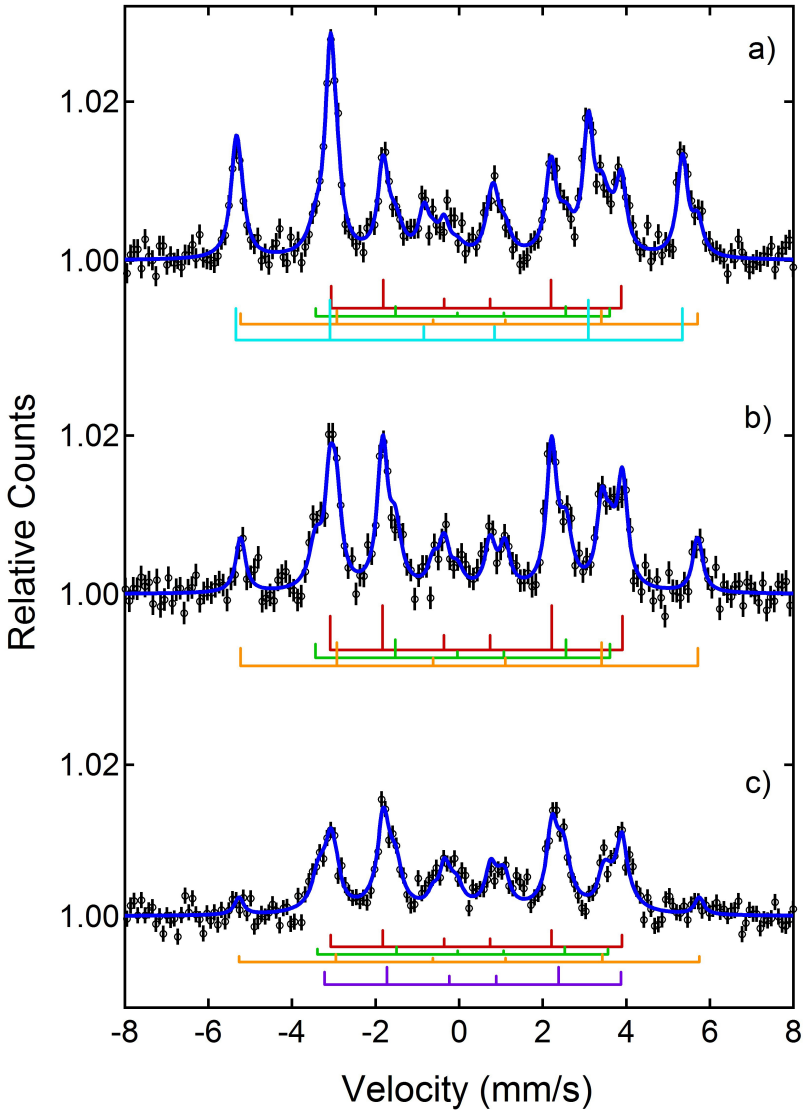

Figure 5.14: CEMS spectra for films a) FeN5, b) FeN10 and c) FeN15 films deposited on MgO (100). The associated parameters can be found on table 5.7.

For films deposited at 250 ^{o}C the CEMS spectra are very different (fig. 5.14) and can be well fitted with a combination of the spectra of iron and/or iron nitrides (depending on the sample). The parameters characterizing the spectra shown in fig. 5.14 are presented in Table 5.7.

In the case of FeN5 films, the sextet associated with α-Fe and the three sextets characteristic of Fe_4N coexist. The same three sextets are dominant in the FeN10 spectra and can be used alone to obtain good fits of the experimental results. For FeN15 films, the CEMS spectra can be fitted using a mixture of Fe_4N and Fe_3N. Using the intensity of the fitted components it was possible to estimate the ratio of the constituent phases and consequently the composition of the films (table 5.7), which was found to be in excellent agreement with the compositions estimated by RBS analysis.

As for the magnetic behaviour, all films are ferromagnetic at room temperature. Representative results of the magnetic behaviour for films deposited at room temperature are shown in fig. 5.15 and the relevant magnetic characteristics are presented in Table 5.8. The films' saturation magnetization and coercive field exhibit the same behaviour that was observed for films deposited in glass, with the magnetic moment decreasing and coercive field increasing with increasing nitrogen content. Nevertheless, although this behaviour is qualitatively similar, the magnetic moment of films deposited on single crystalline substrates is larger, indicating that even though these films have negligible crystalline order, the substrates still influence their magnetic properties. In these films, no magnetic anisotropy is observed, which comes as no surprise given their lack of crystalline order.

For the films deposited at 250 ^{o}C the magnetization hysteresis are presented in fig. 5.16 - 5.18 and the corresponding parameters are summarized in table 5.9.

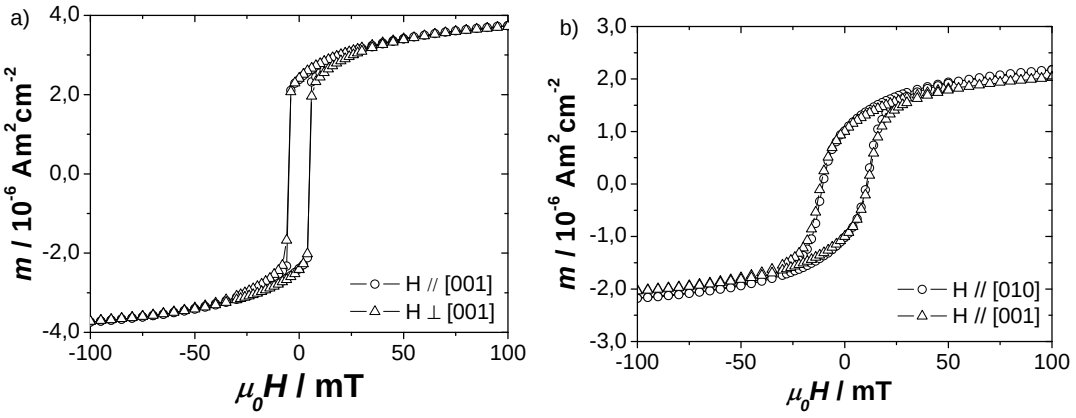

Figure 5.15: Magnetic moment as a function of applied magnetic field measured in two in-plane perpendicular directions of films a) Al_2O_3 (0001)/FeN10RT and b) MgO (100)/FeN15RT.

Table 5.8: Magnetic properties of films deposited at RT.

Substrate	Direction	H_c (mT)	m_s (10^{-6} Am^2/cm^2)	m_s (μ_B/Fe)
		FeN10RT		
Al_2O_3 (0001)	H$\|\|$[010]	5.0	4.43	1.25
	H$\perp$[010]	5.0		
Al_2O_3 (11$\bar{2}$0)	H$\|\|$[001]	5.0	4.40	1.22
	H$\perp$[001]	5.0		
MgO (100)	H$\|\|$[001]	5.0	4.18	1.14
	H$\perp$[001]	6.5		
		FeN15RT		
Al_2O_3 (0001)	H$\|\|$[010]	8.0	3.14	0.94
	H$\perp$[010]	9.0		
Al_2O_3 (11$\bar{2}$0)	H$\|\|$[001]	8.3	3.07	0.93
	H$\perp$[001]	7.3		
MgO (100)	H$\|\|$[001]	10.8	2.70	0.82
	H$\perp$[001]	10.8		

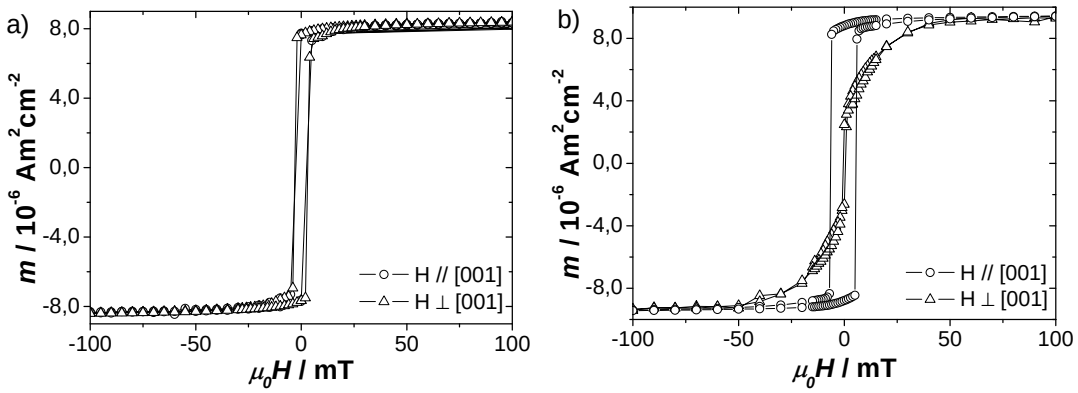

Figure 5.16: Magnetic results for films of group FeN5 deposited on a) MgO (100) b) MgO (110)

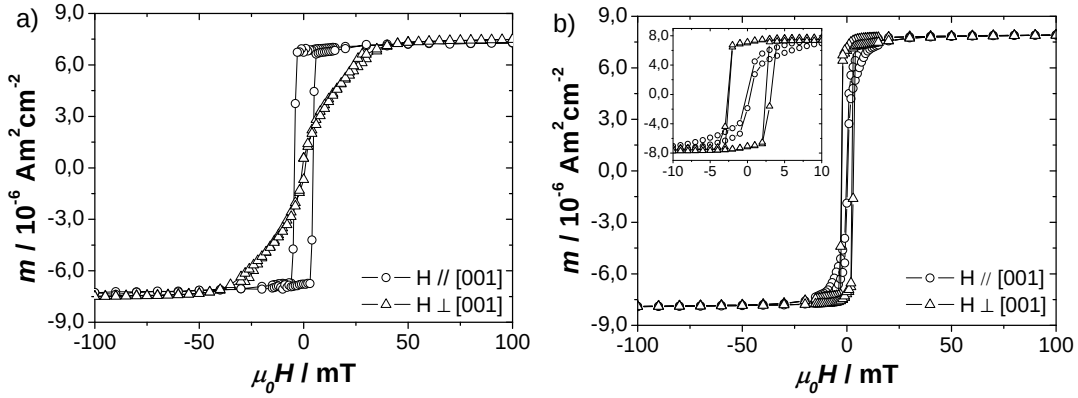

Figure 5.17: Magnetic results for films of group FeN10 deposited on a) MgO (110) b) TiO_2 (100)

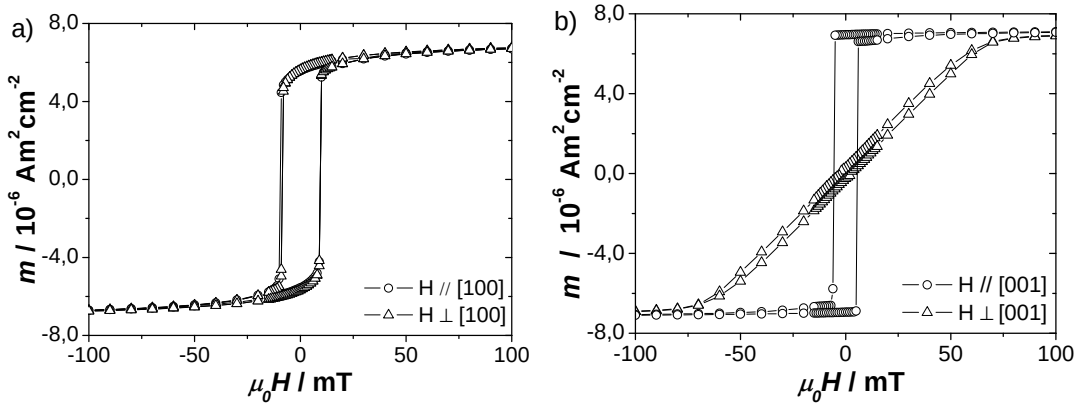

Figure 5.18: Magnetic results for films of group FeN15 deposited on a) Al_2O_3 (0001) and b) MgO (110).

Table 5.9: Magnetic properties of films deposited at 250^{o}C.

Substrate	Direction	H_c (mT)	m_s (10^{-6} Am^2/cm^2)	m_s (μ_B/Fe)
		FeN5		
Al_2O_3 (0001)	H$\|$[010]	2.5	9.27	2.07
	H$\perp$[010]	3.5		
Al_2O_3 (11$\bar{2}$0)	H$\|$[001]	1.0	8.70	2.03
	H$\perp$[001]	3.5		
MgO (100)	H$\|$[001]	3.0	8.66	2.01
	H$\perp$[001]	3.0		
MgO (110)	H$\|$[001]	6.5	9.77	2.29
	H$\perp$[001]	0.5		
TiO_2 (100)	H$\|$[001]	1.0	9.20	2.24
	H$\perp$[001]	2.0		
TiO_2 (110)	H$\|$[001]	1.0	9.06	2.18
	H$\perp$[001]	2.5		
		FeN10		
Al_2O_3 (0001)	H$\|$[010]	3.5	8.19	2.15
	H$\perp$[010]	2.5		
Al_2O_3 (11$\bar{2}$0)	H$\|$[001]	1.2	7.81	1.98
	H$\perp$[001]	3.0		
MgO (100)	H$\|$[001]	4.5	7.65	1.86
	H$\perp$[001]	4.5		
MgO (110)	H$\|$[001]	4.2	7.61	1.88
	H$\perp$[001]	0.5		
TiO_2 (100)	H$\|$[001]	0.2	8.05	2.05
	H$\perp$[001]	2.5		
TiO_2 (110)	H$\|$[001]	0.5	8.38	2.08
	H$\perp$[001]	2.5		
		FeN15		
Al_2O_3 (0001)	H$\|$[010]	9.0	7.02	1.97
	H$\perp$[010]	9.0		
Al_2O_3 (11$\bar{2}$0)	H$\|$[001]	16.5	6.38	1.71
	H$\perp$[001]	7.0		
MgO (100)	H$\|$[001]	6.5	5.91	1.64
	H$\perp$[001]	6.5		
MgO (110)	H$\|$[001]	5.5	7.19	2.08
	H$\perp$[001]	2.0		
TiO_2 (100)	H$\|$[001]	10.0	6.25	1.82
	H$\perp$[001]	17.5		
TiO_2 (110)	H$\|$[001]	13.5	6.04	1.65
	H$\perp$[001]	6.0		

The comparison of the magnetic moment as a function of applied magnetic field along two different perpendicular in-plane directions show that most of the films exhibit magnetic anisotropy. Since α-Fe and Fe_4N have cubic structures, it would be expected that two perpendicular in-plane directions were equivalent in terms of magnetic behaviour, but in films deposited on substrates with non-equivalent in-plane perpendicular directions magnetic anisotropy is observed. This result becomes even more significant for FeN10 films (mainly (100)-oriented Fe_4N) since the <100> direction was expected to be the easy axis of magnetization [11; 77] and two of these directions lay on the film's plane. For anisotropic substrates the films display magnetic anisotropy and no magnetic anisotropy was observed for films deposited on MgO (100), which also has a cubic structure and equivalent in-plane directions. A strong influence of the substrate causes the easy axis to change depending on the substrate.

5.3.3 Fe/Fe-N multilayers

To study the use of nitride films in spintronic devices three groups of bi-layers were produced (Groups A-C) and one three-layer set (Group D) with the following stack (with the expected thickness presented in nm):

Group A Substrate / Fe 20 / Fe-N 20

Group B Substrate / Fe 10 / Fe-N 10

Group C Substrate / Fe-N 10 / Fe 10

Group D Substrate / Fe-N 10 / Fe 10 / Fe-N 10

The substrates used for the preparation of these samples were the ones where better epitaxy was found for individual films: Al_2O_3 (0001), Al_2O_3 (11$\bar{2}$0), MgO (100) and MgO (110) with the deposition conditions for Fe_4N.

RBS analysis performed in both random and alignment conditions (*i.e.* with the $^4He^+$ beam aligned with the principal direction of the substrates) indicates that the multilayers present an ordered structure aligned with the substrates' since a significant reduction in yield is observed in the region of the spectra associated

with Fe in the aligned spectra (Fig. 5.19). This decrease is observed in all samples of all groups.

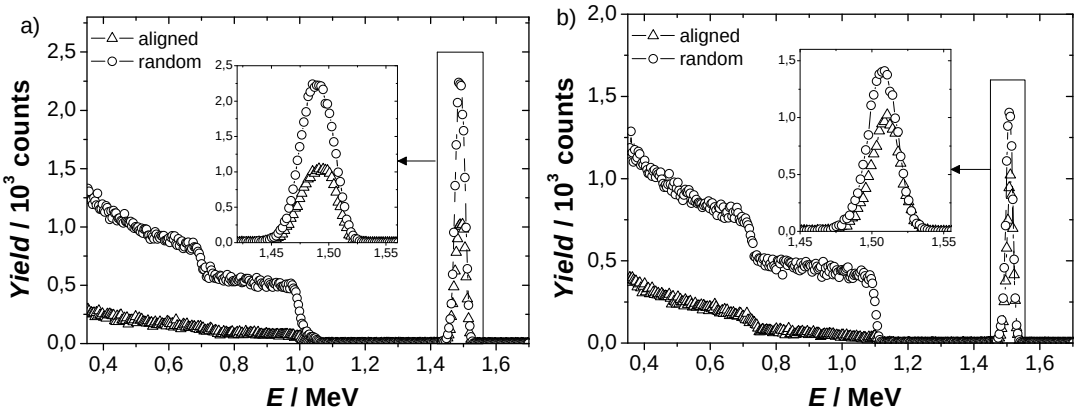

Figure 5.19: Spectra of RBS-Channelling obtained for a) MgO (100)/Fe/Fe-N (Group A) and b) Al_2O_3 (0001)/Fe/Fe-N (Group B).

Since the layers of these samples have very small thickness (max. 20 nm) RBS spectra were collected for a 40^o inclination between the films' normal and the incident beam, increasing the film length traversed by the ion beam and enlarging the profile of Fe, to have higher sensitivity for detecting changes in yield associated with the different composition in the layers. Unfortunately, even for this angle, the very small thickness of the films does not allow to resolve the differences in composition and good simulations of the experimental data are obtained both using two different layers (or three in the case of Group D) with alternating Fe and Fe-N compositions or using one layer with a mixture of Fe and N (fig. 5.20). Since it was not possible to distinguish between a system consisting of very thin distinct multilayers or one larger layer with a mixture of Fe and N, the obtained compositions presented in table 5.10 correspond to the average composition obtained considering only one layer for groups A through C. For group D, the spectra showed signs of surface oxidation and two layers were used to account for oxide at the surface.

The XRD results (fig. 5.21) are consistent with the presence of several nitride phases, indicating that Fe does not appear clearly individualized. Nitrides are interstitial compounds and nitrogen diffusion at the deposition temperature used for nitride production (250 ^{o}C) may explain the intermixing between adjacent

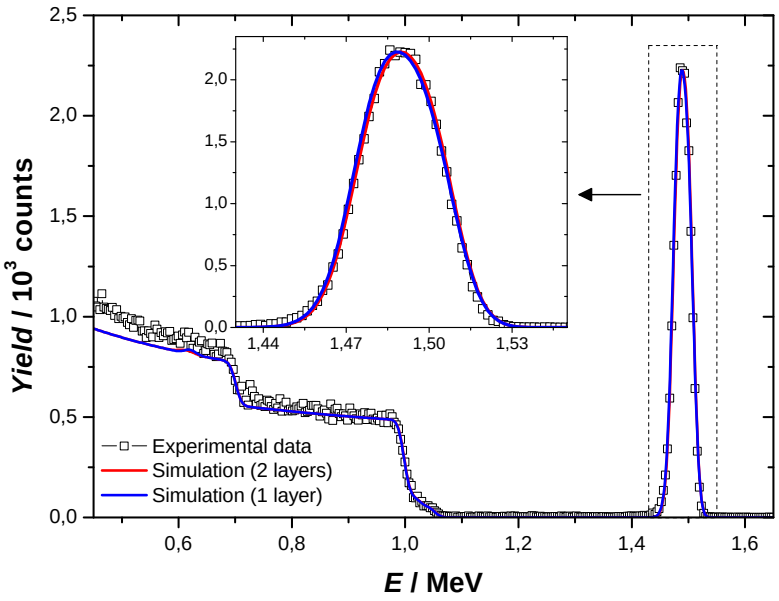

Figure 5.20: Comparison of simulations obtained for MgO (100)/Fe/Fe-N (Group A) using 2 layers or only 1 layer.

Table 5.10: Composition and surface density of multilayered samples.

Substrate	Fe (at.%)	N (at.%)	O (at.%)	Surface atomic density (10^{17} at.cm^{-2})	Fe surf. atomic density (10^{17} at.cm^{-2})
			Group A		
Al_2O_3 (0001)	83.5	16.5	0.0	2.65	2.21
Al_2O_3 (11$\bar{2}$0)	85.9	14.1	0.0	2.95	2.53
MgO (100)	83.3	16.7	0.0	2.85	2.37
MgO (110)	74.0	26.0	0.0	3.15	2.33
			Group B		
Al_2O_3 (0001)	100.0	0.0	0.0	1.25	1.25
Al_2O_3 (11$\bar{2}$0)	93.2	6.8	0.0	1.25	1.17
MgO (100)	84.4	15.6	0.0	1.25	1.06
MgO (110)	84.6	15.4	0.0	1.25	1.06
			Group C		
Al_2O_3 (0001)	93.4	6.6	0.0	1.33	1.24
Al_2O_3 (11$\bar{2}$0)	95.1	4.9	0.0	1.22	1.16
MgO (100)	82.8	17.2	0.0	1.30	1.08
MgO (110)	87.3	12.7	0.0	1.30	1.14
			Group D		
Al_2O_3 (0001)	82.2	9.3	8.5	2.05	1.67
Al_2O_3 (11$\bar{2}$0)	87.0	3.3	9.7	1.55	1.35
MgO (100)	89.1	4.6	6.3	1.90	1.69
MgO (110)	73.0	13.0	13.9	2.30	1.68

layers. The layer intermixing is also favoured by the roughness of the nitride films (3-5 nm).

The mixture of phases observed can also be a direct result from the small thickness of each layer. During growth the layers tend to grow as scattered islands that merge to form a uniform layer. However, in small thickness layers, as is the case for these samples, this growth process can lead to the formation of layers with holes in them that are then filled with the deposition of the following layer. This can also explain why it was not possible to observe distinct layers in RBS measurements.

Magnetic characterization also indicates the coexistence of different magnetic phases in these samples. Measurements of the magnetic moment as a function of temperature (measured at 5 mT) for the bi-layer of Group B deposited on MgO (110) in zero field-cooled (ZFC) and field-cooled (FC) configurations, are presented in fig. 5.22 as an example of this behaviour. At room temperature all samples exhibit ferromagnetic behaviour (fig. 5.23), with many of these also displaying an added diamagnetic component associated with the presence of the diamagnetic iron nitride Fe_2N as detected in the XRD results. The magnetic characteristics of the samples under study are summarized in table 5.11.

Anisotropic behaviour is observed in all samples except those deposited on MgO (100) from group A and B and Al_2O_3 (0001) from group B. Given that anisotropic behaviour was also observed in thin films deposited on MgO (100), which had not happened in the case of single layers, it seems the interactions of the different compounds in the formed layers play a significant role in the appearance of anisotropic behaviour. Due to the nature of these samples it is impossible at this point to determine with certainty if the observed anisotropy arises from the influence of the substrate, as was argued for systems consisting of one uniform layer, or from the influence of the different nitride phases in the formed mixture. Further investigations would be needed to accurately determine the true source of this behaviour.

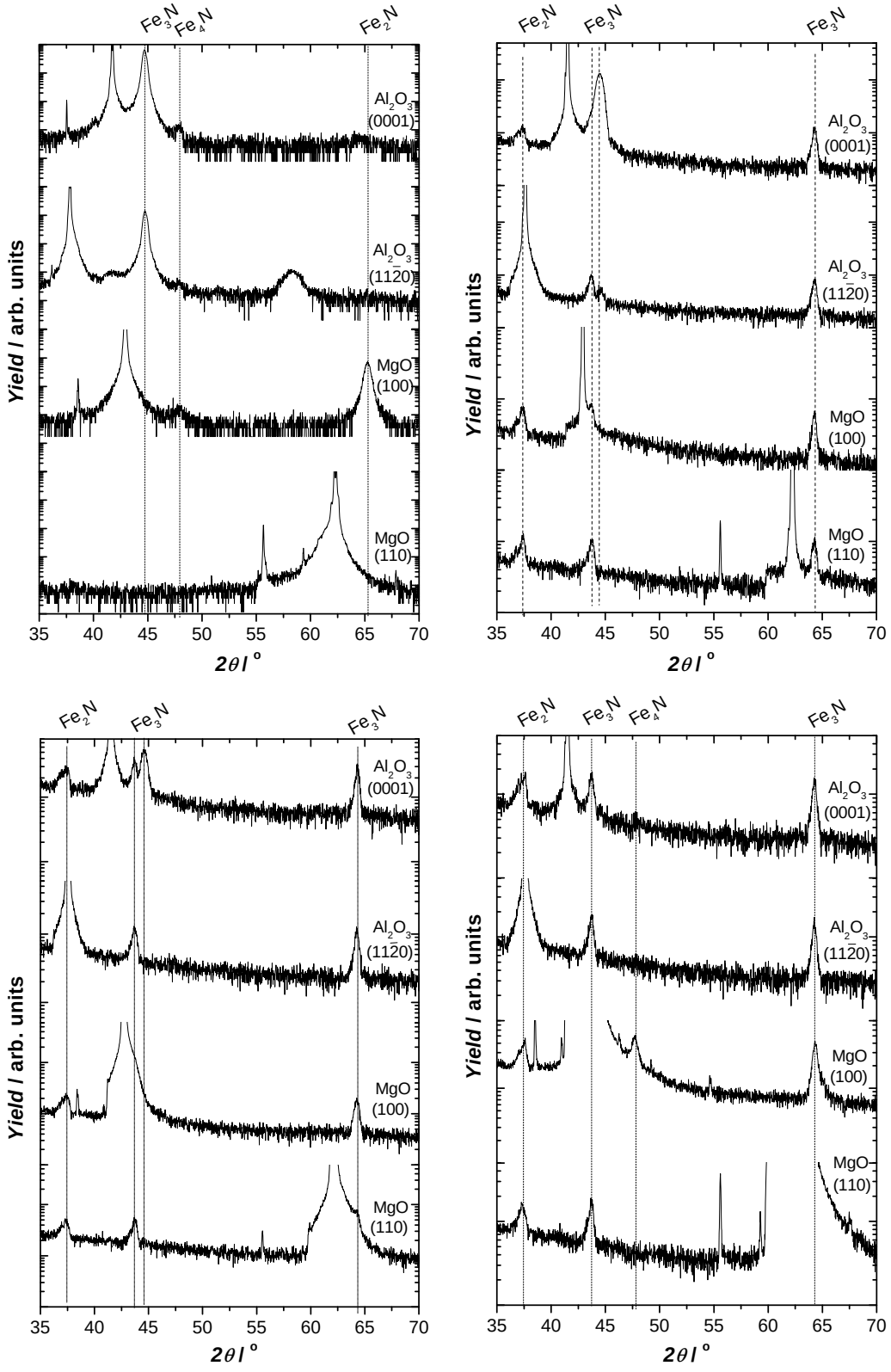

Figure 5.21: XRD diffractograms obtained in $\theta - 2\theta$ geometry for the different sample groups: top left - Group A, top right - Group B, bottom left - Group C, bottom right - Group D.

Table 5.11: Magnetic properties of films deposited at 250^{o}C.

Substrate	Direction	H_c (mT)	m_s (10^{-6} Am^2/cm^2)	m_s (μ_B/Fe)
		Group A		
Al_2O_3 (0001)	H$\|$[010]	2.5	4.32	2.11
	H$\perp$[010]	1.5		
Al_2O_3 (11$\bar{2}$0)	H$\|$[001]	5.0	4.90	2.09
	H$\perp$[001]	6.5		
MgO (100)	H$\|$[001]	5.0	4.19	1.91
	H$\perp$[001]	5.0		
MgO (110)	H$\|$[001]	6.5	3.94	1.82
	H$\perp$[001]	2.5		
		Group B		
Al_2O_3 (0001)	H$\|$[010]	7.0	2.19	1.89
	H$\perp$[010]	7.0		
Al_2O_3 (11$\bar{2}$0)	H$\|$[001]	4.5	2.20	2.03
	H$\perp$[001]	7.0		
MgO (100)	H$\|$[001]	7.5	1.87	1.90
	H$\perp$[001]	7.5		
MgO (110)	H$\|$[001]	11.5	1.99	2.02
	H$\perp$[001]	15.0		
		Group C		
Al_2O_3 (0001)	H$\|$[010]	1.0	2.40	2.09
	H$\perp$[010]	1.0		
Al_2O_3 (11$\bar{2}$0)	H$\|$[001]	3.0	2.38	2.21
	H$\perp$[001]	0.0		
MgO (100)	H$\|$[001]	2.0	2.35	2.35
	H$\perp$[001]	1.0		
MgO (110)	H$\|$[001]	1.0	2.23	2.11
	H$\perp$[001]	1.0		
		Group D		
Al_2O_3 (0001)	H$\|$[010]	1.0	3.59	2.32
	H$\perp$[010]	0.5		
Al_2O_3 (11$\bar{2}$0)	H$\|$[001]	0.5	2.87	2.29
	H$\perp$[001]	3.0		
MgO (100)	H$\|$[001]	1.0	3.38	2.16
	H$\perp$[001]	3.0		
MgO (110)	H$\|$[001]	1.0	3.15	2.02
	H$\perp$[001]	3.0		

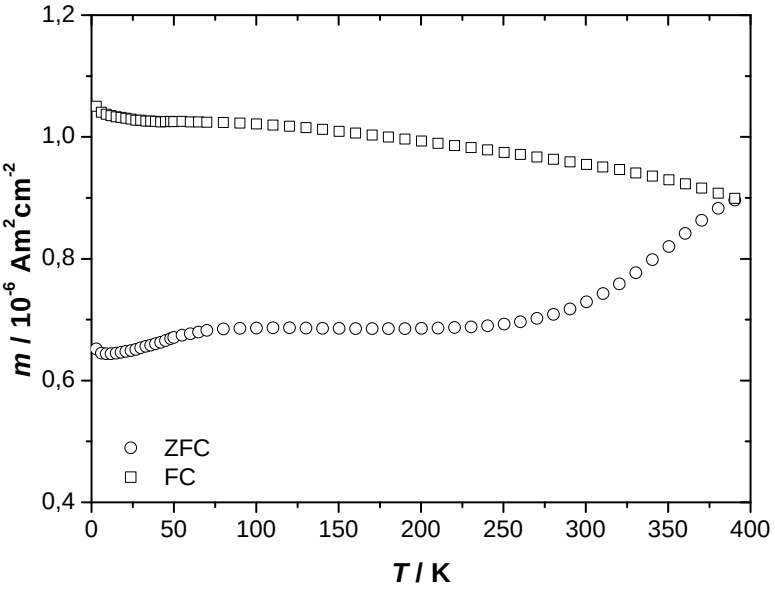

Figure 5.22: Magnetic moment as a function of temperature (measured with an applied field of 5 mT) of sample of Group B deposited on MgO (110).

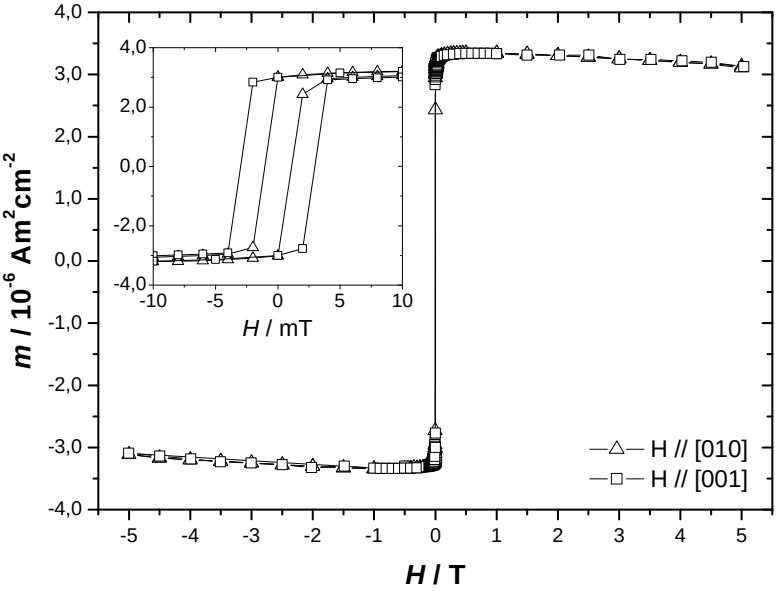

Figure 5.23: Magnetic moment as a function of applied magnetic field measured at room temperature for the sample deposited on MgO (100) of group D. In inset a detail of the low field region is shown.

5.4 Main results obtained for Fe-N films

Thin films

- Films with poor crystalline quality were obtained from depositions performed at room temperature or using glass as a substrate;
- Deposition at room temperature favoured the appearance of iron oxide (more important for depositions on glass substrates than in crystalline substrates);
- Magnetic moments of the films deposited on crystalline substrates are greater than those of films deposited on glass, even in the case of room temperature depositions;
- Higher N content is obtained for films with better crystalline quality;
- Fe_4N is obtained in depositions at 250^oC with $PP(N_2)$=10% having (100) orientation regardless of the orientation of the underlying substrate;
- Significant in-plane anisotropy is observed due to the film/substrate interface stresses;

Multilayers

- The samples obtained do not show sharp interfaces, being probably a mixture of different phases explained by the growth process of layers with small thickness and the diffusion of nitrogen between layers resulting from the high temperature of deposition;
- Anisotropic behaviour was observed for the multilayers produced.

Chapter 6

Characterization of implanted single crystals

6.1 Introduction

In order to study the role of the interfaces in the magnetic behaviour of the nanostructured systems, two groups of Al_2O_3, MgO and TiO_2 single crystals were implanted with Co+N and Fe+N, respectively, at room temperature aiming at producing magnetic nitrides.

There are a few existing works which aim at the production of iron and cobalt nitrides using ionic implantation. However, all the reports found on this line of research are of nitrogen implanted on bulk samples or thin films of the metals [78; 79]. No report of similar work was found.

6.2 Experimental details

The nominal fluences used were chosen in the ratio 4:1 aiming at the production of X_4N nitride (X=Fe,Co) as 2×10^{17} at/cm^2 and 5×10^{16} at/cm^2, for Co/Fe and N respectively. The corresponding energies of implantation were determined using SRIM calculations giving 110 keV for metallic ions and 35 keV for nitrogen. With these energies the implanted region would span approximately 100 nm and the maximum concentration of each implanted element would be at the same depth

(fig. 6.1).

Knowing that for films 250^{o}C is a good temperature for crystallization of nitrides, the samples underwent thermal treatment at 250 ^{o}C in vacuum for 1 hour, to allow rearrangement of the implanted elements and recovery of the lattice. Structure, composition and magnetic properties were characterized in both as implanted and annealed states.

6.3 Results and Discussion

Fig. 6.2 illustrates the typical RBS results obtained for these samples after implantation for the incident beam aligned with the crystallographic axis normal to the crystal ("aligned") and for the incident beam in a random direction ("random"). The spectrum obtained for the unimplanted crystal, in aligned conditions, is also shown for comparison. The aligned spectrum of each sample displays high yield in the implanted depth regions (shaded in grey) indicating strong dechannelling of the incident beam, consistent with highly damaged regions of the host lattice.

After implantation the average yield in the aligned spectrum is approximately 57 % and 54 % of the same value for random spectra for Co+N and Fe+N samples, respectively, while prior to implantation the respective yield was only 3 %, indicating that the good crystalline quality of the crystals before implantation is partially destroyed by the massive changes that occur in the implanted region.

Simulation of the RBS spectra allows to determine the effective implanted fluences of the implanted elements and their respective profile of implantation inside the oxide crystals.

In fig. 6.3 and 6.4 examples of the RBS spectra and their corresponding simulations are shown, along with the in depth profiles of implantation determined for the different elements. The obtained implantation profiles indicate that the implanted elements are concentrated closer to the surface of the crystal than was expected based on the SRIM simulations. This difference can be explained considering the influence of two phenomena not accounted for in the simulations: sputtering of the surface during the implantation process, that erodes the first layers of the host lattice causing the implanted elements to appear closer to the surface, and modification of the matrix density by the implanted ions since the simulation code used

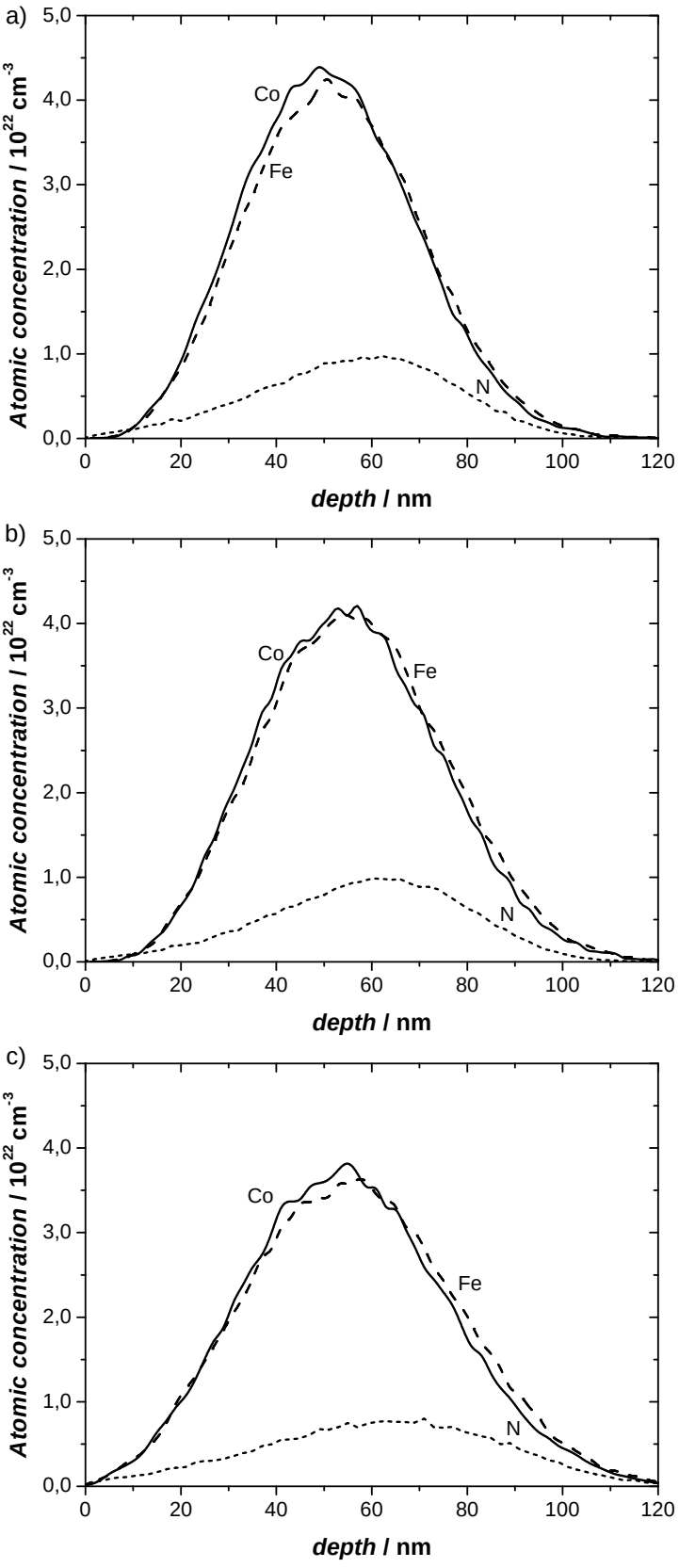

Figure 6.1: SRIM calculation for implantation of Co, Fe and N with 110 keV for the metals and 35 keV for nitrogen, respectively, in a) Al_2O_3, b) MgO and c) TiO_2.

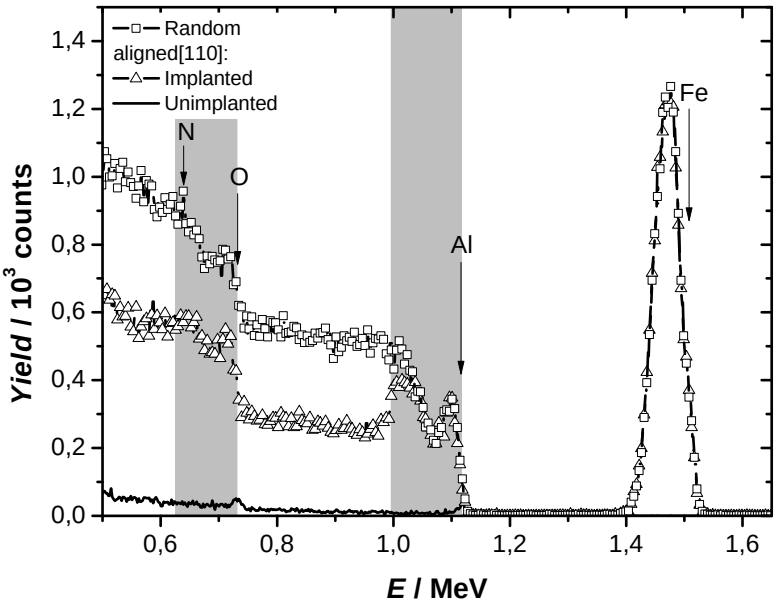

Figure 6.2: RBS spectra obtained for Al_2O_3 $(11\bar{2}0)$ implanted with Fe and N in aligned and random conditions.

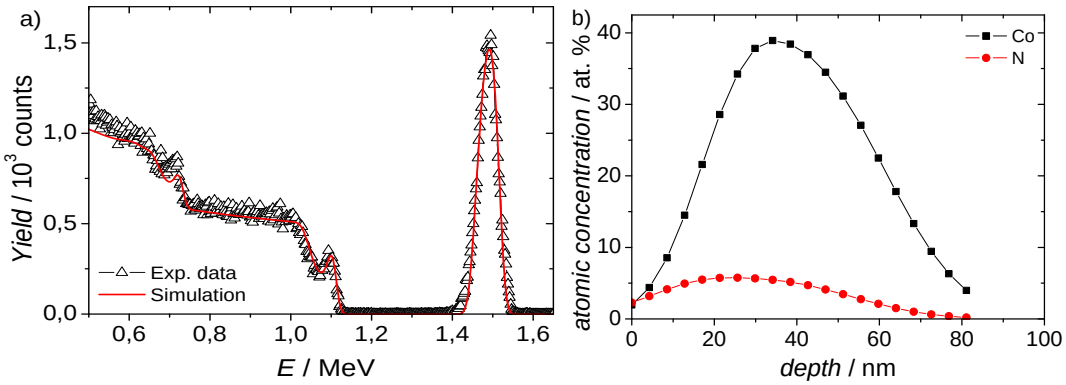

Figure 6.3: a) Comparison between the RBS spectrum obtained for Al_2O_3 $(11\bar{2}0)$ implanted with Co and N and the simulated spectrum obtained with RUMP; b) Atomic concentration of the implanted elements in depth.

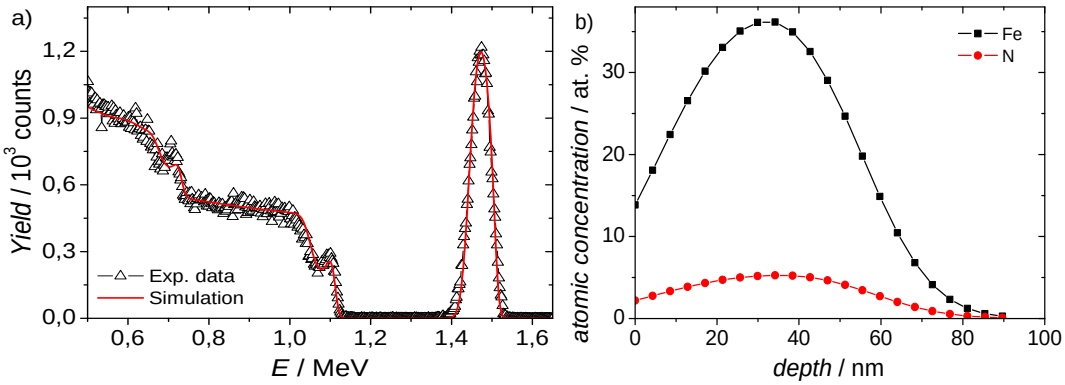

Figure 6.4: a) RBS spectrum and respective RUMP simulation obtained for Al_2O_3 (0001) implanted with Fe and N, b) Profiles of implantation of Fe and N in Al_2O_3 (0001).

to determine the expected distribution of implanted ions in the lattice considers that every implanted ion encounters a virgin matrix, *i.e.* without changes in density and/or structure. The sputtering effect is too small to explain the difference observed but the density modification is important for the high fluences used for the metal ions (2×10^{17} at/cm^2). In the profile of implantation determined by RBS (fig. 6.3 b) and 6.4 b)) the maximum concentration of Fe reaches nearly 40% of the atoms in that region, which means that the proportion between Co (or Fe) and Al is of the order of 1:1 and therefore the density in this point must be very different than that of the virgin crystal. So, in order to test if the changes in density can explain the obtained range, new SRIM simulations were performed using host lattices that included Co (Fe) and N content and changing the total density accordingly. The results obtained by the new simulations considering 1:1 and 2:1 proportions of Al and Co, presented in fig. 6.5, show that the changes in the lattice density have a very important impact in the range of the implanted ions. The results obtained using a 2:1 proportion of Al and Co are close to the profiles obtained by simulation of the RBS spectra indicating that the proportion used is similar to the one obtained at the FWHM of the implantation profile and is a good approximation for the entire implantation region.

The effective fluences, determined by RBS simulation, are presented in table 6.1. The MgO (110) crystal implanted with Co and N exhibits much lower effective fluence for Co than the remaining samples. This sample was implanted at a

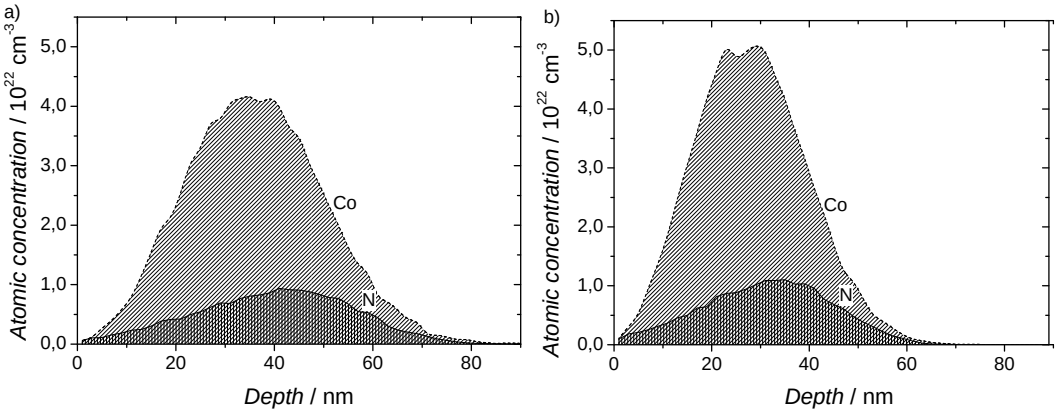

Figure 6.5: Simulation of the implantation profiles of Co and N in Al_2O_3, with energies of 110 keV and 35 keV respectively, using an altered matrix with: a) 2:1 proportion of Al:Co (32% Al 48% O 16% Co 4% N) and b) 1:1 proportion of Al:Co (27,2% Al, 40.8% O, 27.2%Co and 4.8% N).

different time than the other samples and an error during the implantation process cannot be excluded.

Table 6.1: Effective fluences determined by RBS.

Substrate	Co+N		Fe+N	
	Co (10^{17} at.cm^{-2})	N (10^{16} at.cm^{-2})	Fe (10^{17} at.cm^{-2})	N (10^{16} at.cm^{-2})
Al_2O_3 (0001)	2.45	4.64	2.26	4.68
Al_2O_3 (11$\bar{2}$0)	2.26	4.78	2.19	4.68
MgO (100)	2.38	4.77	2.40	5.17
MgO (110)	1.25	4.77	1.85	5.17
TiO_2 (100)	2.05	4.77	1.90	4.86
TiO_2 (110)	2.03	4.77	2.09	5.00

Most of the implanted single crystals show no clear diffraction peaks in the XRD patterns. Exceptions are for the implanted Co+N samples Al_2O_3 (11$\bar{2}$0) and TiO_2 (100) and for Fe+N samples Al_2O_3 (0001), Al_2O_3 (11$\bar{2}$0) and TiO_2 (100) (fig. 6.6 and 6.7). The results obtained for these samples indicate that a mixture of nitride phases (Co+N: Co_4N, Co_3N; Fe+N: Fe_3N, Fe_2N), oxide phases and a spinel structure YX_2O_4 (Y=Al or Ti, X= Co or Fe) coexist. However, the similar magnetic behaviour of all samples indicates that the nitride phases are present in all of them and the fact that they cannot be detected by XRD implies that the

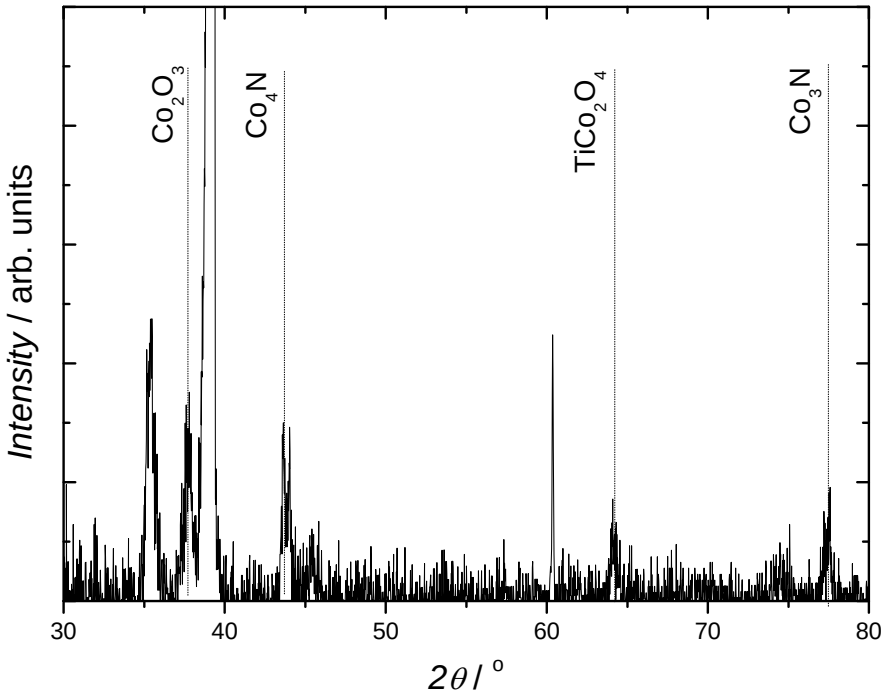

Figure 6.6: X-ray diffractogram of TiO_2 (100) implanted with Co and N in the as implanted state.

particles size is below the resolution of the X-ray diffractometer.

In the as implanted state, all samples except MgO (110) samples are ferromagnetic at room temperature (fig. 6.8) with small saturation magnetic moment of the order of 1 μ_B per Co atom in Co+N implanted samples and 1.2 μ_B per Fe atom in Fe+N implanted samples. The magnetic moment as a function of temperature and as a function of applied magnetic field for implanted MgO (110) is presented in fig. 6.9 and 6.10. The temperature dependence of the magnetic moment indicates that the samples are superparamagnetic with blocking temperature (T_B) around 50 K. To test this behaviour a modified Curie law[1] was fitted to the field cooled (FC) magnetic moment above 50 K. Fig. 6.11 displays χV as a function of $1/T$ showing

[1]The referred Curie law is expressed as

$$\chi V = \frac{\mu_0 \mu_B^2 N P_{ef}^2}{3 k_B T} \tag{6.1}$$

where μ_0 is the magnetic permeability, μ_B is the Bohr magneton, k_B is Boltzmann's constant, T is temperature, N is the number of implanted atoms and P_{ef} is the effective moment

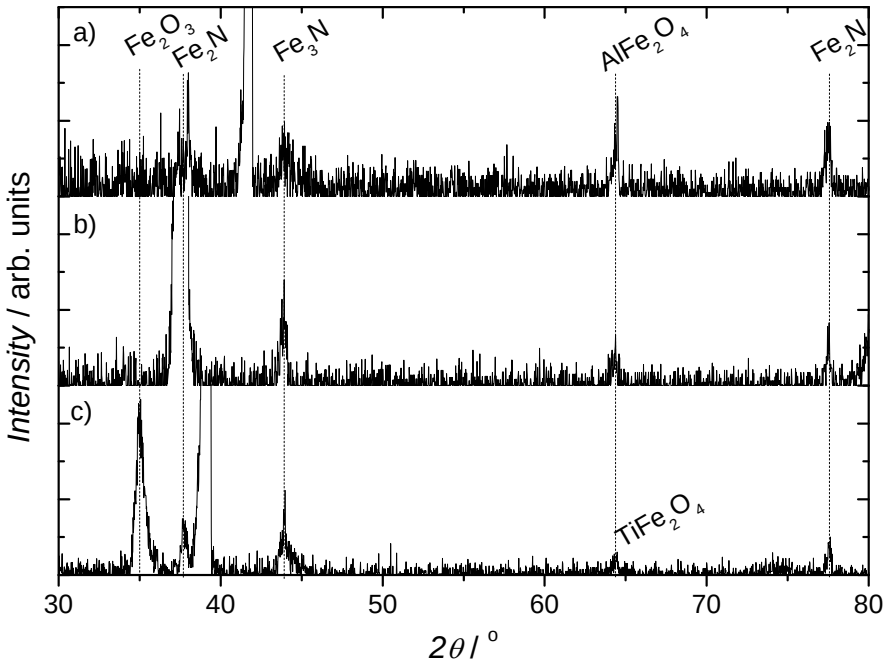

Figure 6.7: X-ray diffractograms of a) Al_2O_3 (0001), b) Al_2O_3 ($11\bar{2}0$) and c) TiO_2 (100) in the as implanted state.

$\chi V \propto 1/T$ gives a good fit for the high temperature region ($T > 50\ K$) yielding $P_{ef} = 13\ \mu_B$ per Co atom for MgO (110) implanted with Co+N. For $T < T_B$ the magnetic aggregates are blocked. The obtained effective moment represents an average moment and cannot be assigned to aggregates of a definite phase since the system may contain a mixture of phases. The same fit was performed for MgO (110) implanted with Fe+N yielding a much higher moment of $P_{ef} = 184\ \mu_B$ per Fe cluster. MgO (100) implanted with Fe+N also seems to exhibit superparamagnetic behaviour, with T_B around 80 K and $P_{ef} = 209\ \mu_B$. However, at room temperature this sample also exhibits a ferromagnetic component.

A summary of the relevant magnetic properties of the implanted samples in the as implanted state is shown in table 6.2.

In order to allow the recovery of the host lattice and rearrangement of the implanted ions the samples underwent a thermal treatment in vacuum at 250^{o}C during 1 hour. RBS analysis shows that the recovery of the oxide crystals is small with the average yield obtained in alignment conditions decreasing from 57 % to

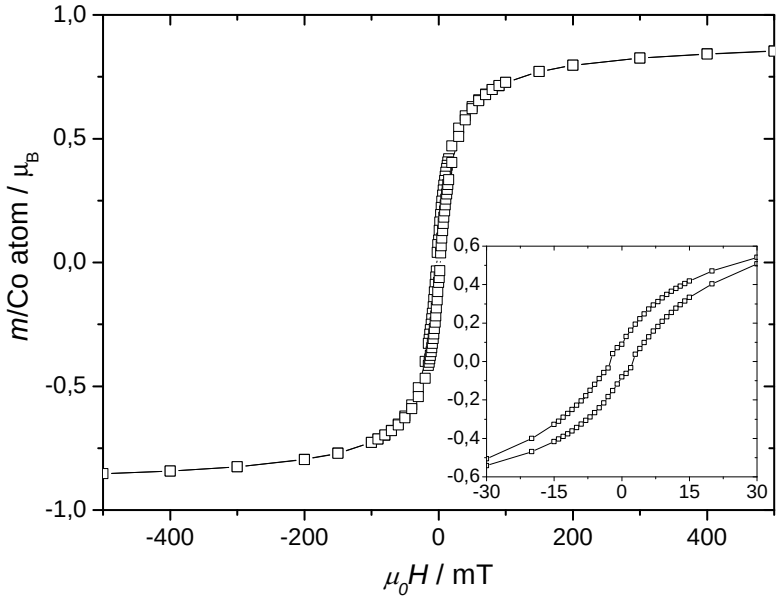

Figure 6.8: Magnetic moment as a function of applied magnetic field of sample Al_2O_3 $(11\bar{2}0)$ implanted with Co and N.

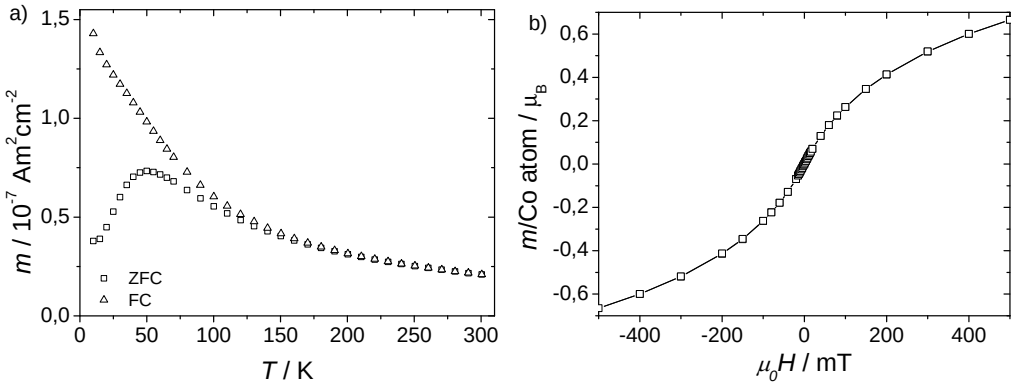

Figure 6.9: Magnetic moment as a function of temperature (a) and as a function of applied magnetic field (b) for sample MgO (110) implanted with Co and N.

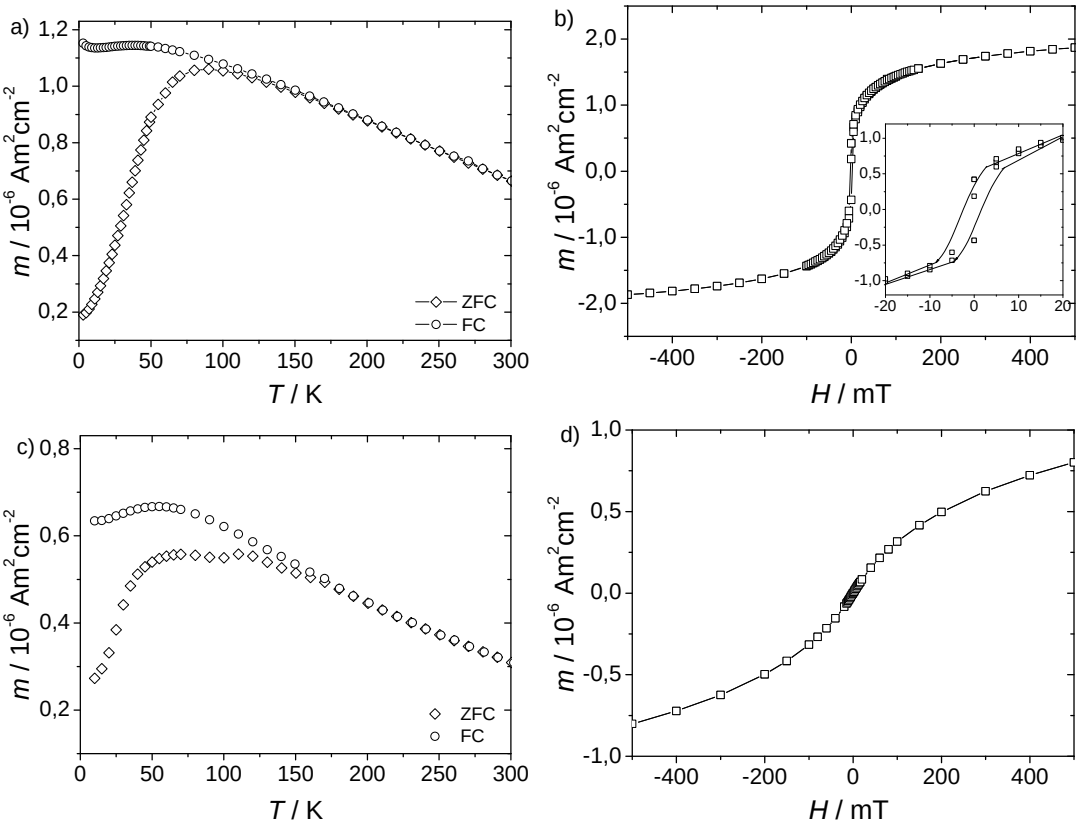

Figure 6.10: Magnetic characterization of MgO (100) and MgO (110) implanted with Fe and N in the as implanted state: a) and c) magnetic moment as a function of temperature with an applied field of 5 mT, b) and d) magnetic moment as a function of applied magnetic field measured at room temperature (300 K).

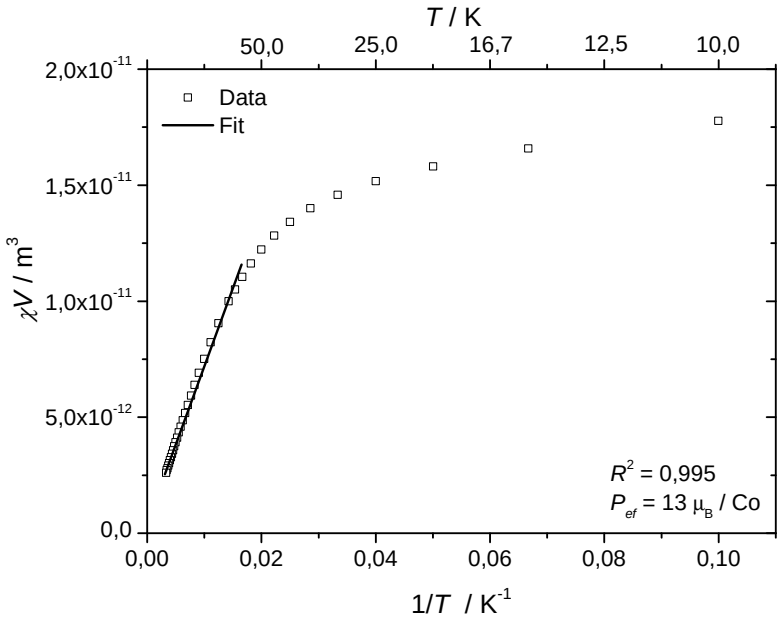

Figure 6.11: χV as a function of $1/T$ for MgO (110) implanted with Co and N in the as implanted state, fitted with a modified Curie law.

Table 6.2: Summary of magnetic properties of implanted oxide crystals in the as implanted state.

Crystal	H_c (mT)	m_s (10^{-6} Am^2/cm^2)	m_s (μ_B/ atom)	T_B (K)
		Co+N		
Al_2O_3 (0001)	4.0	2.27	1.00	-
Al_2O_3 (11$\bar{2}$0)	2.5	1.63	0.78	-
MgO (100)	2.5	2.14	0.97	-
MgO (110)	-	-	-	50
TiO_2 (100)	17.5	1.41	0.74	-
TiO_2 (110)	32.5	2.15	1.14	-
		Fe+N		
Al_2O_3 (0001)	1.5	2.63	1.08	-
Al_2O_3 (11$\bar{2}$0)	0.5	2.24	1.10	-
MgO (100)	2.0	1.95	0.88	80
MgO (110)	-	-	-	50
TiO_2 (100)	2.5	2.55	1.45	-
TiO_2 (110)	7.5	2.95	1.52	-

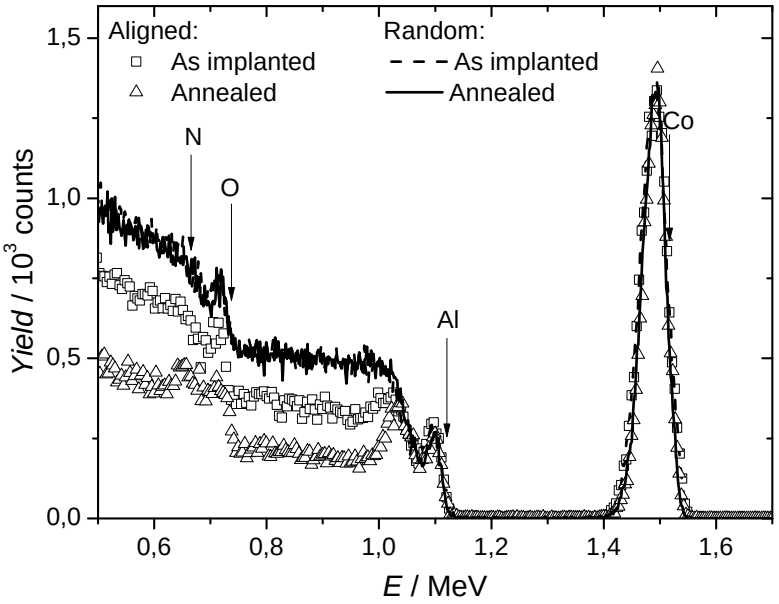

Figure 6.12: RBS spectra of Al_2O_3 $(11\bar{2}0)$ implanted with Co and N in aligned and random conditions for both as implanted and annealed states.

approximately 45 % for Co+N samples (fig. 6.12) and from 54 % to approximately 46 % of the random spectrum for Fe+N samples. On the other hand, simulations of the RBS spectra show no significant modification of the profiles of the implanted species, indicating that the thermal treatment does not induce diffusion of these atoms.

In the case of Co+N implantation, the comparison of the XRD patterns of the as implanted with the ones for annealed crystals only shows differences for Al_2O_3 $(11\bar{2}0)$ crystal. In this crystal two small peaks associated with cobalt oxide (CoO) appear after annealing, indicating the formation or growth of CoO aggregates during annealing (fig. 6.13). Accordingly, a small decrease in saturation magnetic moment is observed for Al_2O_3 $(11\bar{2}0)$ associated with the increase of cobalt oxide. For the remaining Co+N samples no significant changes in magnetic behaviour are observed.

For Fe+N implantation, changes in the relative intensity of diffraction peaks for Al_2O_3 $(11\bar{2}0)$ and TiO_2 (100) diffractograms are observed (fig. 6.14). The spinel phase becomes more important or more crystalline in both samples, as does Fe_2N in TiO_2 (100), because the correspondent diffraction peaks display higher relative

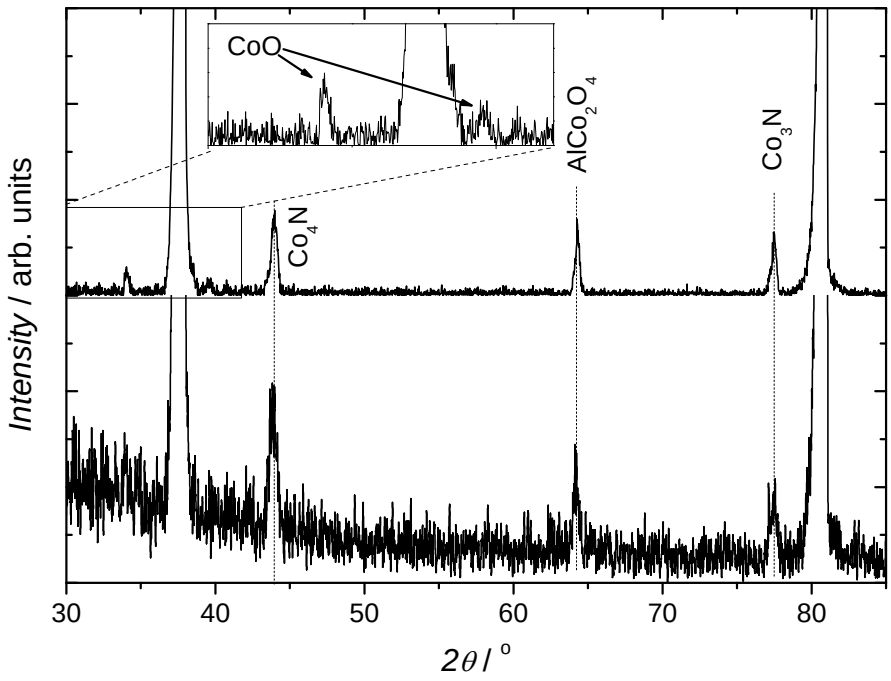

Figure 6.13: X-Ray diffractograms of sample Al_2O_3 $(11\bar{2}0)$ implanted with Co and N in the as implanted (bottom) and annealed (top) states. A zoom of the annealed results is shown to better visualize the presence of CoO diffraction peaks.

intensity, when compared with the diffractograms obtained in the as implanted state. In the magnetic behaviour small changes are only observed for Al_2O_3 (0001), MgO (100) and TiO_2 (100). In the case of Al_2O_3 (0001), a small paramagnetic component appears at room temperature (fig. 6.15). In the case of MgO (100) (not shown) and TiO_2 (100) (fig. 6.15), a decrease in magnetic moment is observed.

The magnetic properties of the implanted samples after annealing are summarized in table 6.3.

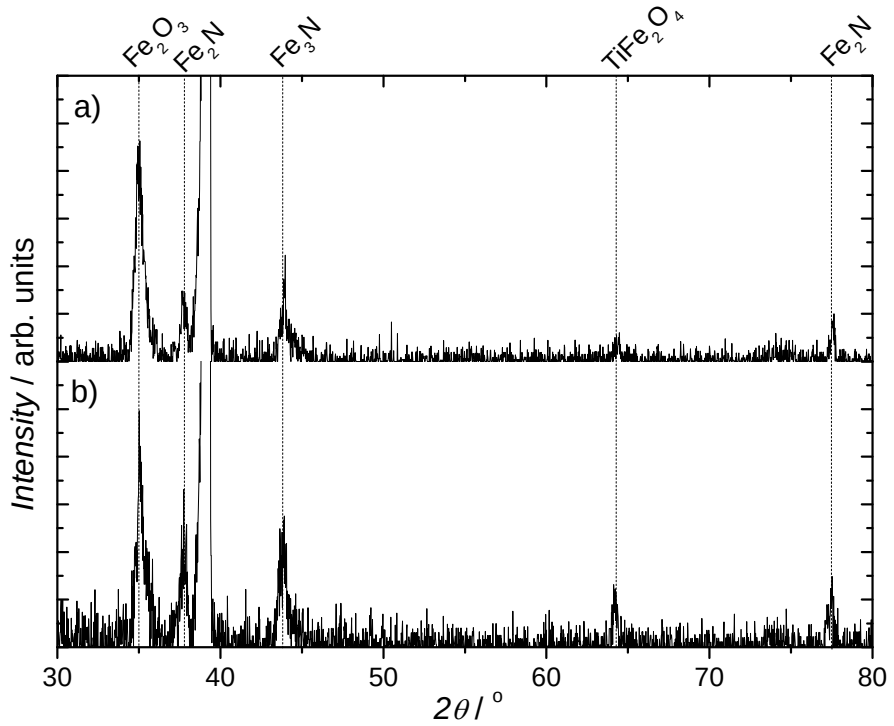

Figure 6.14: XRD diffractograms of TiO_2 (100) implanted with Fe and N in a) as implanted state and b) after annealing.

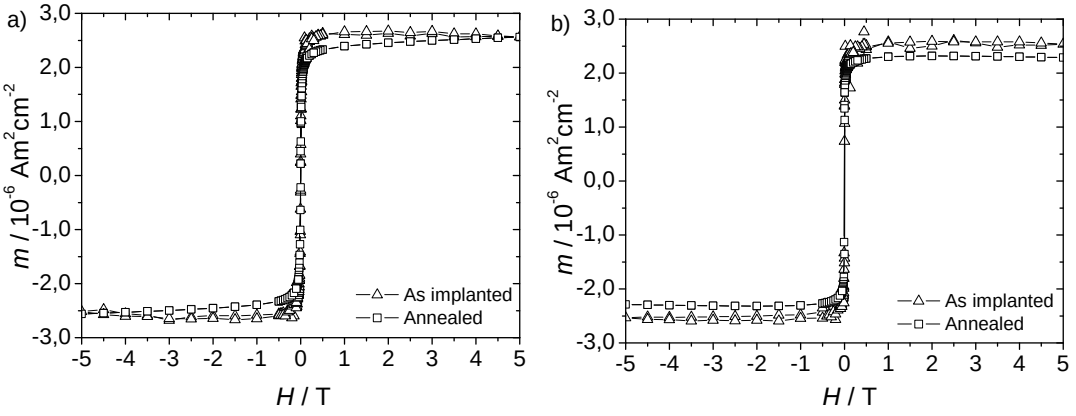

Figure 6.15: Comparison of magnetic moment as a function of applied magnetic field at room temperature in both as implanted and annealed states for samples implanted with Fe+N in a) Al_2O_3 (0001) and b) TiO_2 (100).

Table 6.3: Summary of magnetic properties of oxide crystals implanted with Fe and N in the annealed state.

Crystal	H_c (mT)	m_s (10^{-6} Am^2/cm^2)	m_s (μ_B/ atom)	T_B (K)
		Co+N		
Al_2O_3 (0001)	4.0	2.08	0.87	-
Al_2O_3 (11$\bar{2}$0)	2.0	1.66	0.76	-
MgO (100)	4.0	2.14	0.92	-
MgO (110)	-	-	-	45
TiO_2 (100)	14.0	1.89	0.95	-
TiO_2 (110)	32.5	2.50	1.27	-
		Fe+N		
Al_2O_3 (0001)	1.5	2.34	1.12	-
Al_2O_3 (11$\bar{2}$0)	0.5	2.24	1.10	-
MgO (100)	2.0	2.23	1.00	90
MgO (110)	-	-	-	50
TiO_2 (100)	2.5	2.32	1.32	-
TiO_2 (110)	7.5	2.95	1.52	-

6.4 Main results obtained for implanted single crystals

- A mixture of compounds (nitride, oxide and spinel phases) is obtained after implantation;
- Although all the implantations were performed with a 4:1 ratio between metal and nitrogen fluences, in the case of Fe+N implantation Fe_3N and Fe_2N were the only nitride phases detected. This is explained by iron's affinity to form oxide phases that changes Fe stoichiometry and makes the formation of Fe_4N unlikely;
- Most samples exhibit ferromagnetic behaviour with low magnetic moments (0.75 - 1.2 μ_B per Co in the case of Co+N implantations and 1.0 - 1.5 μ_B per Fe for Fe+N implantations);
- Annealing for 1 hour at 250 ^{o}C in vacuum didn't cause significant changes in the samples' behaviour.

Chapter 7

Conclusions

Iron and cobalt films were successfully produced by reactive magnetron sputtering after determining the appropriate conditions for their deposition.

In the case of both iron and cobalt nitrides, the nitrogen content of the films was shown to increase with the partial pressure of nitrogen in the reactive atmosphere during the production of the films.

The relevant phase for this work is the magnetic cubic phase M_4N (M = Fe, Co) for which the experimental conditions are sputtering of metallic iron or cobalt target in a reactive atmosphere of Ar+N_2 (total pressure = 10 mTorr) with a partial pressure of nitrogen of 10 % into a substrate heated to 250 ^{o}C. For these conditions the composition achieved are 100 % Fe_4N in the case of iron nitide films and 100 % cubic $Co_{4+x}N$ in the case of cobalt nitride films that have structure parameters close to the reported $Co_{16}N$ phase.

For Co-N films, well oriented crystalline films were produced with different orientations depending on the substrate. In the case of te substrate Al_2O_3 (0001) the film surface is parallel to the (111) plane of the cubic nitride, while in the case of substrates MgO (100) and Al_2O_3 ($11\bar{2}0$) the film surface is parallel to the (100) plane of the cubic nitride. The substrate influence is explained by the strain induced due to the mismatch existing between the substrate surface structure and the planes of the cubic $Co_{4+x}N$. A mismatch table (Table 4.5) that allowed to conclude that the less strained films are obtained for Al_2O_3 substrates and the more strained films correspond to the ones deposited on MgO (110) or TiO_2

substrates that cannot be associated with a defined orientation. In both cases, well orientated films or not, the stress in the substrate/film interface induces the magnetic anisotropic behaviour of the film. The significant roughness and low density of the Co-N film indicate that growth occurs by island formation. This leads to mixed orientation in the films on substrates with higher mismatch with Co_4N structure.

In the case of iron nitride films the situation is clearly different since all Fe_4N films exhibit similar orientation (surface parallel to (100) plane of the Fe_4N) independently of the substrate structure and orientation. This implies that the (100) plane has higher stability during growth and that the strain induced by the substrate is not determinant. This is explained by the existence of a mixed composition interface between the substrate and the film due to the high affinity of iron for oxygen and the high concentration of this element in the substrates' composition. This indicates a better coverage of the substrate by the initial layer of the film leading to a growth mechanism closer to layer by layer growth than island growth, in agreement with the low roughness presented by the Fe-N films when compared with the Co-N films.

Although the orientation of the iron nitride films is similar for all substrates, different in-plane magnetic anisotropy is observed depending and following the substrate structural surface anisotropy. This indicates that although strain does not influence the crystalline orientation of the film, the substrate has a determinant influence in the magnetic anisotropy, result explained by strong hybridization in the interface layer, that affects the density in the *d*-band (see section 2.2)

In the case of multilayer samples no clear separation between the individual layers was achieved. This result is attributed to the mobility of nitrogen in iron at the deposition temperature that leads to varying interstitial N content rather than clearly separated Fe/Fe-N layers.

To understand the formation of nitride phases within an oxide matrix, samples were obtained by ion implantation, of the same substrates used for the film preparation, with both nitrogen and iron or cobalt ions. In the as implanted state the implanted region exhibited a mixture of nitride, oxide and spinel phases. The latter phases can be explained by mixed integration of the matrix ions with Fe or Co. Most of the samples exhibit ferromagnetic behaviour with low magnetic mo-

ment of approximately 0.9 μ_B per Co and 1.2 μ_B per Fe on average for each group of samples that doesn't change after annealing treatment at 250 ^{o}C for 1 hour in vacuum. This behaviour is not attributed to ferromagnetic nitrides since only nitrides with high nitrogen content could be detected. To achieve the formation of the magnetic nitrides a higher fluence of Fe and Co relative to that of nitrogen must be used.

Appendix A

Atomic magnetic behaviour

The atomic behaviour in an applied magnetic field is mainly associated with the modifications in the electronic states and in general can be separated in the diamagnetic contribution of the closed shells and the paramagnetic contribution of incomplete shells [28].

The diamagnetic behaviour is associated with the tendency of electrical charges to shield the interior of a material from an applied magnetic field. Classically, this can be viewed as the appearence of an electrical current that opposes the onset of the external magnetic field [29]. The paramagnetic component, on the other hand, is related with the re-orientation of uncompensated intrinsic magnetic moments, originating from the angular momentum and spin of the electrons. The magnetic moment of an atom can be considered as the sum of the electrons magnetic moment associated with its orbital angular momentum and spin

$$\vec{m} = -\frac{e}{2m_e}\sum_{i=1}^{N}\vec{r_i}\times\vec{p_i} - \mu_B g_0 \sum_{i=1}^{N}\vec{s_i} = -\mu_B\vec{L} - \mu_B g_0\vec{S} \tag{A.1}$$

where $\vec{S}$ is the total spin, $\vec{L}$ is the total orbital angular momentum of the atom and g_0 is the electronic g-factor ($g_0 = 2.0023$).

Atoms with electrons in closed shells have total spin and orbital angular momentum zero and, therefore, have no intrinsic atomic magnetic moment. On the other hand, atoms with incomplete electronic shells will possess an associated intrinsic magnetic moment.

The magnetic response of an atom can be determined through the Hamiltonian in an applied magnetic field, which implies replacing the momentum operator $\vec{p}$ by $\vec{p}+e\vec{A}$, where $\vec{A}$ is the vector potential related to $\vec{B}$ by

$$\begin{aligned}\vec{\nabla}\times\vec{A}&=\vec{B}\\ \vec{\nabla}\cdot\vec{A}&=0\end{aligned} \tag{A.2}$$

as well as adding the interaction energy of the field with each electron's spin magnetic moment. Using the symmetric gauge for $\vec{A}$, $\vec{A}=-\frac{1}{2}\vec{r}\times\vec{B}$, the resulting Hamiltonian for an atom with N electrons can then be written as

$$\begin{aligned}\mathcal{H}&=\frac{1}{2m_e}\sum_{i=1}^{N}(\vec{p_i}-\frac{e}{2}\vec{r_i}\times\vec{B})^2+g_0\mu_B\sum_{i=1}^{N}\vec{s_i}\cdot\vec{B}\\ &=\frac{1}{2m_e}\sum_{i=1}^{N}\vec{p_i}^2+\mu_B\vec{L}\cdot\vec{B}+\frac{e^2}{8m_e}B^2\sum_{i=1}^{N}(x_i^2+y_i^2)+g_0\mu_B\vec{S}\cdot\vec{B}\end{aligned} \tag{A.3}$$

assuming $\vec{B}=B\vec{e_z}$ and having $\vec{L}$, the electronic orbital angular momentum, defined as $\hbar\vec{L}=\sum_{i=1}^{N}\vec{r_i}\times\vec{p_i}$, $\vec{S}$, the spin angular momentum, as $\vec{S}=\sum_{i=1}^{N}\vec{s_i}$ and $\mu_B=\frac{e\hbar}{2m_e}$ being the Bohr magneton. The Hamiltonian can then be expressed as

$$\mathcal{H}=\mathcal{H}_0+\Delta\mathcal{H} \tag{A.4}$$

with $\Delta\mathcal{H}$ comprising the field dependent terms of the Hamiltonian. The energy shifts produced by $\Delta\mathcal{H}$ are generally very small on the scale of atomic excitation energies so it is possible to determine the energy levels induced by magnetic field resorting to perturbation theory [27]. Given that the susceptibility is associated with the second derivative of the energy with respect to the field, as shown in (**??**), it is necessary to use terms up to second order in $\vec{B}$ using second-order perturbation theory [80]:

$$E_n\longrightarrow E_n+\Delta E_n\ with\ \Delta E_n=\langle n\,|\Delta\mathcal{H}|\,n\rangle+\sum_{n'\neq n}\frac{|\langle n\,|\Delta\mathcal{H}|\,n'\rangle|^2}{E_n-E_{n'}} \tag{A.5}$$

and so, combining (A.3) and (A.5), ΔE_n can be written as

$$\Delta E_n = \mu_B \vec{B} \cdot \left\langle n \left| \vec{L} + g_0 \vec{S} \right| n \right\rangle + \sum_{n \neq n'} \frac{\left| \left\langle n \left| \mu_B \vec{B} \cdot (\vec{L} + g_0 \vec{S}) \right| n' \right\rangle \right|^2}{E_n - E_{n'}} + \frac{e^2 B^2}{8 m_e} \left\langle n \left| \sum_i (x_i^2 + y_i^2) \right| n \right\rangle \tag{A.6}$$

The simplest application of (A.6) is to an atom (or ion) with all electronic shells closed. In this case, both total orbital angular momentum and total spin are zero in the ground state $|0\rangle$ and consequently only the last term of (A.6) contributes to the ground state field-induced energy shift

$$\Delta E_0 = \frac{e^2 B^2}{8 m_e} \left\langle 0 \left| \sum_i x_i^2 + y_i^2 \right| 0 \right\rangle = \frac{e^2 B^2}{12 m_e} \left\langle 0 \left| \sum_i r_i^2 \right| 0 \right\rangle \tag{A.7}$$

This result is obtained considering the spherical symmetry of the closed-shells.

At the usual temperatures, the probability of the atom being in a state other than its ground state is negligible [27] and so the susceptibility for a solid composed of N atoms is

$$\chi = -\frac{N}{V} \frac{\partial^2 \Delta E_0}{\partial B^2} = -\frac{e^2}{6 m_e} \frac{N}{V} \left\langle 0 \left| \sum_i r_i^2 \right| 0 \right\rangle \tag{A.8}$$

This expression is known as the Larmor diamagnetic susceptibility. This susceptibility is small and independent of both applied field and temperature [28].

To be able to apply (A.6), it is important to determine the ground state of an atom. This can be done using Hund's rules, that allows to determine the ground state quantum numbers L (orbital angular momentum), S (spin angular momentum) and J (total angular momentum), as [81]:

1. S will be the maximum value allowed by the Pauli exclusion principle.

2. L will be the maximum value of total orbital angular momentum consistent with the value of S and the exclusion principle.

3. The value of total angular momentum J is equal to $|L-S|$ if the shell is less than half full ($N < 2l+1$), and will be equal to $L+S$ otherwise.

This ground state is usually represented as ${}^{2S+1}X_J$ where X is a letter associated to the value of L.

For $J \neq 0$, *i.e.* atoms with incomplete shells, the first term of (A.6) will be dominant and the remaining terms can almost always be safely ignored. In this situation, the ground state presents $(2J+1)$ degeneracy in zero field and it is necessary to determine the contribution of the $2J+1$ states evaluating and diagonalizing the $(2J+1)$-dimensional square matrix

$$\langle JLSJ_z \left| J_z + g_0 S_z \right| JLSJ'_z \rangle \quad with \quad J_z, J'_z = -J, \cdots, J \tag{A.9}$$

The particular case of shells one electron short of being half filled will lead to Van-Vleck paramagnetism.

This problem is made much simpler by introducing the Wigner-Eckart theorem which states that the matrix elements of any vector operator in the $(2J+1)$-dimensional space of eigenstates of J^2 and J_z, with a given value of J, are proportional to the matrix elements of J itself [27]:

$$\left\langle JLSJ_z \left| \vec{L} + g_0 \vec{S} \right| JLSJ'_z \right\rangle = g(JLS) \left\langle JLSJ_z \left| \vec{J} \right| JLSJ'_z \right\rangle \tag{A.10}$$

In this result, the proportionality constant $g(JLS)$ is independent of the values of both J_z and J'_z. Since the matrix elements of J_z are given by

$$\langle JLSJ_z \left| J_z \right| JLSJ'_z \rangle = J_z \delta_{J_z, J'_z} \tag{A.11}$$

it follows that

$$\langle JLSJ_z \left| L_z + g_0 S_z \right| JLSJ'_z \rangle = g(JLS) J_z \delta_{J_z, J'_z} \tag{A.12}$$

The matrix is therefore already diagonal in the states of definite J_z with $g(JLS)$, know as the Landé g-factor, defined as

$$g(JLS) = \frac{3}{2} + \frac{1}{2}\left[\frac{S(S+1) - L(L+1)}{J(J+1)}\right] \tag{A.13}$$

taking the electron g-factor g_0 to be exactly 2. The (2J+1)-fold degenerate ground state is then split into states with definite J_z whose energies are uniformly separated by $g(JLS)\mu_B B$.

Since the Helmholtz free energy, F, is defined as [27]

$$e^{-F/k_BT} = \sum_n e^{-E_n(B)/k_BT} \tag{A.14}$$

if only the $2J+1$ lowest states are thermally excited with appreciable probability, F is then given by

$$e^{-\beta F} = \sum_{J_z=-J}^{J} e^{-\beta\gamma B J_z} \tag{A.15}$$

with $\gamma = g(JLS)\mu_B$ and $\beta = 1/k_BT$. The geometric series in (A.15) yields

$$e^{-\beta F} = \frac{e^{\beta\gamma B(J+1/2)} - e^{-\beta\gamma B(J+1/2)}}{e^{\beta\gamma B/2} - e^{-\beta\gamma B/2}} \tag{A.16}$$

The magnetization M of N such atoms in a volume V is then

$$M = -\frac{N}{V}\frac{\partial F}{\partial B} = \frac{N}{V}\gamma J B_J(x) \tag{A.17}$$

with $x = \beta\gamma JB$ and the Brillouin function $B_J(x)$ (represented in fig. A.1) being defined as

$$B_J(x) = \frac{2J+1}{2J}\coth\frac{(2J+1)x}{2J} - \frac{1}{2J}\coth\frac{x}{2J} \tag{A.18}$$

As can be seen in fig. A.1, in the low temperature limit ($k_BT \ll \gamma JB \Rightarrow x \gg 1$) the magnetization will tend to $N/Vg(JLS)\mu_B J$, *i.e.* each atom is completely aligned by the field and saturation is reached. If, on the other hand, temperature is high, then $x \ll 1$ and the Brillouin function can be simplified as follows:

$$\coth x \approx \frac{1}{x} + \frac{1}{3}x \quad \Rightarrow \quad B_J(x) = \frac{J+1}{3J}x \tag{A.19}$$

The magnetic susceptibility is then

$$\chi = \frac{\partial M}{\partial B} = \frac{N}{V}\frac{(g(JLS)\mu_B)^2}{3k_BT}J(J+1) = \frac{C}{T} \tag{A.20}$$

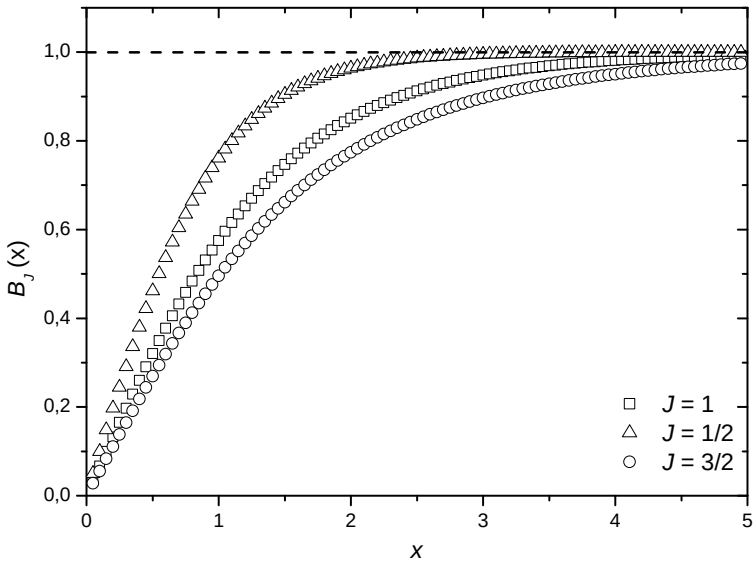

Figure A.1: Brillouin function for different values of J.

The variation of susceptibility inversely with temperature observed in (A.20) is known as Curie's law.

Appendix B

Exchange interactions between localized electrons

To describe the exchange interaction between localized electrons, let us consider the hydrogen molecule (fig. B.1), in which we have two separate atoms bound together by two indistinguishable electrons (labeled 1 and 2). To show how the Pauli principle can lead to magnetic effects when there are no spin terms in the Hamiltonian, we shall consider the spin-independent Hamiltonian [27]. In this case, the Hamiltonian can be split into three parts:

$$\mathcal{H} = \mathcal{H}_1 + \mathcal{H}_2 + \mathcal{H}_{1,2} \tag{B.1}$$

where $\mathcal{H}_1$ and $\mathcal{H}_2$ are the Hamiltonian operators expressed in terms of the coordinates of electrons 1 and 2, respectively, and $\mathcal{H}_{1,2}$ describes the interaction between the electrons arising from the overlap of the electron wave functions. In the Heitler-London approach, the tight-binding model is used, and the three components of the Hamiltonian can be defined as

$$\begin{aligned}
\mathcal{H}_1 &= -\frac{\hbar^2}{2m_e}\nabla_1^2 - \frac{1}{4\pi\epsilon_0}\frac{e^2}{r_{A1}} \\
\mathcal{H}_2 &= -\frac{\hbar^2}{2m_e}\nabla_2^2 - \frac{1}{4\pi\epsilon_0}\frac{e^2}{r_{B2}} \\
\mathcal{H}_{1,2} &= -\frac{1}{4\pi\epsilon_0}\left(\frac{e^2}{r_{B1}} + \frac{e^2}{r_{A2}} - \frac{e^2}{r_{12}}\right)
\end{aligned} \tag{B.2}$$

Figure B.1: Schematic representation of the H_2 molecule.

State	S	S_Z	
$\frac{1}{\sqrt{2}}(\|\uparrow\downarrow\rangle - \|\downarrow\uparrow\rangle)$	0	0	Singlet State
$\|\uparrow\uparrow\rangle$	1	1	Triplet State
$\frac{1}{\sqrt{2}}(\|\uparrow\downarrow\rangle + \|\downarrow\uparrow\rangle)$	1	0	
$\|\downarrow\downarrow\rangle$	1	-1	

Table B.1: Linear combination of spin states for the spin-wave function and their respective values of S and S_z

.

Since the Hamiltonian does not depend on spin, the wave function of the two electrons can be written as

$$\Psi(1,2) = \Phi(\vec{r_1}, \vec{r_2}) X(\vec{S_1}, \vec{S_2}) \tag{B.3}$$

where $\Phi(\vec{r_1}, \vec{r_2})$ corresponds to the spatial component and with $X(\vec{S_1}, \vec{S_2})$, which comprises the orbital component of the wave function, being any linear combination of the four spin states $(|\uparrow\uparrow\rangle, |\uparrow\downarrow\rangle, |\downarrow\uparrow\rangle, |\downarrow\downarrow\rangle)$. We can choose the linear combinations of these states to have definite values of S and S_z, the total spin and its component along an axis, respectively. The appropriate linear combinations are presented in table B.1.

According to the Pauli principle, the wave function in (B.3) should be antisymmetric, *i.e.* $\Psi(1,2) = -\Psi(2,1)$, and therefore if Φ is symmetric then X must be antisymmetric, and vice-versa. According to table B.1, the antisymmetric spin wave function corresponds to the singlet state ($S = 0$), while the symmetric spin wave function is associated with the triplet state ($S = 1$). The energy difference between singlet and triplet states (E_s and E_t) measures the extent to which

an antiparallel alignment ($S = 0$) is more favorable than the parallel alignment ($S = 1$).

The spatial part of the wave function is given by

$$\begin{aligned} \Phi_s(r_1, r_2) &= \frac{1}{\sqrt{2}} \left(\Phi_A(r_1)\Phi_B(r_2) + \Phi_A(r_2)\Phi_B(r_1)\right) \\ \Phi_t(r_1, r_2) &= \frac{1}{\sqrt{2}} \left(\Phi_A(r_1)\Phi_B(r_2) - \Phi_A(r_2)\Phi_B(r_1)\right) \end{aligned} \tag{B.4}$$

Φ_s, being symmetric is therefore associated with the singlet state ($S = 0$), which has an antisymmetric spin wave function, while Φ_t corresponds to the triplet state ($S = 1$). The energy of each state can then be determined to be

$$E = \iint \Phi^* \mathcal{H} \Phi d^3 r_1 d^3 r_2 \Rightarrow E = E_A + E_B + Q \pm J \tag{B.5}$$

with the sign, + or −, being associated with Φ_s and Φ_t respectively, E_A and E_B being the energies of the electrons in their respective atoms disregarding interaction, Q being the Coulomb term given by

$$Q = \iint \Phi_A^*(r_1)\Phi_B^*(r_2)\mathcal{H}_{1,2}\Phi_A(r_1)\Phi_B(r_2) d^3 r_1 d^3 r_2 \tag{B.6}$$

and J, denoted exchange integral, associated with the interaction arising from the overlap of the wave functions is given by

$$J = \iint \Phi_A^*(r_1)\Phi_B^*(r_2)\mathcal{H}_{1,2}\Phi_A(r_2)\Phi_B(r_1) d^3 r_1 d^3 r_2 \tag{B.7}$$

The energy difference between both states, singlet and triplet, is then simply

$$E_s - E_t = 2J \tag{B.8}$$

The interatomic exchange, J, can be either positive or negative which will cause the alignment to be parallel or antiparallel. In the particular case of the hydrogen molecule $J < 0$ and so the electron spins tend to be aligned antiparallel to each other.

Appendix C

Refurbishing of Reactive Sputtering System

In the course of this project refurbishing of an out of order deposition system present at Campus Tecnológico e Nuclear - Instituto Superior Técnico was carried out.

The main problem of the system in question was in the cluster gun, which consists of three magnetrons, where one of the magnetrons due most likely to overheating and improper use of the water cooling system was cracked making it impossible to achieve vacuum in the deposition chamber. Also, the damage to the body of the magnetron allowed for water of the cooling system to enter the magnet system leaving the magnets completely corroded and destroyed.

Another problem of this system was the pressure sensors which were faulty and giving readings of good vacuum conditions even with a whole in the body of the magnetron. In order to fix the problems observed a new magnetron and new pressure sensors were installed in the system allowing it work with magnetic targets and correctly gauge the pressure inside the chamber.

The system was then further improved through the introduction of a gate valve between the main chamber and the main pump to prevent polluting the chamber during the initial heating of the pump. A secondary gas line was also introduced to allow for reactive sputter depositions with mixtures of $Ar+O_2$ or $Ar+N_2$, the flow of each gas being controlled through needle valves. Lastly, a

Figure C.1: Deposition system at Campus Tecnológico e Nuclear - Instituto Superior Técnico

heating element, courtesy of prof. Ribeiro da Silva (Centro de Física Nuclear da Universidade de Lisboa), was introduced to perform high temperature depositions. X-ray diffractograms of Ni films deposited on glass (fig. C.2) at room temperature and at 250° C show the importance of having the possibility to perform depositions at high temperature, due to its effects on the film's structure.

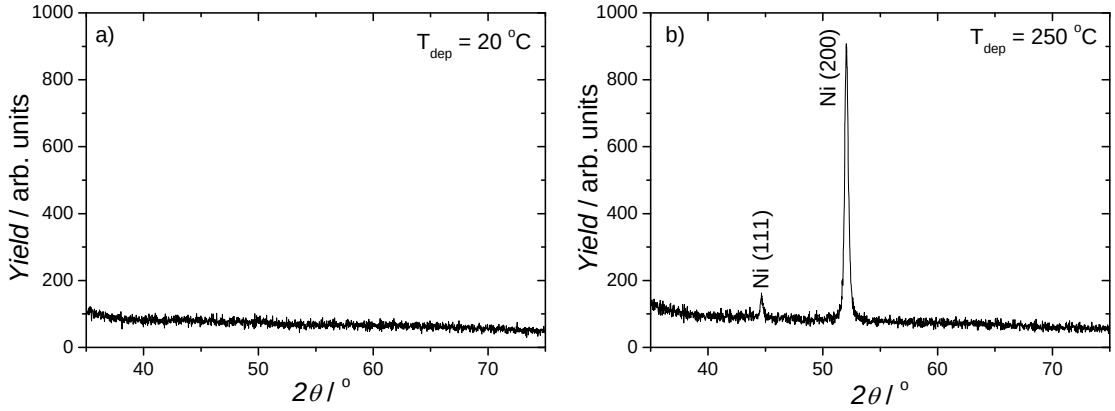

Figure C.2: X-ray diffractograms of Ni thin films deposited a) at room temperature and b) at high temperature (250° C).

List of Figures

List of Tables

Bibliography

[1] K.H. Jack. Binary and ternary interstitial alloys. i. the iron-nitrogen system: The structures of Fe_4N and Fe_2N. *Proceedings of the Royal Society of London A: Mathematical, Physical and Engineering Sciences*, 195(1040):34–40, 1948. 1, 81

[2] A. Tasaki, K. Tagawa, E. Kita, S. Harada, and T. Kusunose. Recording tapes using iron nitride fine powder. *Magnetics, IEEE Transactions on*, 17(6):3026–3028, 1981. 1, 81, 82, 89

[3] T. Takahashi, N. Takahashi, N. Tamura, T. Nakamura, M. Yoshioka, W. Inami, and Y. Kawata. Growth of Fe_4N epitaxial layers displaying anomalous light reflectivity modulated by an external magnetic field. *Journal of Materials Chemistry*, 11:3154–3157, 2001. 1, 3, 81

[4] M. Beshkova, G. Beshkov, M. Marinov, D. Bogdanov-Dimitrov, G. Mladenov, T. Tanaka, and K. Kawabata. Rapid thermal annealing of Co_xN. *Materials and Manufacturing Processes*, 16(4):531–540, 2001. 1

[5] G. Rahman and I.G. Kim. Magnetic properties of anti-perovskite tetracobalt-nitride surfaces: a first-principles study. *Journal of the Korean Physical Society*, 54(1):145–151, 2009. 1, 2

[6] M. Matsuoka and K. Ono. Crystal structure of sputter-synthesized CoN_x thin films. *Applied Physics Letters*, 49(24):1644–1646, 1986. 1, 3, 53

[7] K. Oda, T. Yoshio, and K. Oda. Preparation of Co-N films by rf-sputtering. *Journal of Materials Science*, 22(8):2729–2733, 1987. 1, 2, 53, 67

[8] X. Wang, H. Jia, W.T. Zheng, Y. Chen, and S. Feng. Structural and magnetic properties of Co-N thin films synthesized by direct current magnetron sputtering. *Thin Solid Films*, 517(15):4419 – 4424, 2009. 1, 2, 58

[9] Y.F. Chen, E.Y. Jiang, Z.Q. Li, W.B. Mi, P. Wu, and H.L. Bai. Structure and magnetic properties of rf sputtered FeN films. *Journal of Physics D: Applied Physics*, 37(10):1429 – 1433, 2004. 1, 81

[10] Y. Utsushikawa and K. Niizuma. The saturation magnetization of Fe-N films prepared by nitriding treatment in N_2 plasma. *Journal of Alloys and Compounds*, 222(1-2):188 – 192, 1995. 2, 81

[11] D.M. Borsa, S. Grachev, D.O. Boerma, and J.W.J. Kerssemakers. High-quality epitaxial iron nitride films grown by gas-assisted molecular-beam epitaxy. *Applied Physics Letters*, 79(7):994–996, 2001. 2, 107

[12] R. Coehoorn, G.H.O. Daalderop, and H.J.F. Jansen. Full-potential calculations of the magnetization of $Fe_{16}N_2$ and Fe_4n. *Physical Review B*, 48:3830–3834, 1993. 2, 81, 82

[13] A. Sakuma. Self-consistent calculations for the electronic structures of iron nitrides, Fe_3N, Fe_4N and $Fe_{16}N_2$. *Journal of Magnetism and Magnetic Materials*, 102(1-2):127 – 134, 1991. 2, 82, 83, 153

[14] B.C. Frazer. Magnetic structure of Fe_4N. *Physical Review*, 112:751–754, 1958. 2, 82

[15] S.F. Matar, A. Houari, and M.A. Belkhir. *Ab initio* studies of magnetic properties of cobalt and tetracobalt nitride Co_4N. *Physical Review B*, 75:245109, 2007. 2, 4, 67, 149

[16] S.F. Matar. Chemical bonding and magnetic trends within the iron-nitrogen system. *Journal of Alloys and Compounds*, 345(1 - 2):72 – 76, 2002. 2, 4, 149

[17] A. Houari, S.F. Matar, and M.A. Belkhir. DFT study of magneto-volume effects in iron and cobalt nitrides. *Journal of Magnetism and Magnetic Materials*, 322(6):658 – 660, 2010. 2, 58

[18] T. Koyano, T. Nomiyama, N. Kanoh, H. Numata, T. Ohba, E. Kita, and H. Ohtsuka. Magnetization of α' iron nitride produced through the fcc $\rightarrow$ bct martensitic transformation in high magnetic field. *Journal of Applied Physics*, 100(3):033906, 2006. 2, 83

[19] Y. Takahashi, Y. Imai, and T. Kumagai. Spin-polarized electronic band structures of the Fe_4N-Co_4N system. *Journal of Magnetism and Magnetic Materials*, 323(23):2941 – 2944, 2011. 2

[20] Y. Imai, Y. Takahashi, and T. Kumagai. Relations of electronic energies and magnetic moments of tetra-3d metal (Mn, Fe, Co and Ni) nitrides calculated using a plane-wave basis method. *Journal of Magnetism and Magnetic Materials*, 322(18):2665 – 2669, 2010. 2

[21] A. Narahara, K. Ito, T. Suemasu, Y.K. Takahashi, A. Ranajikanth, and K. Hono. Spin polarization of Fe_4N thin films determined by point-contact Andreev reflection. *Applied Physics Letters*, 94(20):202502, 2009. 2

[22] K. Sunaga, M. Tsunoda, K. Komagaki, Y. Uehara, and M. Takahashi. Inverse tunnel magnetoresistance in magnetic tunnel junctions with an Fe_4N electrode. *Journal of Applied Physics*, 102(1):013917, 2007. 3

[23] M. Matsuoka, K. Ono, and T. Inukai. Magnetic properties of cobalt nitride thin films. *Applied Physics Letters*, 49(15):977–979, 1986. 3

[24] M. Matsuoka, K. Ono, and T. Inukai. Perpendicular magnetic anisotropy of reactively sputtered cobalt nitride thin films. *Magnetics, IEEE Transactions on*, 23(5):2788–2790, 1987. 3

[25] Z. Yao, A. Zhu, J. Chen, X. Wang, C.T. Au, and C. Shi. Synthesis, characterization and activity of alumina-supported cobalt nitride for NO decomposition. *Journal of Solid State Chemistry*, 180(9):2635 – 2640, 2007. 3

[26] M.B. Lourenço, M.D. Carvalho, P. Fonseca, T. Gasche, G. Evans, M. Godinho, and M.M. Cruz. Stability and magnetic properties of cobalt nitrides. *Journal of Alloys and Compounds*, 612(0):176 – 182, 2014. 3, 53, 67, 68, 74

[27] N.W. Ashcroft and N.D. Mermin. *Solid State Physics*. Harcourt College Publishers, 1976. 8, 15, 16, 136, 137, 138, 139, 141

[28] H.P. Myers. *Introductory Solid State Physics*. CRC Press, 1997. 9, 10, 11, 14, 43, 135, 137

[29] H. Ibach and H. Lüth. *Solid-State Physics - An Introduction to Principles of Materials Science*. Springer Berlin Heidelberg, 2003. 12, 135, 149

[30] J.F. Janak. Uniform susceptibilities of metallic elements. *Physical Review B*, 16(1):255, 1977. 13, 149

[31] B.D. Cullity and C.D. Graham. *Introduction to Magnetic Materials*. Wiley, 2009. 14, 15, 18, 19, 21, 23, 24, 149, 150

[32] S. Blundell. *Magnetism in Condensed Matter*. Oxford University Press, 2001. 15, 16

[33] P. Poulopoulos and K. Baberschke. Magnetism in thin films. *Journal of Physics: Condensed Matter*, 11:9495–9515, 1999. 21, 24, 25

[34] J.A. Osborn. Demagnetizing factors of the general ellipsoid. *Physical Review*, 67:351–357, 1945. 22

[35] L. Néel. Anisotropie magnétique superficielle et surstructures d'orientation. *Journal de Physique et Le Radium*, 15(4):225–239, 1954. 24

[36] U. Gradmann. Surface magnetism. *Journal of Magnetism and Magnetic Materials*, 100(1 - 3):481 – 496, 1991. 24

[37] D. Depla, S. Mahieu, and J.E. Greene. Chapter 5 - Sputter deposition processes. In Peter M. Martin, editor, *Handbook of Deposition Technologies for Films and Coatings (Third Edition)*, pages 253 – 296. William Andrew Publishing, third edition edition, 2010. 27

[38] R.D Arnell and P.J Kelly. Recent advances in magnetron sputtering. *Surface and Coatings Technology*, 112(1 - 3):170 – 176, 1999. 27

[39] I. Safi. Recent aspects concerning DC reactive magnetron sputtering of thin films: a review. *Surface and Coatings Technology*, 127(2 - 3):203 – 218, 2000. 27

[40] P.J. Kelly and R.D. Arnell. Magnetron sputtering: a review of recent developments and applications. *Vacuum*, 56:159–172, 2000. 28, 29, 150

[41] W.D. Sproul, D.J. Christie, and D.C. Carter. Control of reactive sputtering processes. *Thin Solid Films*, 491(1 - 2):1 – 17, 2005. 29, 30, 150

[42] S. Berg and T. Nyberg. Fundamental understanding and modeling of reactive sputtering processes. *Thin Solid Films*, 476(2):215 – 230, 2005. 29

[43] S. Schiller, U. Heisig, K. Steinfelder, J. Strümpfel, R. Voigt, R. Fendler, and G. Teschner. On the investigation of d.c. plasmatron discharges by optical emission spectrometry. *Thin Solid Films*, 96(3):235 – 240, 1982. 30

[44] W.D. Sproul and J. Tomashek. Rapid rate reactive sputtering of a group IVB metal. U.S. Patent 4.428.811, 1984. 30

[45] J. Affinito and R.R. Parsons. Mechanisms of voltage controlled, reactive, planar magnetron sputtering of Al in Ar/N_2 and Ar/O_2 atmospheres. *Journal of Vacuum Science & Technology A*, 2(3):1275–1284, 1984. 30

[46] M. McElfresh. *Fundamentals of magnetism and magnetic measurements featuring quantum design's magnetic property measurement system.* Quantum Design, 1994. 32, 33, 150

[47] P. Atkins and J. de Paula. *Atkins' Physical Chemistry.* Oxford, 8th ed. edition, 2006. 34, 150

[48] Y. Wang and M. Nastasi, editors. *Handbook of modern ion beam materials analysis.* Materials Research Society, 2nd ed. edition, 2009. 34, 35

[49] M. Mayer. Rutherford backscattering spectrometry (RBS). In *Workshop on Nuclear Data for Science and Technology: Materials Analysis*, 2003. 34

[50] J.M. Walls, editor. *Methods of Surface Analysis: Techniques and Applications*. Cambridge University Press, 1989. 37, 38

[51] M. Thompson. RUMP: Rutherford backscattering spectrometry analysis package. http://www.genplot.com. 39

[52] J. Als-Nielsen and D. McMorrow. *Elements of modern X-ray Physics*. Wiley, 2nd ed. edition, 2011. 44, 151

[53] E. Meyer. Atomic force microscopy. *Progress in Surface Science*, 41(1):3 – 49, 1992. 45

[54] J.J. Rehr and R.C. Albers. Theoretical approaches to X-ray absorption fine structure. *Reviews of Modern Physics*, 72(3):621 – 654, 2000. 49

[55] V. Holý, J. Kuběna, I. Ohlídal, K. Lischka, and W. Plotz. X-ray reflection from rough layered systems. *Physical Review B*, 47(23):15897 – 15903, 1993. 49

[56] M. Yasaka. X-ray thin-film measurement techniques. *The Rigaku Journal*, 26(2):1–9, 2010. 49, 50, 51, 151

[57] J.-S. Fang, L.-C. Yang, C.-S. Hsu, G.-S. Chen, Y.-W. Lin, and G.-S. Chen. Phase transition behavior of reactive sputtering deposited Co-N thin films using transmission electron microscopy. *Journal of Vacuum Science & Technology A*, 22(3):698–704, 2004. 53

[58] C. Silva, A. Vovk, R.C. da Silva, P. Strichovanec, P.A. Algarabel, A.P. Gonçalves, R.P. Borges, M. Godinho, and M.M. Cruz. Magnetic properties of Co-N thin films deposited by reactive sputtering. *Thin Solid Films*, 556(0):125, 2014. 54, 55, 67, 71

[59] C. Silva, A. Vovk, R.C. da Silva, P. Strichonavec, P.A. Algarabel, A. Casaca, C. Meneghini, I. Carlomagno, M. Godinho, and M.M. Cruz. Influence of the substrate on structure and magnetic properties of Co-N thin films. *Journal of Alloys and Compounds*, 633:470 – 478, 2015. 54, 59

[60] L.R. Doolittle. Algorithms for the rapid simulation of rutherford backscattering spectra. *Nuclear Instruments and Methods in Physics Research Section B: Beam Interactions with Materials and Atoms*, 9(3):344 – 351, 1985. 55

[61] E.P. Wohlfarth, editor. *Ferromagnetic materials Vol. 1*. North-Holland, 1986. 58

[62] K.K. Shih and J. Karasinski. Properties of Co-N, Co-Fe-N, and Co-Zr-N films prepared by rf sputtering in nitrogen-argon gas mixtures. *Journal of Applied Physics*, 73(12):8377–8380, 1993. 59

[63] R. Torchio, C. Meneghini, S. Mobilio, G. Capellini, A. Garcia Prieto, J. Alonso, M.L. Fdez-Gubieda, V. Turco Liveri, A. Longo, A.M. Ruggirello, and T. Neisius. Microstructure and magnetic properties of colloidal cobalt nano-clusters. *Journal of Magnetism and Magnetic Materials*, 322(21):3565 – 3571, 2010. 63, 64, 152

[64] C. Meneghini, F. Bardelli, and S. Mobilio. ESTRA-FitEXA: A software package for EXAFS data analysis. *Nuclear Instruments and Methods in Physics Research Section B: Beam Interactions with Materials and Atoms*, 285(0):153 – 157, 2012. 65

[65] C. Battocchio, C. Meneghini, I. Fratoddi, I. Venditti, M. Russo, G. Aquilanti, C. Maurizio, F. Bondino, R. Matassa, M. Rossi, S. Mobilio, and G. Polzonetti. Silver nanoparticles stabilized with thiols: A close look at the local chemistry and chemical structure. *The Journal of Physical Chemistry C*, 116(36):19571–19578, 2012. 67

[66] K. Ito, K. Harada, K. Toko, H. Akinaga, and T. Suemasu. Epitaxial growth and magnetic characterization of ferromagnetic Co_4N thin films on $SrTiO_3(001)$ substrates by molecular beam epitaxy. *Journal of Crystal Growth*, 336(1):40 – 43, 2011. 68

[67] D. K. Schroder. *Semiconductor Material and Device Characterization*. Wiley-Interscience, 2006. 76

[68] W. Gil, D. Görlitz, M. Horisberger, and J. Kötzler. Magnetoresistance anisotropy of polycrystalline cobalt films: Geometrical-size and domain effects. *Physical Review B*, 72:134401, 2005. 76

[69] A. Segal, O. Shaya, M. Karpovski, and A. Gerber. Asymmetric field dependence of magnetoresistance in magnetic films. *Physical Review B*, 79:144434, 2009. 79

[70] X.M. Cheng, S. Urazhdin, O. Tchernyshyov, C.L. Chien, V.I. Nikitenko, A.J. Shapiro, and R.D. Shull. Antisymmetric magnetoresistance in magnetic multilayers with perpendicular anisotropy. *Physical Review Letters*, 94:017203, 2005. 79

[71] Y. Sugita, H. Takahashi, M. Komuro, K. Mitsuoka, and A. Sakuma. Magnetic and Mössbauer studies of single-crystal $Fe_{16}N_2$ and Fe-N martensite films epitaxially grown by molecular beam epitaxy (invited). *Journal of Applied Physics*, 76(10):6637–6641, 1994. 81

[72] M. Takahashi, H. Shoji, H. Takahashi, H. Nashi, T. Wakiyama, M. Doi, and M. Matsui. Magnetic moment of α"-$Fe_{16}N_2$ films (invited). *Journal of Applied Physics*, 76(10):6642–6647, 1994. 81

[73] X.-z. Ding, F.-m. Zhang, J.-s. Yan, H.-l. Shen, X. Wang, X.-h. Liu, and D.-F. Shen. Synthesis and magnetic properties of iron nitride films deposited on Ge(100) by reactive ion beam sputtering. *Journal of Applied Physics*, 82(10):5154–5158, 1997. 81

[74] M.A. Abdellateef, C. Heiden, H. Lemke, F.M. El-Hossary, and K. Baerner. Magnetic properties and structure of the α"-$Fe_{16}n_2$ films. *Journal of Magnetism and Magnetic Materials*, 256(1-3):214 – 220, 2003. 81

[75] H.Y. Wang, S. Mitani, M. Motokawa, and H. Fujimori. Effect of high magnetic fields on the morphology of soft magnetic α'-FeN films. *Journal of Applied Physics*, 93(11):9145–9150, 2003. 81

[76] W. Kiriake, K. Kuwahara, H. Iwanaga, and H. Fujiyama. Preparation of iron nitride thin films by magnetron sputtering under surface magnetic field on

substrates. *Surface and Coatings Technology*, 98(1-3):1293 – 1297, 1998. 82, 153

[77] T. Yamaguchi, M. Sakita, M. Nakamura, and T. Kobira. Synthesis and characteristics of Fe_4N powders and thin films. *Journal of Magnetism and Magnetic Materials*, 215-216:529 – 531, 2000. 107

[78] B. Rauschenbach, A. Kolitsch, and K. Hohmuth. Iron nitride phases formed by nitrogen ion implantation and thermal treatment. *physica status solidi (a)*, 80(2):471–482, 1983. 115

[79] K. Nakajima, S. Okamoto, and T. Okada. Formation of ferromagnetic iron nitrides in iron thin films by high-dose nitrogen ion implantation. *Journal of Applied Physics*, 65(11):4357–4361, 1989. 115

[80] D. Park. *Introduction to Quantum Theory*. McGraw-Hill, 1964. 136

[81] C. Kittel. *Introduction to Solid State Physics*. Wiley, 1996. 137